# A search for high-mass resonances in final states with hadronically decaying tau leptons and high missing transverse momentum using pp-colision data at $\sqrt{s} = 13$ TeV collected by the ATLAS Detector

Dissertation

zur

Erlangung des Doktorgrades (Dr. rer. nat.)

dei

Mathematisch-Naturwissenschaftlichen Fakultät

der

Rheinischen Friedrich-Wilhelms-Universität Bonn

vorgelegt von

**Christos Vergis** 

aus

Marousi

Bonn 2024

Angefertigt mit Gene Friedrich-Wilhelms-U	chmigung der Mathematisch-Naturwissenschaftlichen Fakultät der Rheinischen Universität Bonn
Gutachter/Betreuer: Gutachter:	Prof. Dr. Jochen Dingfelder Prof. Dr. Florian Bernlochner
Tag der Promotion: Erscheinungsjahr:	27.05.2025 2025

# **Acknowledgements**

I would like to express my deepest gratitude to my supervisor, Prof. Dr. Jochen Dingfelder, for their invaluable guidance, support, and encouragement throughout the course of this thesis. Their expertise and mentorship have been instrumental in shaping this work.

I am also profoundly thankful to the University of Bonn for providing the academic environment, resources, and opportunities that made this research possible.

Furthermore, I am deeply grateful to my family and friends for their unwavering support, patience, and understanding. Their encouragement and assistance, particularly in reviewing and improving the quality of this thesis, have been a source of strength and motivation.

# **Abstract**

A search for new heavy charged gauge bosons W', predicted by some extensions of the Standard Model is presented in this thesis. This analysis is based on data collected from proton-proton collisions with a center-of-mass-energy of  $\sqrt{s}$ =13 TeV by the ATLAS detector. The integrated luminosity corresponds to 139 fb<sup>-1</sup>. The search is performed in the decay channel with one tau lepton that decays hadronically and a neutrino,  $W' \to \tau \nu$ . The scenarios considered are the *Sequential Standard Model*, where the W'-bosons have the same couplings as the Standard Model W-bosons, as well as *Non-Universal Gauge Interaction Models*, which allow for preferential couplings to the heavy generation of fermions.

No significant excess is observed in data and upper limits at 95% confidence level on the production cross sections of the W' bosons under the different signal hypotheses. Model-independent upper limits are also derived to allow re-interpretation of the results in more generic models.

# **Contents**

1	Intro	oduction	1
	1.1	The Standard Model of Particle Physics	1
	1.2	The tau lepton	3
2	The	Evnoriment	5
2		Experiment The Lorent Hadron Collider	5
	2.1	The Large Hadron Collider	_
	2.2	The ATLAS Experiment	8
		2.2.1 The ATLAS coordinate system	8
		2.2.2 Inner Detector	9
			11
		2.2.4 Muon Spectrometer	13
	2.3	Data Acquisition and Trigger	13
3	Ohia	ect Reconstruction	15
	3.1		15
	3.2		16
	3.3		17
	3.4		18
	3.5		18
	3.6		20
	3.7		20
	3.8		22
	3.9	Preselection summary	23
4	The	orv	25
	4.1		25
	4.2		25
			26
			27
			28
	4.3	• 66	30
	7.5		30
			31
	4.4		32
	4.4		
			32

#### Contents

Bi	bliog	yraphy 1	0
7	Con	nclusions	99
	6.3	Model independent limits	94
		6.2.3 Limits on Non-Universal Gauge Interaction Models	91
		6.2.2 Limits on Sequential Standard Model	90
	0.2	6.2.1 Fit procedure	85
	6.2	6.1.2 The Likelihood Ratio Test Statistics	82
		6.1.1 The Likelihood Model	81
	6.1	Hypothesis Testing	81
6	Stat		81
	5.7	Background validation	79
		5.6.3 Theoretical uncertainties	76
		5.6.2 Jet background uncertainties	73
		5.6.1 Experimental uncertainties	72
	5.6	Systematics	72
		5.5.3 Results	67
		5.5.2 Uncertainties on the truth-level correction weights	67
	3.3	5.5.1 Measurement of correction factors	63
	5.5	High- $p_{\rm T}$ tau reconstruction corrections	63
	5.4	5.3.2 High- $m_{\rm T}$ extrapolation and smoothening	56 60
		5.3.1 Fake Factor Method	55
	5.3	Background Modeling	54
	5.2	Event selection	45
	5.1	Analysis Strategy	43
5	Ana	alysis	43
		4.4.3 Signal	36

## Introduction

The main goal of particle physics is to understand the true nature of the fundamental blocks that build up the world we observe.

## 1.1 The Standard Model of Particle Physics

The Standard Model (SM) of particle physics has been established for several decades of theoretical predictions and experimental verifications. It currently stands as the most successful framework for describing the elementary particles and their fundamental interactions. Originating from the 1950s, its development now explains three of the four fundamental forces—the electromagnetic, weak, and strong interactions. Despite its success, certain questions remain unanswered, motivating physicists to explore theories beyond the SM.

The roots of the SM trace back to the advancement of the quantum mechanics in the 1920s and the subsequent discovery of subatomic particles, such as the positron. The 1930s saw the discovery of the neutron and theoretical developments in quantum electrodynamics (QED), the first quantum field theory describing the electromagnetic force. QED was successfully formalized in the 1940s, offering a model for the interaction between charged particles via the quanta of electromagnetic interactions; the photons.

However, it was not until the unification of the weak and electromagnetic forces, as initially proposed by Sheldon Glashow, Abdus Salam, and Steven Weinberg in the 1970s, when the SM solidified its foundation. Their electroweak theory introduced the new particles, *W*-boson and *Z*-boson, as mediators of the weak force, together with the photon as the carrier of the electromagnetic force, and relied on the Higgs mechanism to explain how particles acquire mass.

In the meantime, another crucial aspect of the SM was developed; the quantum chromodynamics (QCD). QCD was proposed in the 1970s to describe how the quarks interact via the gluons to bind to form hadrons, such as protons and neutrons. This theory introduced the concept of color charge and confinement, the principle that does not allow for free quarks to be realized in nature at low energies. Together with the electroweak theory, the QCD provided a comprehensive theoretical framework for the quantum fundamental forces. Together they were formalized into the SM as a gauge theory with symmetry group  $SU(3) \otimes SU(2) \otimes U(1)$ .

At the same time that the SM was developed, several discoveries assisted in its establishment as the most accurate model for theoretical predictions. Some of those are the observation of weak neutral

currents, the discovery of the Z/W-bosons and the top-quark. The final discovery of a fundamental particle occurred at the Large Hadron Collider at CERN in 2012, when both the ATLAS and CMS Experiments declared the discovery of the Higgs Boson. At the same time, during the past decades, the SM has been challenged by many experiments worldwide that aim to test the accuracy of its predictions. Up to date, no experiment has observed any significant deviation from the SM expectations, validating the SM predictions to unprecedented levels.

Despite its success, the SM is incomplete and has notable limitations. The most profound limitation of the SM is that it is not compatible with the theory of gravitational interactions. Some notable difficulties faced by SM in describing what observe in the universe is the existence of neutrino masses, the presence of Dark matter and energy, as well as the matter-antimatter asymmetry in the universe. These unresolved questions within the SM have inspired various theories beyond the SM, such as supersymmetry, extra dimensions, and grand unification, each proposing new particles, symmetries, or interactions. As these theories are being proposed, the natural curiosity for scientific progress motivates their experimental testing. The Large Hadron Collider and other facilities continue to probe these possibilities, looking for deviations from SM predictions, rare decays, and new particle signatures.

Table 1.1: Particles of the Standard Model, organized by generation, type, charge, and mass (Ref. [1])

Generation	I	Ш	Ш	
	Quarks			
Up-type	<i>u</i> (up)	c (charm)	t (top)	
Charge [e]	$+\frac{2}{3}$	$+\frac{2}{3}$	$+\frac{2}{3}$	
Mass [MeV/ $c^2$ ]	2.2	1273	172570	
Down-type	d (down)	s (strange)	b (bottom)	
Charge [e]	$-\frac{1}{3}$	$-\frac{1}{3}$	$-\frac{1}{3}$	
Mass [MeV/ $c^2$ ]	4.7	93.5	4183	
	Leptons			
Charged Lepton	e (electron)	μ (muon)	τ (tau)	
Charge [e]	-1	-1	-1	
Mass [MeV/ $c^2$ ]	0.511	105.7	1776.9	
Neutrino	$v_e$ (electron neutrino)	$v_{\mu}$ (muon neutrino)	$v_{\tau}$ (tau neutrino)	
Charge [e]	0	0	0	
Mass [MeV/c <sup>2</sup> ]	$< 0.8 \times 10^{-6}$	< 0.19	< 18.2	

sociated with any	menachon	in the sivi.	
Boson	Symbol	Mass (GeV/c <sup>2</sup> )	<b>Associated Interaction</b>
Photon	γ	0	Electromagnetic
W-boson	$W^{\pm}$	80.369	Weak
Z-boson	$Z^0$	91.188	Weak
Gluon	g	0	Strong
Higgs Roson	Н	125.2	_

Table 1.2: The Standard Model bosons, their symbols, mass and associated interactions (Ref. [1]). The Higgs boson is not associated with any interaction in the SM.

## 1.2 The tau lepton

The tau lepton  $(\tau)$  belongs to the third generation of fermions. With a mass of  $(1\,776.93\pm0.09)\,\text{MeV}$  and a mean lifetime of  $(290.3\pm0.5)\,\text{fs}$  [1], it is the most massive and short-lived charged lepton in the SM. Its high mass kinematically allows the tau lepton to decay into either light leptons or hadrons, making it unique among the lepton family. The short mean lifetime of the tau lepton corresponds to a mean decay length of  $87.03\,\mu\text{m}$ . Consequently, most of the tau leptons produced at the LHC will decay before they reach the detectors.

The tau lepton decays via the weak interaction. In leptonic decays, the tau produces a lighter lepton (either an electron or muon) along with two neutrinos. These decays account for approximately 35% of its total decay rate. The remaining 65% of tau decays result in hadronic final states, with various combinations of charged  $(h^{\pm})$  and neutral  $(h^{0})$  hadrons. The branching ratios for the most important tau decays are shown in Tab. 1.3.

Table 1.3: Branching Ratios of tau lepton decays into charged and neutral mesons and leptons (Ref. [1]).

Decay Mode	Branching Ratio (%)
$\tau^{\pm} \rightarrow e^{\pm} \nu_e \nu_{\tau}$	17.82
$\tau^{\pm} \to \mu^{\pm} \nu_{\mu} \nu_{\tau}$	17.39
Total	35.21
$\tau^{\pm} \to h^{\pm} \nu_{\tau}$	11.51
$\tau^\pm \to h^\pm h^0 \nu_\tau$	25.93
$\tau^{\pm} \to h^{\pm} h^0 h^0 v_{\tau}$	9.48
$\tau^{\pm} \to h^{\pm} (\geq 3h^0) \nu_{\tau}$	1.34
Total	48.26
$\tau^{\pm} \to h^{\pm} h^{\pm} h^{\mp} \nu_{\tau}$	9.80
$\tau^{\pm} \to h^{\pm} h^{\pm} h^{\mp} (\geq 1 \ h^0) \nu_{\tau}$	5.29
Total	15.20

# The Experiment

This chapter briefly describes the experimental setup that the work presented in this thesis used. In Section 2.1, the Large Hadron Collider (LHC) accelerator, which provides the proton-proton collisions that produced the data used in this thesis is briefly described. Finally, in Section 2.2 the ATLAS detector, where the data was recorded, is presented with a brief description of the coordinate system and detector parts.

## 2.1 The Large Hadron Collider

The LHC is currently the world's largest particle accelerator. The purpose of the LHC is to accelerate counter-rotating proton or ion beams to high energies before collision. It is a 27 km ring of superconducting magnets with a number of accelerating structures that boost the energy of the particles along the way and keeps them confined in the beam pipes. This thesis focuses solely on collisions of proton beams that occurred between the years 2015 and 2018 (Run2) at a center-of-mass energy of 13 TeV. A schematic figure of the accelerator complex is shown in Fig. 1. The protons are initially taken from bottles of hydrogen gas. After the hydrogen atoms are ionized by an external electric field, the free protons are guided through a sequence of radio-frequency cavity accelerators: LINAC2, Proton Synchrotron Booster (PSB), Proton Synchrotron (PS) and Super Proton Synchrotron (SPS) before they reach the energy of 450 GeV and get separated into discrete packets ("bunches"). At that point, the protons are injected into the beam pipes of the LHC ring. The protons are further accelerated in opposite directions in separate beam pipes. The energy of the proton beams inside the LHC increases to 6.5 TeV. There are four interaction points (IP) where the proton beams are made to cross each other and collisions can occur. Around those IP, the four main experiments (ATLAS, CMS, ALICE and LHCb) are built. This thesis uses data recorded by the ATLAS detector which is discussed in more detail in Section 2.2.

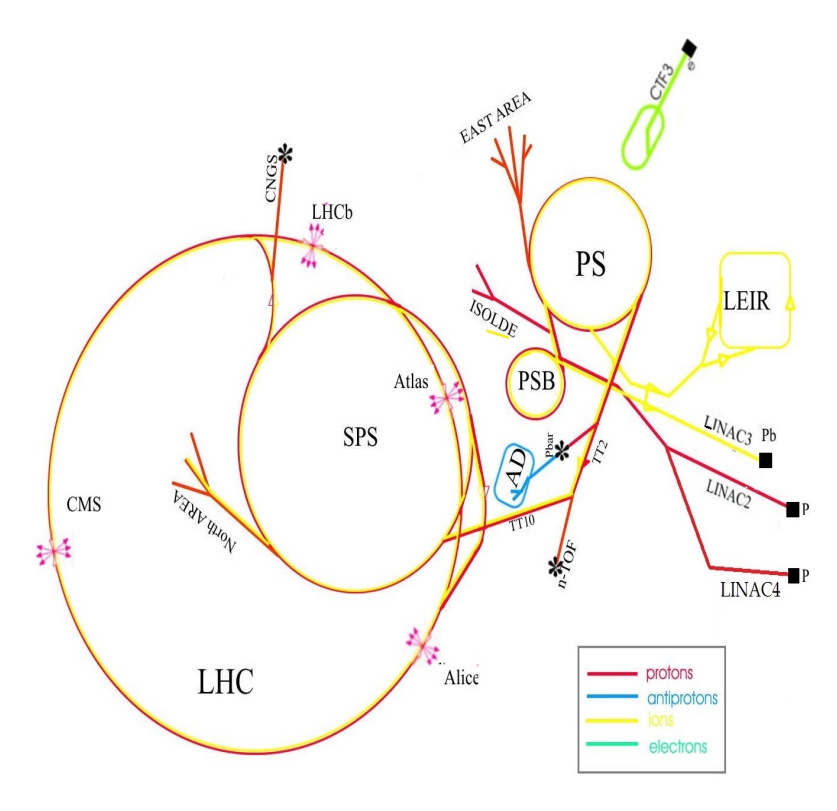


Figure 1: A schematic of the LHC aparatus (Taken from [2] and modified by the author).

One important property of an accelerator is the luminosity. The luminosity quantifies the number of interactions that occur over a period of time. Thus, over a period of time, a process X with cross section  $\sigma_{ppX}$  will occur in  $N_X$  events that are given by:

$$N_X = \sigma_{ppX} L \tag{2.1}$$

where L the integrated luminosity. From Eq. (2.1), the integrated luminosity has dimensions of m<sup>-2</sup> and typically is quoted in units of inverse barns (1b<sup>-1</sup> = 10<sup>24</sup>cm<sup>-2</sup>). The integrated luminosity is accumulated over time and so an interesting quantity is its rate,  $\mathcal{L}$ , also called *instantaneous luminosity*. The instantaneous luminosity has units of cm<sup>-2</sup>s<sup>-1</sup> and it can be calculated from the properties of an accelerator and the beams by [3]:

$$\mathcal{L} = \frac{N_p^2 n_b f_{\text{rev}} \gamma_r}{4\pi \epsilon_n \beta^*} \mathcal{F},\tag{2.2}$$

where  $N_p$  is the number of protons per bunch,  $n_b$  the number of bunches,  $f_{\rm rev}$  the revolution frequency,  $\gamma_r$  the relativistic gamma factor,  $\epsilon_n$  the normalized transverse beam emittance,  $\beta^*$  the beta function of the beam and  $\mathcal F$  the geometric luminosity reduction factor. The later accounts for the beams crossing at a certain angle at the IP. Some of the properties of the accelerator that enter Eq. (2.2) are given in Tab. 2.1. In order to achieve a large statistical precision and observe events originating from rare processes, a high luminosity was one of the main design criteria for the LHC. The delivered luminosity from LHC during the Run2 operation was about  $160\,{\rm fb}^{-1}$ . From this amount of data, the good quality

data collected by the ATLAS detector and used by this analysis during the years 2015-2018 was  $139.0 \pm 2.4 \text{ fb}^{-1}$  [4].

Operation Year	2015	2016	2017	2018
Bunch spacing (ns)	50 – 25	25	25	25
$N_p$ (10 <sup>11</sup> protons/bunch)	1.15	1.2	1.2 - 1.25	1.1
$n_b$	2244	2040 - 2556	1916 – 1868	2556
$f_{\rm rev}$ (kHz)	11.246	11.246	11.246	11.246
$\epsilon_n  (\text{mm} \times  \text{rad})$	3.5	3.5 - 2.1	2.3 - 1.8	2
$\beta^*$ (m)	0.8	0.4	0.4 - 0.3	0.3 - 0.25
Half crossing angle ( $\mu$ rad)	145	185 - 140	150 - 120	160 - 130
Delivered integrated luminosity (fb <sup>-1</sup> )	4.2	39.7	50.6	66
Good recorded integrated luminosity (fb <sup>-1</sup> )	3.2	33.0	44.3	58.5

Table 2.1: Beam operation parameter values from the LHC for the separate years. The values are taken from Reference [5]. The Good recorded integrated luminosity refers to the good physics data collected by the ATLAS and used in this thesis.

## 2.2 The ATLAS Experiment

ATLAS is one of the main experiments at the LHC. It aims to study a wide variety of physics from SM to BSM and therefore it is a general purpose cylindrical detector built around one of the four IPs at the LHC. The detector is approximately 44 m wide and 25 m in height. Going from the inside out, it consists of several layers which aim to record the different types of outgoing particles. The innermost layer is the inner detector, which records the trajectories of charged particles. Following the inner detector is the Calorimeter system, which measures the energies of electrons, photons and hadrons. Finally, the outer-most layers of the ATLAS detector consist of the Muon Spectrometer with the purpose of identifying and measuring the tracks of muons. Each layer is described in more detail in the subsequent sections. A cut-away view of the ATLAS detector is given in Fig. 2.

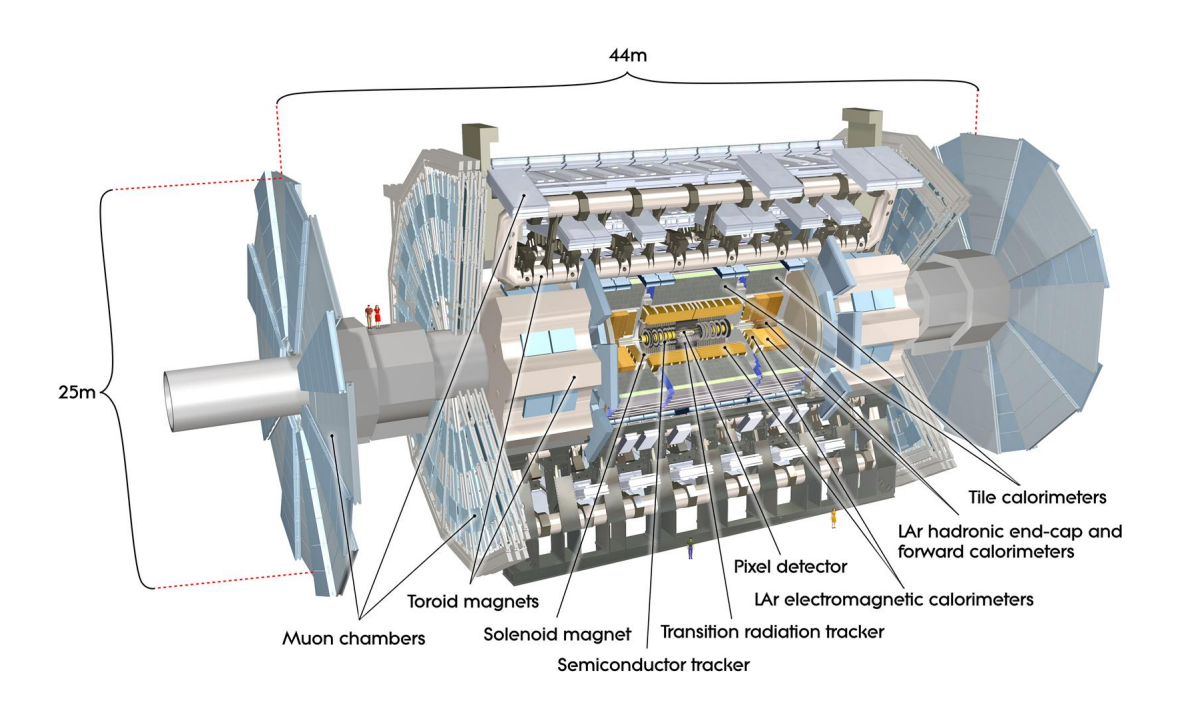


Figure 2: A cut-away view of the ATLAS detector (Taken from [6]).

#### 2.2.1 The ATLAS coordinate system

The ATLAS coordinate system uses the IP as the origin, while the axis along the beam direction defines the *z*-axis. The *x*-*y* plane is transverse to the beam direction. The positive *x*-axis is defined as pointing from the interaction point to the center of the accelerator's ring and the positive *y*-axis is defined as pointing upwards. Due to the cylindrical symmetry of the detector around the transverse plane, cylindrical coordinates are typically used. The *x*, *y* coordinates are replaced by *r*,  $\phi$ , where *r* is the radial distance from the IP and  $\phi \in [-\pi, \pi]$  is the azimuthal angle relative to the *x*-axis direction around the beam pipe. The polar angle  $\theta$ , which is the angle to the beam axis, is also replaced by the pseudorapidity. The pseudorapidity,  $\eta$ , is defined as:

$$\eta = -\ln \tan \frac{\theta}{2} \tag{2.3}$$

and thus  $\eta$  tends to zero when  $\theta$  reaches  $\pi/2$  (perpendicular to the beam axis). The ATLAS coordinate system is also depicted in Fig. 3, where all the coordinate representations are sketched.

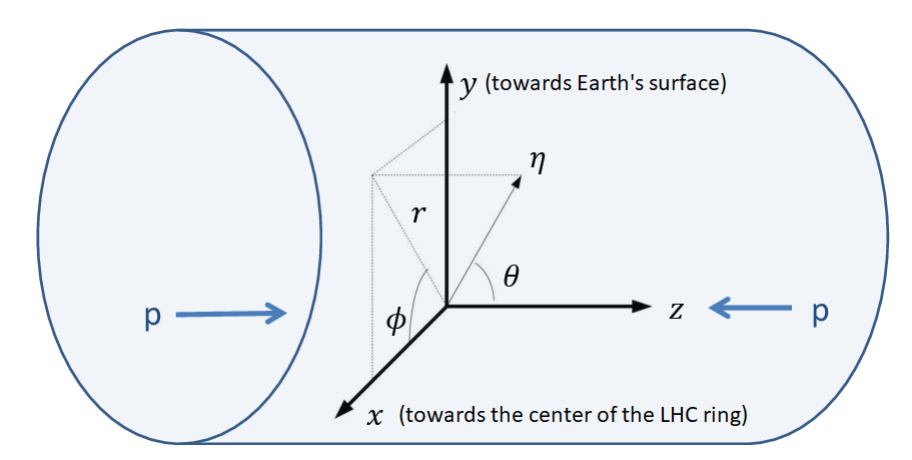


Figure 3: The ATLAS coordinate system. The blue shaded cylinder represents the ATLAS detector. The blue arrows indicate the incoming protons. The figure was taken from [7] and modified by the author.

An additional quantity which can be defined is the angular separation,  $\Delta R(p_1, p_2)$ , between two points away from the beam axis  $p_1 = (\phi_1, \eta_1)$  and  $p_2 = (\phi_2, \eta_2)$ :

$$\Delta R(p_1, p_2) = \sqrt{\Delta \eta_{12}^2 + \Delta \phi_{12}^2} , \qquad (2.4)$$

where  $\Delta \eta_{12} = \eta_1 - \eta_2$  and  $\Delta \phi_{12} = \phi_1 - \phi_2$ .

#### 2.2.2 Inner Detector

The inner detector is the closest module to the IP. It covers the range of  $\eta \in [-2.5, 2.5]$  and its purpose is to reconstruct the trajectory of charged particles. The trajectory of the charged particles gives information about the particles' momenta, charge sign and allows to identify the primary vertices (PV), i.e. the coordinates where the hard scattering occurred, or secondary vertices. Secondary vertices are associated to vertex coordinates that are displaced from the primary vertex, and can originate from decays of secondary particles with a significant flight length. In order to measure the charged particle momenta, the inner detector is immersed in a magnetic field of 2 T parallel to the beam-axis produced by a solenoid magnet.

The inner detector which is shown in Fig. 4, consists of three sub-systems. These components are the Pixel Detector, the Semiconductor Tracker (SCT) and the Transition Radiation Tracker (TRT). The Pixel Detector uses silicon pixels while the SCT uses silicon strips. Both provide a high precision spatial measurement for the particle tracking close to the PV. When the charged particles cross the silicon sensors, they generate electron-hole pairs. The electron-hole pairs are then collected as electric signals by the application of an external electric field. The TRT uses gas filled straw drift tubes. It provides worse spatial resolution measurements but a larger number of measured points along the particle's trajectory. The charged particles traversing the drift tubes ionize the gas. The electrons from

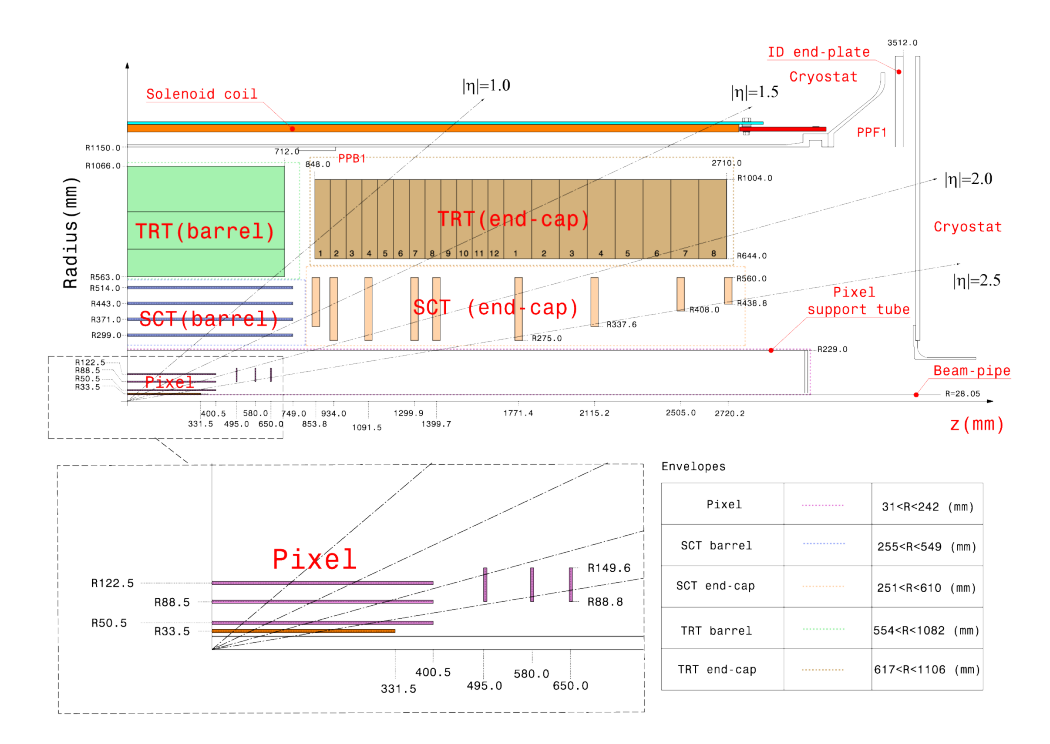


Figure 4: The r-z cross section of the ATLAS inner detector. Both the radius r (R in figure) and the distance z are shown in mm. The diagonal lines represent the different values of  $\eta$  where a transition in any of the detectors occur. The Pixel Detector is further zoomed. Figure was taken from [8].

the ionization then drift to the wire at the center of the straw by an external electric field, where they are recorded.

Since the Long-Shutdown 1 upgrades of 2013-2015, the Pixel Detector consists of four layers. It contains over 80 million pixels in total and provides an average of four to five measurements per charged particle [9]. The closest layer (IBL) has a radial distance of approximately 33 mm from the IP. The whole detector spans the radial region up to 150 mm. The spatial resolution of the pixel detector without the IBL is  $10 \, \mu m$  on the  $\eta$ - $\phi$  plane and  $115 \, \mu m$  along the z direction. The IBL improved the measurement uncertainties as it is capable of recording measurements with a spatial resolution of  $8 \, \mu m$  in  $r - \phi$  and  $40 \, \mu m$  in z.

The SCT surrounds the Pixel Detector, spanning the radial regions from 299 mm to 560 mm. Each module of SCT is composed of a double layer of silicon strips whose axes are tilted with respect to another. The pair measurements at each SCT layer locates charged particles in the  $\eta$ - $\phi$  plane with an accuracy of 17  $\mu$ m and along the z-direction with an accuracy of 580  $\mu$ m. The SCT typically provides four to twelve measurements per particle.

Finally the TRT is the largest sub-detector of the inner detector, spanning the radial distances from 563 mm to 1066 mm. It covers  $|\eta| < 2.0$  and is composed of approximately of 300 thousand straw drift tubes. It can measure the position of charged particles with an accuracy of 130  $\mu$ m per single detection in the  $\eta$ - $\phi$  plane but provides on average 30 hits per particle. The TRT is also useful in particle identification through the detection of transition radiation. The charged particles that cross between tubes can emit transition radiation (photons) with a probability that depends on the particle's

Lorentz factor  $\gamma$ . Thus, for fixed momentum values, the electrons can radiate more photons than the charged hadrons, providing discrimination between the two.

The resolution  $\sigma_t$  of the measurements of the different track properties t can be expressed by:

$$\sigma_t = \sigma_t(\infty) \left( 1 \oplus \frac{p_t}{p_T} \right) , \qquad (2.5)$$

where the symbol  $\oplus$  denotes the quadrature addition (i.e.  $a \oplus b = \sqrt{a^2 + b^2}$ ),  $\sigma_t(\infty)$  is the asymptotic resolution expected at infinite momentum and  $p_t$  is a constant representing the value of  $p_T$  for which the intrinsic and multiple-scattering terms are equal for the parameter t. The momentum resolution is  $\sigma_{p_T}/p_T \approx 1\%$  at 20 GeV and reaches better than 50% at 1 TeV [10].

#### 2.2.3 Calorimeter

The calorimeter system of the ATLAS detector, pictured in Fig. 5, is used to measure the energy of electrons, photons and hadrons. It is divided into two subsystems, namely the Electromagnetic Calorimeter (ECAL) and the Hadronic Calorimeter (HCAL). Together they cover the region  $|\eta| < 4.5$  and provide full coverage around  $\phi$ . The ATLAS calorimeters are sampling calorimeters. Therefore, the particles that traverse the detector material produce showers of energy and only a fraction of the produced energy is measured by the active detector sensors. The energy of the full shower is inferred from the observed energy.

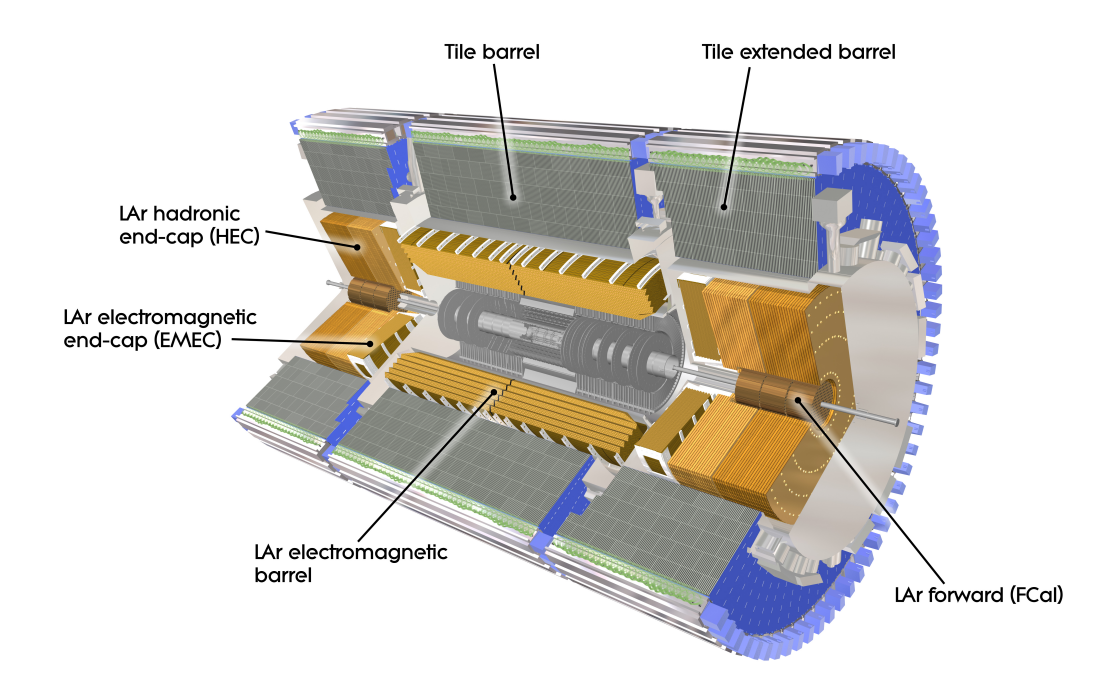


Figure 5: A schematic view of the ATLAS Calorimeter detector and its parts. The image taken from [11]

• The ECAL is dedicated to measure the energy of the photon and electron showers. It is divided into two regions: the barrel ( $|\eta| < 1.475$ ) and the end-cap (1.375 <  $|\eta| < 3.2$ ) calorimeter. It

is a lead-Liquid Argon (LAr) detector and so allows high granularity measurements that are crucial for particle identification in the range  $|\eta| < 2.5$ . The ECAL is radially segmented into three sections with different granularity. The first segment is called ECAL1 and it can separate the showers initiated by electrons or photons and showers initiated by neutral pions (the neutral pions decay predominantly into two photons). It achieves this goal by a fine segmentation in  $\Delta\phi \times \Delta\eta$  of approximately  $0.098 \times 0.0031$ . The second section, ECAL2, is mainly used for measuring the energy with a granularity of n  $\Delta\phi \times \Delta\eta \approx 0.0245 \times 0.025$ . Finally, the outermost layer, ECAL3, has wider cells ( $\Delta\phi \times \Delta\eta \approx 0.0245 \times 0.05$ ) and adds depth to the ECAL. The final depth of the ECAL reaches 22-30  $X_0$  (absorption lengths). A presampler (PS) detector is positioned before the ECAL layers. It covers the region  $|\eta| < 1.8$  and has a granularity of  $\Delta\phi \times \Delta\eta \approx 0.1 \times 0.025$ . It is mainly used to correct the energy lost by electrons or photons upstream of the calorimeter.

The ECAL design energy resolution after noise subtraction is:

$$\frac{\sigma(E)}{E} = \frac{10\%}{\sqrt{E(\text{GeV})}} \oplus 0.7\% , \qquad (2.6)$$

where the first term is the "stochastic" term and accounts for fluctations in the shower development, while the second term is the "constant" term that appears because of local non-uniformities in the calorimeter's response.

The HCAL subsystem surrounds the ECAL. Because the hadrons on average have a longer interaction length, the HCAL had to be built with a wider granularity to cover a larger area and volume (from r ≈2.28 m to r ≈4.25 m). In principle, its purpose is to measure the energy of hadrons. It consists of the Tile Calorimeter, the LAr hadronic endcap calorimeter and the LAr forward calorimeter, each covering different pseudorapidity regions up to |η| ≈ 5.

The Tile Calorimeter is placed directly outside the ECAL envelope. It consists of a barrel (LBA, LBC) that covers pseudorapidities up to  $|\eta| = 1.0$  and two extended barrels (EBA, EBC) in the range of  $0.8 < |\eta| < 1.7$ . It uses steel as the absorber material and scintillating tiles as the active material. The barrel's layer segmentation in thickness is approximately 1.5, 4.1 and 1.8 interaction lengths X and the extended barrel's are of 1.5, 2.6 and 3.3 X thick.

The LAr Hadronic endcap calorimeter consists of two independent wheels per endcap, located behind the ECAL endcap and sharing the same LAr cryostats. It covers the range  $1.5 < |\eta| < 3.2$  partially overlapping with the tile and forward calorimeters at its edges. Each wheel is segmeted in depth in two layers, for a total of four layers per endcap. The LAr forward calorimeter is closer to the beam pipe and covers the "forward" regions of  $3.1 < |\eta| < 4.9$ . It is designed for high-density particle fluxes and is approximately 10X deep.

The HCAL design energy resolution is:

$$\frac{\sigma(E)}{E} = \frac{50\%}{\sqrt{E(\text{GeV})}} \oplus 3\% \tag{2.7}$$

#### 2.2.4 Muon Spectrometer

The Muon Spectrometer (MS) is the outer part of the ATLAS detector. It is designed to detect charged particles that leave the barrel or endcap calorimeters and measure their momenta. Its covers the pseudorapidity range of  $|\eta| < 2.7$ . A cross-sectional view of the MS is shown in Fig. 6.

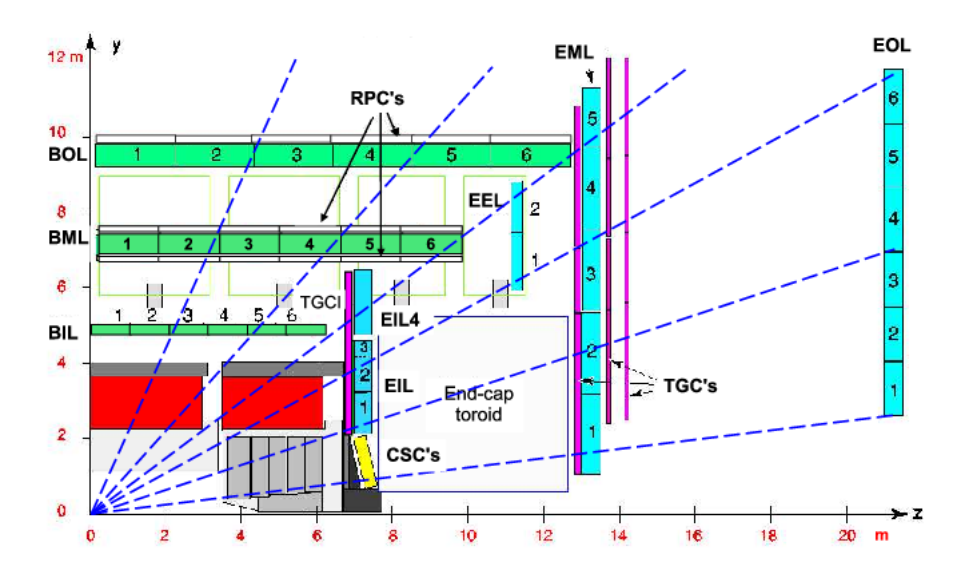


Figure 6: The profile of the Muon Spectrometer of the ATLAS Detector in the r-z plane for  $|\eta| > 0$ . The MDT are shown in green (barrel) and blue (endcaps) while the CSC are colored yellow. The RPC (TGC) are shown as black outlined (purple) blocks. The straight dashed lines show the trajectories of infinite momentum muons. Image was taken from [6].

The MS operates in a toroidal magnetic field. In the barrel region the muon chambers are arranged in three cylindrical layers around the beam axis while the transition and endcap region chambers are arranged in three planes perpendicular to the beam. The particles' positions are measured by Monitored Drift Tubes (MDT) for most of the pseudorapidities except for the  $2 < |\eta| < 2.7$  range where Cathode Strip Chambers (CSC) are used. Additional chambers such as the Resistive Plate Chambers (RPC) and Thin Gap Chambers (TGC) are added which provide a fast tracking information of the muons, used by the muon trigger.

## 2.3 Data Acquisition and Trigger

Triggering the events, i.e. filtering the events, is an important part of the data acquisition and the functionality of the LHC experiments. To study rare processes, one needs to produce a large number of collisions. That means to collide beams at high frequency. At the ATLAS detector, beam crossings occur with a frequency of approximately 40 MHz. Saving all these events in tape disks would require about  $O(100\,\mathrm{TB/s})$  of space. Managing this size of data is not feasible and for that reason the detectors use several algorithms to rapidly select interesting events. The ATLAS trigger system aims to reduce the size of recorded data to a few thousand events per second. It consists of two steps:

- Level-1 trigger (L1), is the first step of the trigger, that is implemented on hardware and during Run2 is based on field-programmable gate array (FPGA) technology. Its goal is to reduce the original recording rate of data to  $100 \, \text{kHz}$  in just a few  $\mu \text{s}$  to be further processed in the next step.
- **High Level Trigger** (HLT), is implemented at software level and aims to decrease the number of collected data to the original goal of 1 kHz in a few 100ms.

However, while the frequency of interactions at LHC increases, so does the rate of collecting data. Hardware updates of the trigger are not possible during operations of the machine, therefore, in order to keep the trigger rate constant through its runs, ATLAS had to either implement more efficient algorithms at HLT or adjust the trigger thresholds depending on the instantaneous luminosity. For the triggers used in this search, both these methods were utilized and their result on the trigger rate are shown in Fig. 7 . Further information about the triggers that were used is given in more detail in Sec. 3.7.

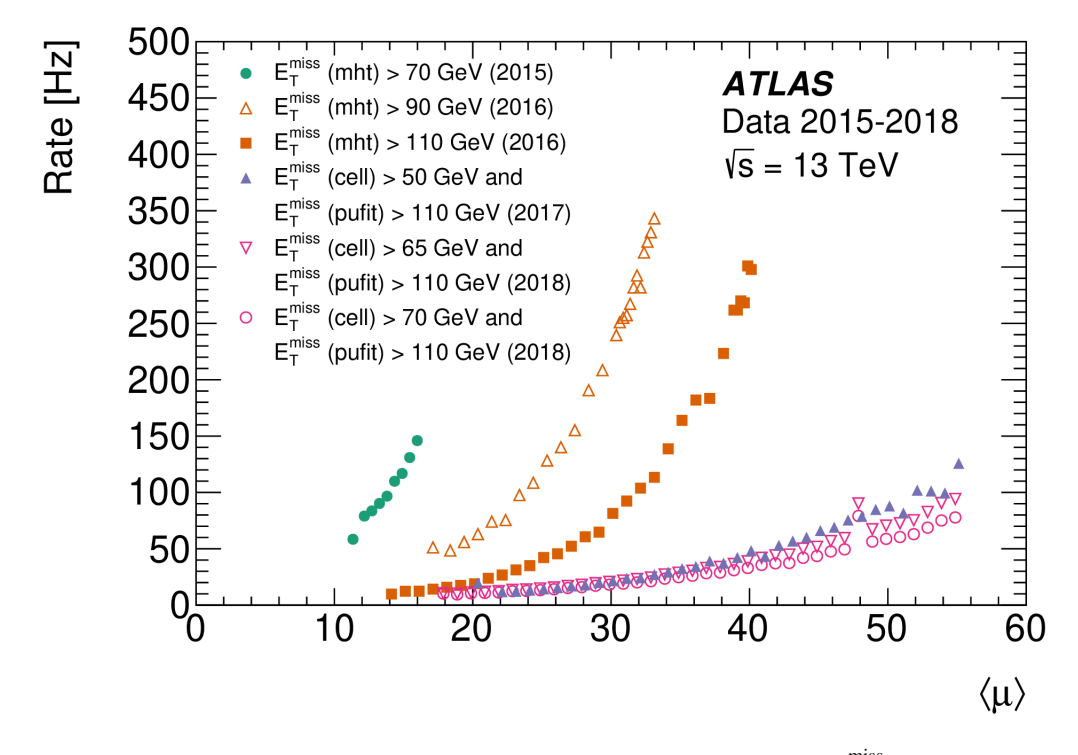


Figure 7: Comparison between typical output trigger rates for the different baseline  $E_{\rm T}^{\rm miss}$  triggers for the different values of the average interactions per proton bunch crossing  $\langle \mu \rangle$ , taken from [12]. The later is proportional to the instantaneous luminosity. Thus, with the increase of instantaneous luminosity of the Run2 data collection the trigger rates decreased by either changing the  $E_{\rm T}^{\rm miss}$  threshold requirements of the triggers or by changing the algorithm ("mht" versus "pufit") used in  $E_{\rm T}^{\rm miss}$  calculation.

# **Object Reconstruction**

Different particles can be produced during the protons collision inside the beam pipe. Some of these particles live long enough to reach the detector and interact with its material. During the interaction the particles deposit part of their energy or momenta in the detector. These deposits are recorded as electronic signals. Solely the collection of electronic signals does not provide information neither about the particle type (i.e. whether it is an electron, muon, etc.) nor the particle's four-momentum. Thus, in order to associate physical particles to the collection of electronic signals, the later are given as inputs to the ATLAS reconstruction algorithms. These algorithms convert the signals into collections of measurements and properties associated with the particles that were produced in the collision. This chapter briefly describes the reconstruction algorithms of objects that are relevant for this analysis and the object selections. Section 3.1 mentions the reconstruction of tracks. Sections 3.2 and 3.3 describe the reconstruction and selection of muons and electrons respectively. The reconstruction and preselection of jets is summarized in Section 3.4. Finally, in Section 3.5 the tau reconstruction and identification steps are summarized and in Section 3.6 the missing transverse momentum of the event is defined and described. A summary on the object pseselection is given in Section 3.9.

#### 3.1 Track Reconstruction

The trajectories of charged particles (tracks) are reconstructed from measurements of the particle interactions ("hits") in the Inner Detector and the MS. The track parameters, such as the direction, the origin and the momentum are determined by a three-dimensional fit to the position of the track hits. During the track fitting, tracks that do not meet some good quality criteria are rejected. The quality criteria used are [13]:

- resulted in a poor fit (quantified by the track's  $\chi^2$ )
- $p_{\rm T} > 400 \,{\rm MeV}$
- $|\eta| < 2.5$
- Number of hits requirements:
  - o Pixel + SCT  $\geq 7$
  - o No more than one shared Pixel hits on the same layer

- o No more than two shared SCT hits on the same layer
- o No more than two holes (miss hits in the active detector material) in the combined Pixel and SCT.
- o No more than one hole in the Pixel detector.
- $|d_0^{\rm BL}| < 2 \, {\rm mm}$
- $|z_0^{\rm BL} \sin \theta| < 3 \,\mathrm{mm}$

where  $d_0^{\rm BL}$  stands for the transverse impact parameter with respect to the beam-axis,  $z_0^{\rm BL}$  is the longitudinal difference along the beam-axis between the point where  $d_0^{\rm BL}$  is measured and the primary vertex and  $\theta$  being the polar angle of the track.

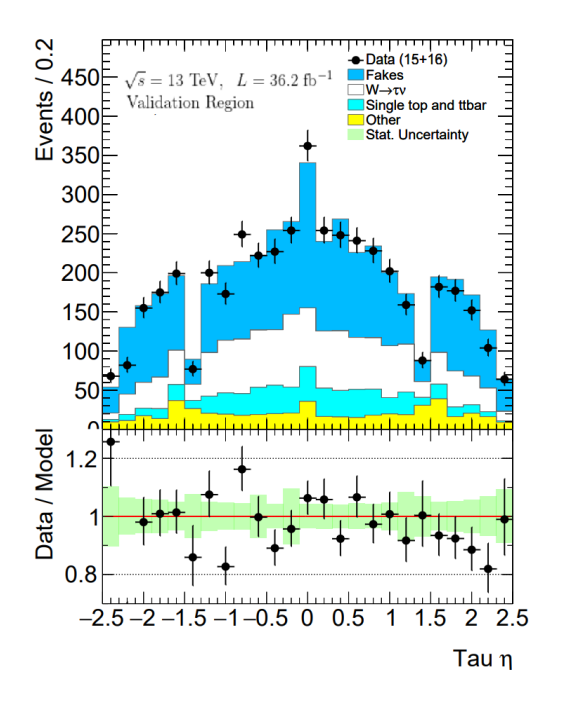
Through the track reconstruction, the track's four-momentum are measured and several parameters of the tracks are obtained. These track parameters can be the sign of the particle's charge or other parameters, such as the significance of transverse impact parameter's  $d_0^{\rm BL}$ , defined as the ratio of the transverse impact parameter of the track and the estimated error  $(d_0^{\rm sig} = \frac{|d_0^{\rm BL}|}{\sqrt{\sigma_{d_0^{\rm BL}}}})$  or the distance  $z_0 \sin \theta$ .

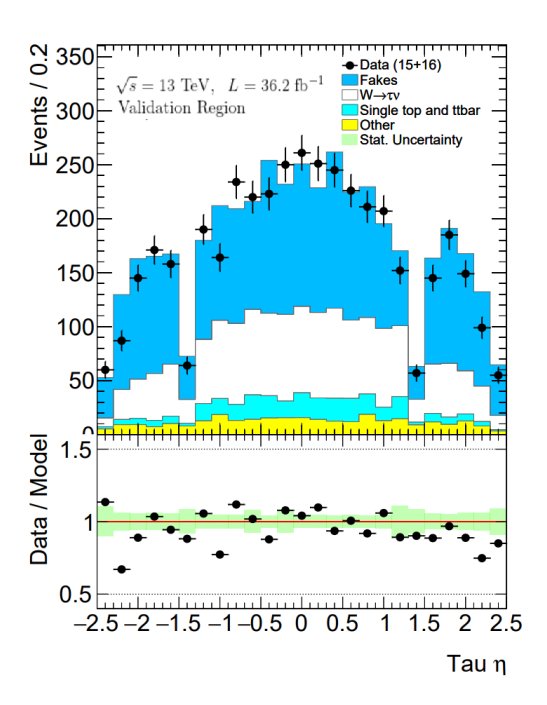
#### 3.2 Muon Reconstruction

Muon candidates are reconstructed from tracks using four algorithms for the reconstruction. The two of them rely on matching tracks of the Inner Detector to the complete tracks in the MS (*Combined*) or track-segments in the MS (*Segment-tagged* muons). The third performs a matching between the fitted Inner detector track and an energy deposit in the calorimeter (*Calorimeter-tagged* muons). The last algorithm reconstructs *Extrapolated* muons that consist of a track only at the MS.

ATLAS provides four identification working points for muons. This analysis makes use of *Loose* muons, that have reconstruction efficiency of 98.1% [14]. Moreover, the muon candidates are required to have  $p_T > 20 \, \text{GeV}$  and be within the  $|\eta| < 2.5 \, \text{region}$ . In addition, to ensure that the muons originate from the hard scatter, additional requirements on the muons'  $d_0^{\text{sig}} < 3$  and  $z_0 \sin \theta < 0.5 \, \text{mm}$  are imposed. In order to avoid selecting muons that originate from secondary meson decays, this analysis uses the  $TightTrackOnly\_FixedRad$  isolation criteria for the muon selection. The isolation, as the name suggests, requires that the muon tracks appear isolated in the detector. For that reason, it minimizes the energy detected surrounding the muon track. The  $TightTrackOnly\_FixedRad$  requires that the scalar sum of  $p_T$  of all the tracks with  $p_T > 1 \, \text{GeV}$  within a cone size around the muon of  $R_{\text{ptcone30}} = \min(\frac{10 \, \text{GeV}}{p_T}, 0.3)$  does not exceed the 6% of the total muon's transverse momentum. The "FixedRad" suffix indicates that for muons with transverse momenta above 50 GeV, the cone size is fixed to 0.2.

The requirements on muons' track parameters and isolation are removed for the overlap removal process (Section 3.8) in order to decrease the number of jets that fake the tau in the  $|\eta| < 0.1$  region (Fig. 8).





- (a) Only muons that passed the track properties and isolation requirements were considered in the overlap removal step.
- (b) Muons that failed the track properties and isolation requirements were also considered in the overlap removal step.

Figure 8: The hadronically decaying tau  $\eta$  distribution.

#### 3.3 Electron Reconstruction

Electrons traversing the detector material leave tracks in the Inner Detector and generate electromagnetic showers in the ECAL. The electron reconstruction algorithm utilizes this information and matches clusters of energy in the ECAL to tracks of the Inner Detector. A "sliding-window" algorithm is used, which searches for deposited energy local maxima in small windows of  $\eta$ - $\phi$  of the ECAL. Then tracks are matched to the found maxima and the seed clusters are resized to account for capture the energy distributions in the different calorimeter regions. The energy of the electron is set equal to the cluster energy after correcting for energy loss in material before entering the calorimeter or lateral and longitudinal energy leakage from the cluster.

The analysis presented in this thesis selects electrons that have  $p_{\rm T}$  of at least 20 GeV and are found within the  $|\eta| < 2.47$  region of the detector but excluding the barrel-endcap transition region  $|\eta| \in (1.37, 1.52)$ . The identification of electrons in ATLAS uses a Log-Likelihood (LLH) based selection in order to discriminate prompt electrons from other background. This analysis uses the "Loose" LLH working point provided by ATLAS, which corresponds to an electron identification efficiency of 85% (96%) for  $E_{\rm T}$  =20 GeV (100 GeV). Similarly to muons, track-based requirements on  $d_0^{\rm sig} < 3$  and  $z_0 \sin \theta < 0.5$  mm are imposed on the selected electron candidates. For selecting isolated electrons, the "Fix (Loose)" [15] isolation working point is used.

#### 3.4 Jet Reconstruction

The collimated collections of particles that originate from the fragmentation and hadronization of quarks and gluons are referred to as "jets". The reconstruction of jets is essential for the rest particle reconstruction, such as the hadronically decaying tau leptons.

Jets are reconstructed from the energy deposits in the calorimeters using the anti- $k_t$  algorithm [16] with a radius parameter R=0.4. The algorithm takes as inputs three-dimensional energy clusters called *topological clusters* (TopoClusters) [17]. The TopoClusters are calibrated using a Local hadronic Calibration (LC), which corrects for energy leakage outside the reconstructed clusters and the non-compensation of the ATLAS calorimeters.

The anti- $k_t$  algorithm defines the distance between two objects i, j as  $d_{ij}$  and the distance of the i-th cluster to the beam  $d_{iB}$ :

$$d_{ij} = \min\left(p_{T,i}^{-2}, p_{T,j}^{-2}\right) \frac{(\Delta R_{ij})^2}{R^2}$$
(3.1)

$$d_{iB} = p_{T,i}^{-2} (3.2)$$

Where  $p_{T,i(j)}$  is the transverse momentum of the cluster i(j) and  $\Delta R_{ij} \equiv \Delta R(i,j)$  the angular distance between the clusters i and j. The jets are formed by comparing these distances and merging the neighboring clusters until either the distance of the new clusters to the jet candidate exceeds the radius parameter R, or a harder cluster which will be assigned to a separated jet is found.

The jets are relevant for the work presented in this thesis as they enter the  $E_{\rm T}^{\rm miss}$  reconstruction (Section 3.6). They are required to have transverse momenta larger than 20 GeV and be within  $|\eta| < 4.5$ . To reduce the effects of pileup in jets with  $p_{\rm T} < 60$  GeV, a Jet Vertex Tagging (JVT) and forward Jet Vertex Tagging (fJVT) [18, 19] algorithm is used for jets with |eta| < 2.4 and  $2.5 < |\eta| < 4.5$ , respectively. The JVT and fJVT uses a multivariate technique to determine the likelihood of the jet originating from the hard-scatter or from pileup. The measured jet energy scale (JES) is corrected using a  $p_{\rm T}$  and  $\eta$  dependent corrections obtained from simulation comparisons [20]. To further suppress jets that do not originate from the hard process a TightBad [21] selection on the jets is imposed with a jet efficiency of 95%. This suppresses contributions from jets that might originate from remnants of calorimeter noise or beam induced background due to proton losses upstream of the interaction point (NCB) or from muons of cosmic showers.

#### 3.5 Tau Reconstruction

The reconstruction of hadronically decaying tau leptons,  $\tau_{\text{had}}$ , is seeded by reconstructed anti- $k_t$  jets as those discussed in Section 3.4. The neutrinos from the tau decays escape the detector without interacting, and that is why the reconstruction algorithm can only reconstruct the visible hadronic parts of the tau decays (denoted as  $\tau_{\text{had-vis}}$ ). The reconstruction of the hadronically decaying tau leptons consists of several steps:

• Tau Vertexing: In events with multiple primary vertices, the default vertex association in ATLAS identifies the PV as the vertex with the largest scalar sum of  $p_{\rm T}^{\ 2}$  of tracks associated with that vertex. However, this vertex does not always correspond to the production vertex of

the tau lepton. The Tau Vertexing algorithm associates the tau's primary vertex (TV) to the PV candidate with the highest scalar sum of transverse momenta of the tracks that lie within the core-cone region ( $\Delta R < 0.2$ ) around the jet barycenter.

- Tau MVA Tracking: When the TV is identified, the  $\tau_{\rm had-vis}$  direction and its tracks parameters with respect to the TV are recalculated. A BDT algorithm uses track information to categorize the tracks within  $\Delta R < 0.4$  around the tau axis into four separate categories ("core", "conversion", "isolation" and "fake" tracks), depending on their origin. The number of the tracks that the algorithm associates to the real charged hadron products of the tau decay ("core" tracks), identify the "prongness" of the reconstructed taus. Thus, taus are classified as "1-prong" if they have only one associated "core" track, or "3-prong" if they have three associated "core" tracks. Compared to the previous cut-based method for tau tracking, the MVA tracking improved significantly the correct classification of tau tracks at high- $p_T$ . As an example, for taus with visible  $p_{\rm T}$  above 500 GeV (1 TeV), the MVA tracking achieved a combined  $^1$  reconstruction efficiency of 72% (69%) compared to the cut-based algorithm 59% (52%). This improvement originates from the implicit requirement on the number of pixel hits by the track in the cut-based method  $(N_{\rm Sil} \ge 2)$ . Thus, in the cut-based tracking, the very boosted taus that managed to traverse the detector and decay after the 2nd innermost layer of the Inner detector would be mis-reconstructed as "0-prong". MVA tracking achieved the partial recovery of those boosted tau leptons.
- Tau Calibration: After the τ<sub>had-vis</sub> have their tracks classified, their energies are calibrated as described in [22]. This correction firstly subtracts effects in the energy that are coming from the pileup and the detector response. Then the tau energy scale (TES) correction is derived by combining this corrected energy with a boosted regression tree to determine the final τ<sub>had-vis</sub> energy.
- **Tau Identification:** The tau reconstruction alone does not provide an adequate rejection against jet or electron backgrounds. Rejection against those backgrounds is achieved in separate identification steps.

Fragmentation and hadronization of quark or gluons also results in reconstructed jets that can be wrongly reconstructed as  $\tau_{\text{had-vis}}$  objects. To reject this jet background, a Recurrent Neural Network (RNN) algorithm is trained to discriminate between  $\tau_{\text{had-vis}}$  and quark/gluon-initiated jets from dijet events [23]. The RNN-based tau identification (ID) has been separately trained for 1-prong and 3-prong  $\tau_{\text{had-vis}}$  decays. Cuts on the resulting tau-jet RNN score discriminant are then parametrized with respect to the  $\tau_{\text{had-vis}}$   $p_{\text{T}}$ , so that a uniform signal efficiency can be achieved. Four working points are provided by the ATLAS; namely VeryLoose, Loose, Medium and Tight. This analysis uses  $\tau_{\text{had-vis}}$  objects that pass the Loose ID working point, which corresponds to 85% (75%) signal efficiency and background efficiency of 4.8% (1.1%) for 1-prong (3-prong)  $\tau_{\text{had-vis}}$ . Control regions are defined by selecting  $\tau_{\text{had-vis}}$  objects that pass the VeryLoose ID requirement.

Electrons can also be misidentified as  $\tau_{had}$  objects as they have single tracks pointing to energy deposits in the calorimeter. To suppress the electron background a Boosted Decision Tree (BDT)

<sup>&</sup>lt;sup>1</sup> The combined efficiency is measured as the sum of the 1-prong and 3-prong efficiencies weighted by the ratio of their branching ratios (78% for 1-prong and 22% for 3-prong)

algorithm is trained to discriminate between 1-prong  $\tau_{\text{had-vis}}$  signals and electron backgrounds. The resulting BDT distribution is also transformed to give a flat signal efficiency versus  $p_{\text{T}}$ . This analysis uses the *Loose* electron BDT working point, which corresponds to 95% signal efficiency. An additional electron veto (EleOLR) is applied on the 1-prong  $\tau_{\text{had-vis}}$ , which aims to reject  $\tau_{\text{had}}$  objects that are near ( $\Delta R < 0.2$ ) to preselected electrons that pass the *VeryLoose* LLH electron identification (Section 3.3).

Finally, this analysis selects the leading- $p_{\rm T}$   $\tau_{\rm had\text{-}vis}$  object that has transverse momentum of at least 30 GeV and is reconstructed within the detector region of  $|\eta| < 2.4$  (excluding the barrel-endcap transition region  $|\eta| \in (1.37, 1.52)$ ). The  $\tau_{\rm had\text{-}vis}$  are required to have been associated with 1, 2 or 3 *core* tracks and have charge  $|q| \le 2$ .

## 3.6 Missing Transverse Energy

Because the proton beams travel along the longitudinal direction, the transverse momentum vectors of the particles produced by a collision should add up to zero. However, this assumption does not hold in the presence of weakly interacting particles that do not interact with the detector such as the neutrinos. Neutrinos will effectively traverse the detector without a trace and so will create momentum imbalance in the final state's measured momentum. This momentum imbalance is quantified by the missing transverse momentum (or missing transverse energy),  $\vec{E}_T^{\text{miss}}$ .

The Missing Transverse Energy is reconstructed per event. It is calculated as the negative vectorial sum of the transverse momenta of all the calibrated, high- $p_{\rm T}$  reconstructed objects [24]. Thus, for each object type i (such as electrons, muons etc.), the missing momentum on the x or y-direction is determined as  $E_{x(y)}^{{\rm miss-i}} = -\sum_i p_{x(y)}^i$ . The total missing momentum on each direction is then given by:

$$E_{x(y)}^{\text{miss}} = E_{x(y)}^{\text{miss-e}} + E_{x(y)}^{\text{miss-}\mu} + E_{x(y)}^{\text{miss-}\tau} + E_{x(y)}^{\text{miss-jet}} + E_{x(y)}^{\text{miss-soft}}$$
(3.3)

In order to improve the missing transverse energy resolution, jets that are classified as originating from pileup by the JVT or the forward JVT  $^2$  [25] (fJVT) algorithms are not considered in the  $E_{x(y)}^{\text{miss-jet}}$ . A Track-based Soft Term (TST),  $E_{x(y)}^{\text{miss-soft}}$ , is added to account for reconstructed tracks that were not matched on any object. The TST algorithm provides a robust determination of the soft-track term against varying pileup but misses the contribution of neutral particles.

It is more useful to represent the missing transverse momentum in polar coordinates, with the magnitude  $E_{\rm T}^{\rm miss}$  and angle  $\phi^{\rm miss}$  given by:

$$E_{\rm T}^{\rm miss} = \sqrt{(E_x^{\rm miss})^2 + (E_y^{\rm miss})^2} \ , \quad \phi^{\rm miss} = \arctan\left(\frac{E_y^{\rm miss}}{E_x^{\rm miss}}\right)$$
(3.4)

# 3.7 $E_{\mathsf{T}}^{\mathsf{miss}}$ trigger reconstruction algorithms

This search uses the  $E_{\rm T}^{\rm miss}$  triggers to select interesting events. It is necessary for the trigger reconstruction algorithms to provide fast decisions about the recorded events. For that reason, the

<sup>&</sup>lt;sup>2</sup> The forward jet vertex tagger aims to classify jets originating from pileup in the region 2.5 <  $|\eta|$  < 4.5

 $E_{\rm T}^{\rm miss}$  triggers use a different approach to reconstruct the  $E_{\rm T}^{\rm miss}$  compared to the more sophisticated approach used at the analysis level.

The L1- $E_{\rm T}^{\rm miss}$  trigger calculates the  $E_{\rm T}^{\rm miss}$  by combining towers of  $\Delta\phi \times \Delta\eta \approx 0.1 \times 0.1$  of energy deposits above a threshold <sup>3</sup> inside "jet elements" of approximate granularity  $\Delta\phi \times \Delta\eta \approx 0.2 \times 0.2$ . The L1- $E_{\rm T}^{\rm miss}$  vector is then calculated as the negative vector sum of the x and y of the jet elements' transverse momenta. The lowest unprescaled triggers used in this search require the missing transverse momentum efficiency to be at least 50 GeV or 55 GeV.

In the HLT several algorithms and combinations were used during the period of data collection to adjust the rates. The algorithms used for triggering events in this analysis are:

- **mht**: During the years 2015-2016, the mht was the baseline algorithm for the HLT- $E_{\rm T}^{\rm miss}$  calculation. The mht-algorithm calculates the  $E_{\rm T}^{\rm miss}$  as the negative sum of the momenta of all the calibrated jets (with uncalibrated  $p_{\rm T} > 7~{\rm GeV}$ ) of the event. During calibration, the pile-up contribution to the jets is corrected on average by using the jet area-based pile-up suppression method [26]. The energy deposited by photons, electrons or hadronically decaying tau leptons is included in the jet reconstruction.
- cell: The cell-algorithm calculates the HLT- $E_{\rm T}^{\rm miss}$  as the negative sum of all cells in the calorimeter without object calibrations or pile-up corrections. The pile-up and electronic noise is suppressed by requiring the signal energy within a cell to be higher than a given threshold. The threshold is determined as the expectation of noise and pile-up before the data taking. Cells with spurious large negative signals are also ignored.
- **pufit**: The pufit-algorithm performs a fit in order to constrain the summed transverse energy components that originate from pile-up near 0 (within fluctuations), and then proceeds in calculating the  $E_{\rm T}^{\rm miss}$  as the negative vectorial sum of the pile-up subtracted high-energy deposits.

During the years 2017-2018, the baseline triggers utilized a combination of the cell-based and pufit-algorithms. During the year 2017, the triggers required the cell-based  $E_{\rm T}^{\rm miss}$  value to exceed 50 GeV and the pufit-based  $E_{\rm T}^{\rm miss}$  to exceed 110 GeV. In the year 2018, the trigger's cell-based  $E_{\rm T}^{\rm miss}$  increased to 65 GeV and 70 GeV depending on the instantaneous luminosity while the lowest pufit-based  $E_{\rm T}^{\rm miss}$  requirement remained at 110 GeV. The triggers and the corresponding integrated luminosity are given in Tab. 3.1.

<sup>&</sup>lt;sup>3</sup> The threshold varies from 1 GeV to 9 GeV and aims to reduce effects originating from pile-up and noise. Thus, it is parametrized separately for the ECAL and HCAL towers as a function of pile-up conditions and pseudorapidity.

Year	Trigger	Luminosity $(pb^{-1})$
2015	HLT_xe70_mht	3219.56
2016	HLT_xe90_mht_L1XE50 HLT_xe110_mht_L1XE50	10748.89 22246.55
2017	HLT_xe110_pufit_L1XE50 HLT_xe110_pufit_L1XE55	38918.26 5388.93
2018	HLT_xe110_pufit_xe70_L1XE50 HLT_xe110_pufit_xe65_L1XE50	6428.44 52021.82
	Total Luminosity:	138972.45

Table 3.1: The lowest unprescaled  $E_{\rm T}^{\rm miss}$  triggers used for each period of data taking and their corresponding integrated luminosity.

## 3.8 Overlap Removal

The reconstruction algorithms discussed in this chapter run in parallel over each event. This can result in ambiguities between energy deposits that were assigned to different objects. This ambiguity is solved by the overlap removal, which assigns priorities upon reconstructed objects and removes reconstructed objects that overlap. ATLAS provides tools that solve the ambiguity for different working points. For the work presented in this analysis, the Standard working point was used, the priorities of which are summarized in Tab. 3.2.

Reject	Against	Criteria
Electron	Electron	shared track, $p_{T,1} < p_{T,2}$
Tau	Electron	$\Delta R < 0.2$
Tau	Muon	$\Delta R < 0.2$ and if $p_{\rm T}^{\tau} > 50$ GeV is Combined-Muon
Muon	Electron	is Calorimeter-tagged Muon and shared Inner Detector track
Electron	Muon	shared Inner Detector track
Photon	Electron	$\Delta R < 0.4$
Photon	Muon	$\Delta R < 0.4$
Jet	Electron	$\Delta R < 0.2$
Electron	Jet	$\Delta R < 0.4$
Jet	Muon	$N_{\rm track} < 3$ and (ghost-associated or $\Delta R < 0.2$ )
Muon	Jet	$\Delta R < 0.4$
Jet	Tau	$\Delta R < 0.2$
Photon	Jet	$\Delta R < 0.4$

Table 3.2: The "Standard" working point priorities for the ATLAS overlap removal tool.  $\Delta R$  denotes the angular separation between the objects. The term "ghost-associated", refers to cases where the muon track was associated with one of the soft tracks of the jet.

# 3.9 Preselection summary

Feature	Electron	Muon
Pseudorapidity range Transverse momentum	$ \eta  < 2.47 \text{ (excl. [1.37, 1.52])}$ $p_{\text{T}} > 20 \text{ GeV}$	$ \eta  < 2.5$ $p_{\rm T} > 20 {\rm GeV}$
Object quality Track to vertex association Identification Isolation	Not from a bad calorimeter cluster $d_0^{\rm sig} < 3$ $z_0 \sin \theta < 0.5  {\rm mm}$ LH Loose Fixed (Loose)	$-\frac{d_0^{\rm sig} < 3}{z_0 \sin \theta < 0.5  \rm mm}$ $Loose$ $TightTrackOnly\_FixedRad$
	Jet	
Pseudorapidity range Transverse momentum	$  \eta  < 4.5 $ $p_{\rm T} > 20  {\rm GeV} $	
Object Quality	TightBad	
JVT cut for $p_{\rm T}$ <60 GeV and $ \eta $ < 2.4 fJVT cut for $p_{\rm T}$ <60 GeV and 2, 4 < $ \eta $ < 4.5	> 0.59 applied	
71	Tau	
Pseudorapidity range Transverse momentum	$ \eta  < 2.4 \text{ (excl. [1.37, 1.52])}$ $p_{\text{T}} > 30 \text{ GeV}$	
"Core" tracks Absolute charge	$ \begin{array}{c c} 1 \text{ or } 2 \text{ or } 3 \\  q  < 2 \end{array} $	
Identification Jet-rejection Electron-rejection	RNN <i>Loose</i> BDT <i>Loose</i>	

Table 3.3: The object selection criteria used in for the reconstructed objects in this thesis.

# **Theory**

#### 4.1 The Standard Model

The Standard Model of particle physics (SM) is the theoretical framework describing the behavior and interactions of elementary particles, the fundamental constituents of the observable universe. Since the 1960s, the SM has made numerous predictions, many of which have been experimentally verified with remarkable precision, establishing it as one of the most well-tested theories in physics. As a quantum field theory, the SM portrays particles as excitations of underlying quantum fields.

The SM particles are grouped into two main categories: the *matter particles* and the *force-carrier particles*. The *matter particles* are the particles that form the structures that are realized as matter in the universe. The *force-carrier particles* are, as the name suggests, the particles responsible for the particle interactions.

An important concept in physics, particularly in quantum theories, is that of symmetries. Symmetries are associated with conserved quantities via Noether's theorem. The way symmetries are realized in nature is through transformations. In the following section, a certain type of symmetries present in the SM, namely the gauge symmetries, are described.

## 4.2 The gauge symmetries of the Standard Model

One key concept in the SM is local gauge symmetries. In a local gauge transformation, the matter fields have their inner degrees of freedom transformed with angles that depend on the spacetime point. Over time, the SM evolved in a gauge theory with symmetry group  $SU_c(3) \times SU_L(2) \times U_Y(1)$ . This symmetry is spontaneously broken on the electroweak energy scale (approximately  $u_F = 246 \, \text{GeV}$ ) to  $SU_c(3) \times U_{EM}(1)$  through the Higgs mechanism.

Symmetries are reflected in the action (S) formalism, where a symmetry is a transformation that leaves the action unchanged. The action S is the time integral of the Lagrangian L:

$$S = \int L(x,t)dt = \int \mathcal{L}(x,t)d^4x ,$$

where  $\mathcal{L}$  is the Lagrangian density and  $d^4x$  is the measure of the spacetime coordinates. Similarly to classical mechanics, the Lagrangian contains information on the kinetic and potential energy of the fields.

The Lagrangian density for the non-interacting fields depends on the spin. The fields of particles with spin-0 (scalar fields), denoted  $\phi$ , are described by the Klein-Gordon equation. Fields of spin-1/2 particles (fermion fields), denoted  $\psi$  by the Dirac equation. Finally, the spin-1 particles (vector fields),  $A_{\mu}$ , by the generalization of the Proca equation.

$$\mathcal{L}_{Klein-Gordon} = (\partial_{\mu}\phi)(\partial^{\mu}\phi) - \frac{m_{S}^{2}}{2}\phi^{2}$$
(4.1)

$$\mathcal{L}_{Dirac} = i\bar{\psi}\gamma^{\mu}\partial_{\mu}\psi - m\bar{\psi}\psi \tag{4.2}$$

$$\mathcal{L}_{Poca} = -F_{\mu\nu}F^{\mu\nu} + \frac{m_V^2}{2}A_{\mu}A^{\mu}, \tag{4.3}$$

where  $\partial_{\mu} = \frac{\partial}{\partial x^{\mu}}$ , m the mass of the field,  $\gamma^{\mu}$  the Dirac matrices,  $\bar{\psi} = \psi^{\dagger} \gamma^{0}$  and  $F_{\mu\nu} = \partial_{\mu} A_{\nu} - \partial_{\nu} A_{\mu}$ .

#### 4.2.1 The Strong Interaction

#### **Proton structure**

Unlike the fundamental particles, protons are composite particles made up of three valence quarks: two up quarks and one down quark. These quarks determine the positive charge of the proton. The strong force, mediated by gluons, binds the quarks together, allowing virtual quark-antiquark pairs and additional gluons to appear briefly.

In the parton model, protons contain not only valence quarks but also sea quarks and gluons, which collectively are called *partons* and carry the proton's momentum. During high-energy proton collisions, the partons interact. The cross-section of the interacting protons A,B to produce the outcome Y,  $\sigma_{AB\to Y}$ , can be expressed by:

$$\sigma_{AB\to Y} = \int dx_a dx_b f_{aA}(x_a, Q^2) f_{bB}(x_b, Q^2) \sigma_{ab\to Y}$$
 (4.4)

In the above equation, the following terms appear:

- $\sigma_{ab\to Y}$ : the cross-section of the interacting partons a, b to produce the outcome Y,
- $x_{a(b)}$ : the momentum fraction carried by the partons a(b) in the proton,
- $f_{aA}(x_a, Q^2)$ : the probability of the parton a to exist in the proton A with momentum fraction  $x_a$  (and equivalently for b).

The latter probabilities are called the parton distribution functions (PDFs) of the proton. The PDFs also depend on the type of the parton and on the transferred momentum,  $Q^2$ , of the scattering process. The PDFs cannot be theoretically calculated. Instead, they are measured in collider experiments, by observing processes of with known cross-sections at a fixed value of  $Q^2$ . A functional form for the cross-section including a parametrization of the PDF is then fitted to the measured cross-section. The PDFs are measured from experiments at a particular scale  $Q^2$  and are extrapolated to all values of  $Q^2$  using the Dokshitzer-Gribov-Lipatov-Altarelli-Parisi (DGLAP) evolution equations [27, 28, 29].

using the Dokshitzer-Gribov-Lipatov-Altarelli-Parisi (DGLAP) evolution equations [27, 28, 29]. In Fig. 9, the PDFs are shown for  $Q^2 = 10 \text{GeV}^2$  and  $Q^2 = 10^4 \text{GeV}^2$  as a function of x. The PDFs decrease rapidly for higher values of x, reflecting the rarity of observing a single parton inside the

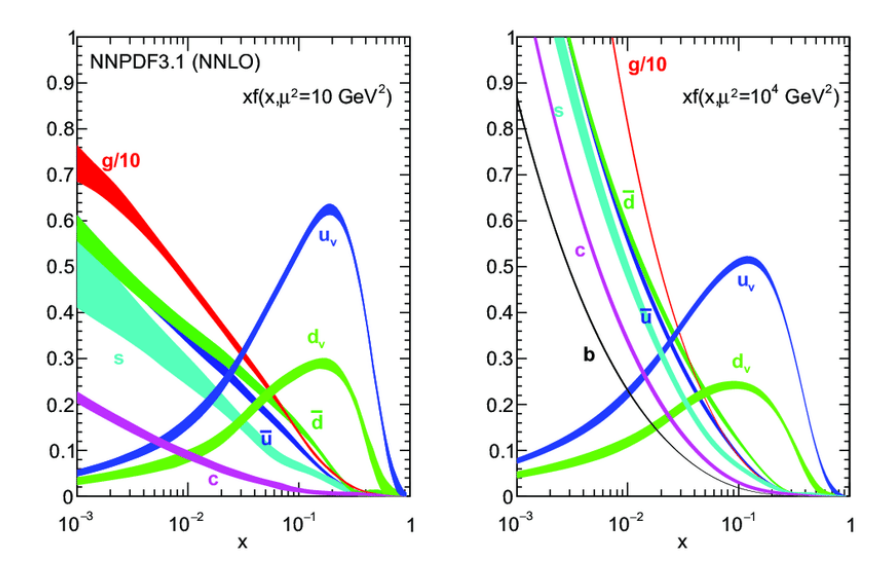


Figure 9: Results of the global fit performed by the NNPDF Collaboration. The PDFs are shown for scales  $Q^2 = 10 \text{GeV}^2$  (left) and  $Q^2 = 10^4 \text{GeV}^2$  (right). The gluon PDF is scaled down by a factor of 10 for visibility. Figure is taken from Ref. [30]

proton that carries most of the proton's momentum. The up- and down-quark peaks, together with their relative ratios, is a consequence of the presence of two and one valance up-quark and down-quark respectively. The rest of the partons types can exist inside the proton carrying a smaller amount of its momentum. The statistical uncertainty of the PDFs in the figure depends on the different kinematic regions as the size of data from which the PDFs were measured varies between them.

#### 4.2.2 Quantum Electrodynamics

Before introducing the electroweak interactions, we first discuss the significance of local gauge invariance in quantum field theory, using  $U_Y(1)$  as an illustrative example. Under such a symmetry group, the matter fields  $\psi$  transform as:

$$\psi \xrightarrow{U(1)} \psi' = e^{-iYa(x)}\psi.$$

where Y is the hypercharge of  $\psi$ , and a(x) is the spacetime-dependent phase parameter. The invariance of the action under any symmetry transformation is satisfied if the Lagrangian density transforms by up to a total derivative. However, the presence of spacetime-dependent phase parameters in the transformation of the matter field, combined with the partial derivative in the Lagrangian density, introduces a term that violates this condition:

$$\mathcal{L} \xrightarrow{U(1)} \mathcal{L}' = i\bar{\psi}\gamma^{\mu}\partial_{\mu}\psi - m\bar{\psi}\psi + Y\bar{\psi}\gamma^{\mu}\psi\partial_{\mu}a(x)$$

By itself, the last term breaks the invariance of the action, as it cannot be written as a total derivative. To restore the gauge invariance, a vector field  $B_{\mu}$  is introduced, and the partial derivative is generalized to the covariant derivative, defined as:

$$D_{\mu} = \partial_{\mu} + iYB_{\mu}$$

The Lagrangian density then becomes:

$$\mathcal{L} = i\bar{\psi}\gamma^{\mu}D_{\mu}\psi - m\bar{\psi}\psi$$

The addition of the vector field restores the gauge invariance by requiring it to transform as:

$$B_{\mu} \xrightarrow{U(1)} B'_{\mu} = B_{\mu} + i\partial_{\mu}a(x)$$

Additionally, having introduced the vector field, we can include additional gauge-invariant terms, as shown in the Lagrangian density of Eq. 4.3. The total Lagrangian density,  $\mathcal{L}_{QED}$ , that obeys the local  $U_Y(1)$  gauge invariance of the action can be written as:

$$\mathcal{L}_{OED} = i\bar{\psi}\gamma^{\mu}_{\mu}\psi - m\bar{\psi}\psi - F_{\mu\nu}F^{\mu\nu}$$

The "QED" subscript in the Lagrangian density only reflects the equivalence of this theory to the Quantum Electrodynamics  $^1$ . In summary, the requirement of local  $U_Y(1)$  gauge symmetry leads to a theory with an additional vector field that can interact with fermionic fields by the term  $Y\bar{\psi}\gamma^{\mu}B_{\mu}\psi$ . It is important to note that the vector field mass term,  $\frac{m_V^2}{2}A_{\mu}A^{\mu}$ , is not included in  $\mathcal{L}_{QED}$  because it is not gauge invariant. In the Standard Model, the gauge bosons acquire masses dynamically through the Spontaneous Symmetry Breaking of the Electroweak group via the Higgs mechanism.

#### 4.2.3 Electroweak Theory and Higgs field

For the Electroweak theory in the Standard Model, the symmetry group is  $SU_L(2) \times U_Y(1)$ , where  $SU_L(2)$  represents the weak isospin and  $U_Y(1)$  corresponds to the hypercharge, Y. The  $U_Y(1)$  transformations act on both left-handed and right-handed fermions, denoted by  $\psi_L$  and  $\psi_R$  respectively. The evaluation of the Standard Model Lagrangian density for those transformations follows a similar approach to the one discussed in Sec. 4.2.2. On the other hand, the  $SU_L(2)$  transformations exclusively act on left-handed fermions, introducing the parity violation in the Standard Model.

Under a local  $SU_L(2)$  transformation, the left-handed fermions transform as:

$$\psi_L \to \psi_L' = e^{it^b a_b(x)} \psi.$$

where  $t^b$  (with  $b \in 1, 2, 3$ ) are the generators of the  $SU_L(2)$  group and  $a_b(x)$  are spacetime-dependent parameters of the transformation.

Following a similar approach as in Sec. 4.2.2, one can write the following Langrangian density that respects the gauge symmetry:

$$\mathcal{L}_{EW} = \left(i\bar{\psi}_L\gamma^\mu D_\mu\psi_L + i\bar{\psi}_R\gamma^\mu D_\mu\psi_R\right) - \frac{1}{4}\left(W^a_{\mu\nu}W^{a\mu\nu} + F_{\mu\nu}F^{\mu\nu}\right),\tag{4.5}$$

where the covariant derivative is given by:

$$D_{\mu} = \partial_{\mu} - igW_{\mu}^b t^b - ig'YB_{\mu} . \tag{4.6}$$

<sup>&</sup>lt;sup>1</sup> The actual QED Lagrangian appears only after the Spontaneous Symmetry Breaking.

In the above expression,  $W_{\mu}^{a}$  are the gauge fields for the  $SU_{L}(2)$  group with coupling strength g, and  $B_{\mu}$  is the gauge field for  $U_{Y}(1)$  with coupling strength g'. The additional terms in the second set of parentheses in Eq. 4.5 include the kinetic and self-interaction terms of the gauge fields  $W_{\mu}^{a}$ ,  $W^a_{\mu\nu} = \partial_\mu W^a_\nu - \partial_\nu W^a_\mu + g \epsilon^{abc} W^b_\mu W^c_\nu$ , where  $\epsilon^{abc}$  is the fully antisymmetric Levi-Civita symbol.

Although the written  $\mathcal{L}_{EW}$  respects the gauge symmetry of the Standard Model, it does not provide mass terms for the fermions or gauge bosons. The  $SU_L(2)$  symmetry forbids mass terms for the fermionic fields, while the inclusion of gauge boson masses would violate the  $SU_L(2) \times U_Y(1)$ symmetry. This is inconsistent with observation, as both massive fermions and gauge bosons are described by the Standard Model.

To resolve this problem, the Standard Model introduces the Higgs field,  $\Phi$ , a complex scalar field that acquires a non-zero vacuum expectation value (VEV). The Higgs field provides a mechanism by which both fermions and gauge bosons can acquire mass, without breaking the underlying gauge symmetry.

The introduction of a scalar field in the theory that transforms as a doublet under the  $SU_L(2)$ , can introduce additional terms in  $\mathcal{L}_{EW}$ :

$$\mathcal{L}_{EW+Higgs} = \mathcal{L}_{EW} + (D_{\mu}\Phi)^{\dagger}(D^{\mu}\Phi) + y_f \bar{\psi}_L \Phi \psi_R - V(\Phi)$$
(4.7)

where  $y_f$  are the Yukawa couplings of the fermions with the Higgs field. The Higgs potential,  $V(\Phi)$ , is given by:

$$V(\Phi) = -\mu^2 \Phi^{\dagger} \Phi + \lambda |\Phi^{\dagger} \Phi|^2, \tag{4.8}$$

where  $\mu^2 > 0$  and  $\lambda > 0$  as free parameters defining the shape of the potential. The minimum of the potential occurs when the field acquires its VEV,  $v = \sqrt{\frac{-\mu^2}{\lambda}}$ .

Using the local gauge invariance and expanding the Higgs field near the minimum of the potential, one obtains:

$$\Phi = \frac{1}{\sqrt{2}} \begin{pmatrix} 0 \\ v + h(x) \end{pmatrix},$$

where h(x) is the Higgs boson. Substituting this expression into  $\mathcal{L}_{EW+Higgs}$  yields mass terms for the fermions, given by  $m_f = \frac{y_f v}{\sqrt{2}}$ . For the gauge bosons, the fields are appropriately redefined as  $\sqrt{2} W_{\mu}^{\pm} = W_{\mu}^{1} \mp i W_{\mu}^{2}$ ,  $Z_{\mu} = \cos \theta_{W} W_{\mu}^{3} - \sin \theta_{W} B_{\mu}$  and  $A_{\mu} = \sin \theta_{W} W_{\mu}^{3} + \cos \theta_{W} B_{\mu}$ . The  $A_{\mu}$  field corresponds to the photon, the  $W_{\mu}^{\pm}$  fields are the charged weak bosons, and the  $Z_{\mu}$  field is the neutral weak boson. The masses of those fields are then calculated:

$$m_A = 0 \tag{4.9}$$

$$m_{W^{\pm}} = \frac{gv}{2} \tag{4.10}$$

$$m_{W^{\pm}} = \frac{gv}{2}$$
 (4.10)  
 $m_{Z} = \frac{m_{W}}{\cos \theta_{W}},$  (4.11)

where  $\theta_W$  is the Weinberg angle, defined by  $\cos \theta_W = \frac{g}{\sqrt{g^2 + g'^2}}$ .

# 4.3 Beyond the Standard Model

The SM has been remarkably successful in describing the strong and electroweak interactions described above, as it has accurately predicted the particle interactions to an impressive degree. However, there are several open questions in the model and compelling reasons to search for theories beyond the SM. The origin of neutrino masses is such a question in the SM is the origin of neutrino masses. Neutrinos are observed to oscillate between flavors, which implies they must have non-zero masses [31]. However, the SM treats the neutrinos as massless and does not provide a mechanism for generating these masses. New physics is needed to explain why neutrino masses are so small and how they arise, with possibilities ranging from right-handed neutrinos to the seesaw mechanism.

Further motivation for searching for physics beyond the SM comes from the hierarchy problem, which questions the smallness of the Higgs boson's mass (125 GeV) in comparison to the natural cut-off scale of the SM, namely the Planck scale (10<sup>19</sup> GeV). To keep the Higgs mass as small as the observed value, the SM requires a high degree of fine-tuning, which many find unnatural. Theories like supersymmetry and little Higgs model [32] aim to resolve this issue by protecting the Higgs mass from the large quantum corrections.

Moreover, precision measurements in particle physics have exposed small, yet persistent, discrepancies with SM predictions. For instance, the anomalous magnetic moment of the muon shows a deviation from theoretical predictions, hinting at new particles or interactions beyond those known in the SM [33, 34]. Additionally, discrepancies in certain decays involving flavor-changing interactions, which could indicate new physics at play in flavor dynamics [35].

Finally, the SM cannot explain the matter-antimatter asymmetry observed in the universe [36]. Although the SM includes some mechanisms (CP-violating processes) for generating this asymmetry [37], they are insufficient to account for the observed dominance of matter over antimatter. Instead, a fundamental theory may include new sources of CP violation that could provide a more complete picture of the origin of this imbalance [38].

Each of the above examples represents a key frontier in modern physics, encouraging searches for new particles and symmetries that could lead to a more comprehensive understanding of the fundamental behavior of our universe.

#### 4.3.1 Heavy Gauge Boson models

The above problems and some of their suggested solutions include larger symmetries, that contain the SM, or extend the SM with new additional symmetries. These symmetries result in the presence of additional heavy gauge bosons in analogy to the SM ones. Some such models are briefly described below:

• Non-Universal Gauge Interaction Models: The Non-Universal Gauge Interaction Models [39, 40, 41, 42] (NUGIM) can possibly explain the mass hierarchy of fermions and the observed discrepancies of Lepton Flavor Universality. For example, the TopFlavor model [43] provides a dynamical explanation to large mass gaps between the fermion generations. In the simplest form, the NUGIM proposes an extended gauge symmetry of SU₁(2) ⊗ SU₂(2) × U(1) for the SM. This symmetry can facilitate different interactions between the third generation of fermions (denoted by the subscript 1) and the first and second generation of fermions (denoted by the subscript 2). The breaking mechanism of this model may vary, but in all cases it introduces new

heavy gauge bosons, neutral Z' and charged W', which can exhibit enhanced couplings to the third generation of fermions, such as the  $\tau$ -leptons. As these models are more relevant for this search, additional information can be found in Sec. 4.4.3.

- Left-Right Symmetric Models: The Left-Right Symmetric Model [44] (LRSM) extends the SM Electroweak sector by an extra  $SU_R(2)$  which introduces right-handed interactions in analogy to the left-handed weak interactions. In doing so, this model predicts the existence of additional heavy gauge bosons  $Z_R$ ,  $W_R$  once the breaking of the  $SU_R(2)$  occurs. The LRSM also provides a natural mechanism for the neutrinos to acquire mass through the see-saw mechanism and the presence of heavy right-handed neutrinos.
- Little Higgs Model: The Little Higgs model [45] proposes a solution to the hierarchy problem, viewing the Higgs as a pseudo-Goldstone boson of a new, larger symmetry group such as SU(5) that is only broken at low energies (order of 10 TeV). The symmetry is broken into various  $SU(2) \otimes U(1)$  groups, which are later mixed and broken to give the SM symmetry group. The extra degrees of freedom of the mixing and breaking of the extra groups become the heavy gauge bosons Z' and W'.

Since several theories can predict additional heavy gauge bosons, a benchmark model is commonly used to assess the discovery potential of a specific channel. The Sequential Standard Model [46] (SSM) is such a benchmark model, and assumes universal couplings between the extra gauge bosons W'/Z' and all the fermion generations.

# 4.3.2 Experimental exclusion of Heavy gauge bosons

This section summarizes only a subset of relevant W' searches undertaken by experiments. A general overview can be found in Ref. [47].

The ATLAS experiment has searched for W' bosons in the light-lepton,  $W' \to \ell \nu$  ( $\ell = e, \mu$ ) [48], and  $\tau$ -lepton,  $W' \to \tau \nu$  [49], channels. The light-lepton searches generally have a better sensitivity than  $W' \to \tau \nu$ , especially for models with universal couplings to fermions because they suffer from less SM background and are enhanced by better lepton reconstruction and identification efficiency. With an integrated luminosity of 139 fb<sup>-1</sup> recorded at a center-of-mass energy of  $\sqrt{s} = 13$  TeV, the ATLAS light-lepton search excluded W' bosons in the SSM with masses up to 6.0 TeV [48] at 95% confidence level (CL).

The signatures originating from  $W' \to \tau \nu$  decays in the detectors at LHC are mainly the hadronic decay products of a high-momentum  $\tau$ -lepton and large missing transverse momentum. The missing transverse momentum originates from the prompt neutrino of the W' decay and the neutrino from the subsequent  $\tau$ -lepton decay. The CMS experiment has searched for  $W' \to \tau \nu$  decays in data collected during the years 2015–2018 and excluded W' bosons in the SSM with masses up to 4.8 TeV [50] at 95% CL.

The leptonic tau decays are experimentally challenging, as they have the same (light-leptons) but softer visible products as the mono-lepton searches, and more smeared missing transverse momentum due to the presence of the two neutrinos from the tau leptonic decay. At the same time, they only account for a small fraction (35%) of the total branching ratio, and thus they are neglected. More details can be found in Ref. [51].

Decays of the W' boson into tb final states are also relevant for probing third generation couplings. The ATLAS experiment has performed searches for  $W' \to tb$  decays using 139fb<sup>-1</sup> of data, excluding W' masses below 4.2 TeV at 95% CL[52]. Similarly, the CMS experiment has conducted a search focusing on leptonic top-quark decays, excluding W' masses below 3.9 TeV at 95% CL [53]. In addition, reinterpretations of qq resonance searches [54, 55] by both collaborations have placed constraints on W' masses, with the ATLAS excluding SSM W' masses below 4 TeV at 95% CL.

Exclusion limits on the masses of the new heavy gauge bosons as a function of the parameter  $\cot \theta_E$  can also be derived by indirect searches. The most stringent limits are derived from electroweak precision measurements (EWPT) [56] and by the absence of lepton flavor violation (LFV) in the SM [57]. They exclude W' bosons with masses below 1.8–2.5 TeV, depending on the coupling. Weaker limits can be set either from tests of the unitarity of the Cabibbo–Kobayashi–Maskawa (CKM) matrix [58] or low-energy constraints and the Z-pole data at LEP [39].

## 4.4 Simulation

#### 4.4.1 Introduction

Due to the quantum nature of the particles inside the proton, predicting the outcome of *pp*-collisions requires knowledge and understanding of the underlying probabilities of possible interactions that may occur at the collision. This is achieved through simulations, which briefly consist of the following conceptual steps:

- Hard Scattering: The simulation process begins with hard scattering, which models the original, high-energy collision between the partons of the colliding protons. The hard scattering step calculates the probability of each process by evaluating all relevant Feynman diagrams using perturbative QCD or EW theory when photons or weak bosons are involved. The simplest Feynman diagram describing the process is referred to as the Leading Order (LO) contribution to the process's Matrix Element (ME). Additional diagrams, which include extra vertices representing radiative corrections, lead to higher-order calculations that improve the precision of the simulation, such as Next-to-Leading Order (NLO) or Next-to-Next-to-Leading Order (NNLO) accuracy in MC generators. The amount of computation time and resources increases dramatically for higher orders, and for that reason most simulation programs do not exceed the NLO precision. The scale  $\mu_R$  (renormalisation scale) is protecting the theory from ultraviolate (UV) divergences appearing from loops with large momentum transfers and describes the scale at which the coupling constant  $a_S$  is evaluated. The scale  $\mu_F$  (factorisation scale) is another cut-off which protects the theory from infra-red (IR) divergences that occur due to the presence of very soft (zero-momentum) particles. The choice of the factorization scale is arbitrary and is usually set equal to the renormalisation scale,  $\mu_F = \mu_R = \mu$ .
- **Parton Shower**: The following step is the parton shower. Here, the high-energy quarks and gluons from the primary event undergo successive splittings, emitting softer quarks or gluons as they lose energy. The goal of the parton shower is to model the cascade of QCD radiation and simulate the many soft particles produced that the original hard scattering could not calculate <sup>2</sup>.

<sup>&</sup>lt;sup>2</sup> Cases where the calculation may not work could be for collinear and infrared radiation from a quark, or higher-order QCD corrections.

That way, the parton shower can capture the "jet-like" structure outcomes that are typical at the high-energy collisions.

- **Hadronization**: The outcome of the parton shower is the set of low energy gluons and quarks. As quarks and gluons cannot exist free in nature, the hadronization step combines them into colorless hadrons. This step is non-perturbative and relies on phenomenological models [59, 60].
- **Simulation**: After the hadronization, the detector simulation is applied to model how the actual detector would respond to the resulting particles. The software simulates the particle interactions with detector components. This process generates simulated readout data, which includes energy deposits in calorimeters, hits in tracking detectors, and responses in other detector parts,
- **Reconstruction**: Finally, as is done with real data, the simulated detector readout is used by the main reconstruction algorithms to produce reconstructed physics objects in simulation.

#### 4.4.2 Backgrounds

Monte Carlo (MC) simulation is used to estimate signal efficiencies and some background contributions. The relevant SM processes that contribute to background in this search are summarized as follows:  $W(\to \tau \nu) + jets$ ,  $W(\to \ell \nu) + jets$ ,  $Z(\to \tau \tau) + jets$ ,  $Z(\to \ell \ell) + jets$ ,  $Z(\to \ell \ell) + jets$ ,  $Z(\to \ell \ell) + jets$ , and diboson. Figures 10, 11, 12, 13 illustrate a few possible Feynman diagrams for the production and decay of each background. Processes of  $Z(\to \nu \nu) + jets$  were also generated for cross-checks with the fake background originating from jets.

Events where the selected tau candidate is not matched to a truth electron, muon or tau are assumed to have the tau candidate originating from a truth jet. This truth match is performed via a  $\Delta R$  match between the reconstructed  $\tau_{\text{had-vis}}$  4-momentum and the visible 4-momentum of the truth tau, electron or muon (up to a threshold of  $\Delta R = 0.2$ ).

Details about the simulation of the samples can be found in Table 4.1. All generated events are propagated through a detailed Geant4 simulation [61] of the ATLAS detector and subdetector-specific digitisation algorithms [62] and are reconstructed with the same algorithms as the data. Pileup is simulated by overlaying minimum-bias interactions on the generated events. The simulated events are later reweighted to match the pile-up profile observed in data. The simulations are normalized to the data luminosity and their respective cross-sections after applying higher-order QCD and Electroweak corrections via k-factors. Mass-dependent k-factors are used as weights for the W/Z-boson processes. These k-factors correct the QCD and EW calculations to NNLO and NLO respectively.

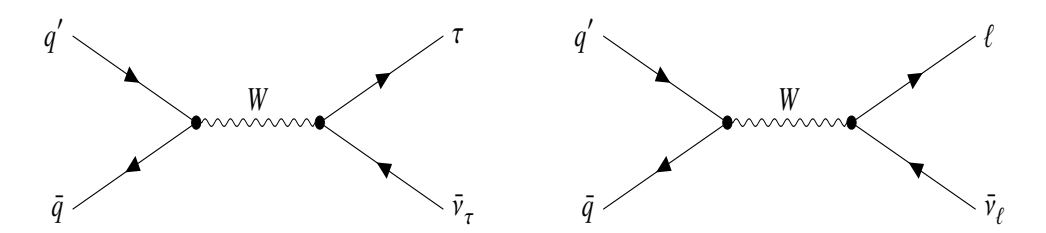


Figure 10: The Feynman diagram for the production of charged W-boson that decays to a tau lepton (left) and light lepton (left) and its neutrino during a pp-collision. The offshell  $W \to \tau \nu$ , is the main background in this analysis. The cases where the light lepton is wrongly reconstructed as a tau lepton the diagram on the left can be part of this analysis background.

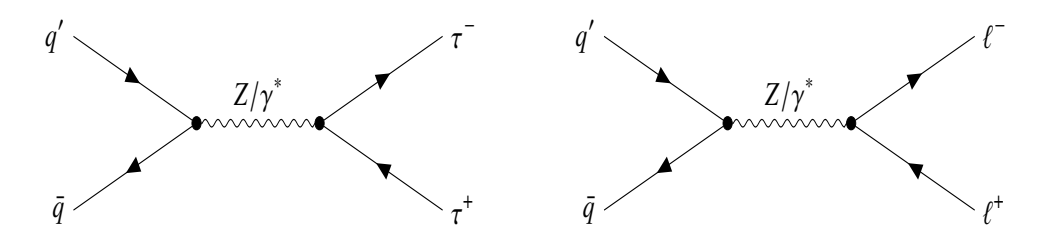


Figure 11: The Feynman diagram for the production of neutral  $Z/\gamma^*$ -boson that decays to a pair of tau leptons (left) and light leptons (right) during a pp-collision. Cases where the leptons are wrongly reconstructed as tau leptons, and one of the tau leptons fails the reconstruction, these process can be a background for the W' search.

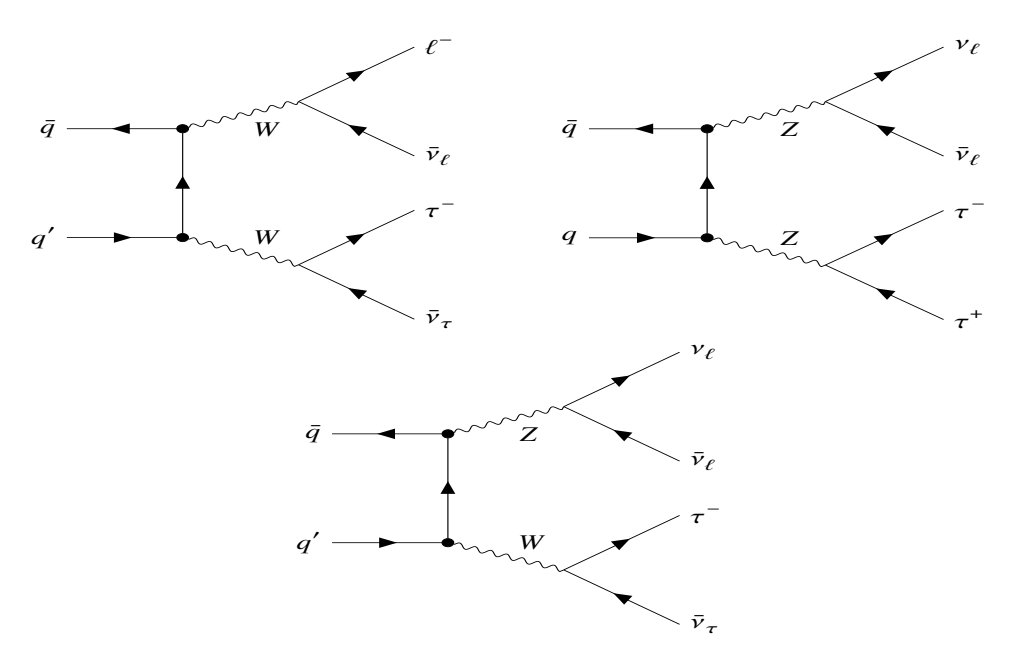


Figure 12: Some Feynman diagrams for the production of dibosons WW (top left) or ZZ (top right) and WZ (bottom) that can decay to leptons during a pp-collision. The presence of tau-lepton(s) in the final state suggests that the relevant process can be a background for the W' search.

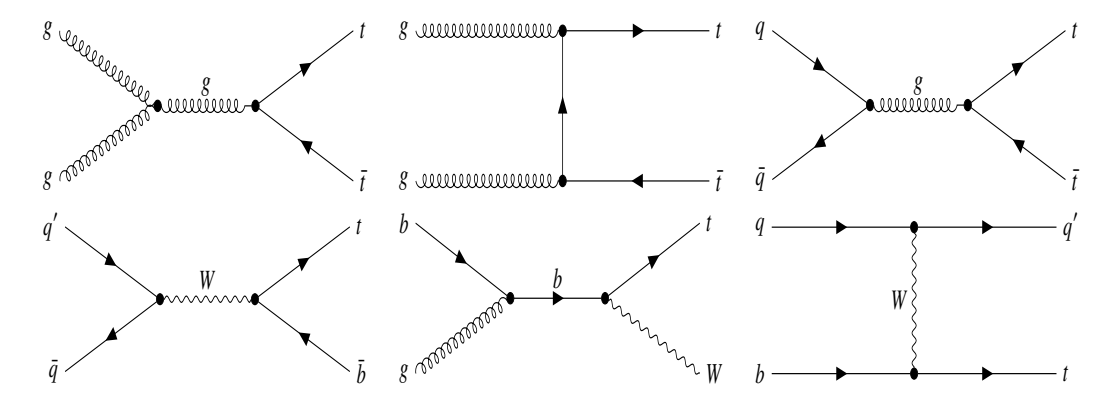


Figure 13: Some Feynman diagrams for the production of  $t\bar{t}$  (top) and single-top (bottom) during a pp-collision. The top-quarks decay instantly giving a Wb. Depending on the decay of the W, the  $t\bar{t}$  can be a background for the W' search.

### 4.4.3 Signal

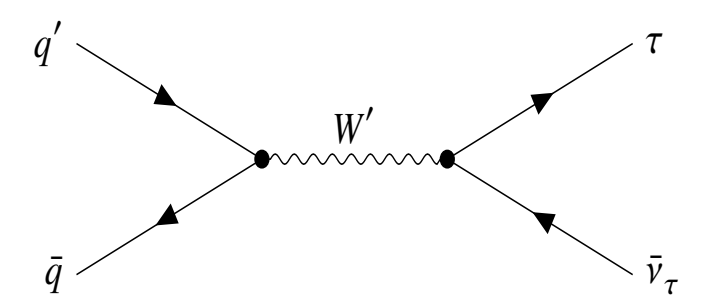


Figure 14: Feynman diagram of the production and decay of a W' to  $\tau \nu$  during a pp-collision.

A flat signal sample  $W' \to (\tau \to \tau_{\rm had} \nu) \nu$  was produced at LO (Fig. 14) using the Pythia-8 Event Generator. The term "flat" in this context indicates that the sample has nearly equal statistical power across all values of the parameter of interest, ensuring sufficient event production for various regions of the W invariant mass spectrum ( $m_{\tau\nu}$ ). The A14 NNPDF23LO tune was applied. The tau polarization is correctly treated by Pythia-8 interfaced with TAU0LA++  $\nu$ 2.9. The generated events were subsequently simulated using ATLFASTII [80] (AF2), which employs a full Geant4 simulation for particle tracks (in the inner detector and muon spectrometer) alongside a faster simulation for calorimeter response.

The event generation followed the same standard approach as the  $W' \to \ell \nu$  search, where the Breit-Wigner resonance peak was removed at generation. Also, to achieve the "flatness" the statistical uncertainty of the MC events weights does not depend on the invariant mass. This is achieved by weighting the events during the generation by appropriate weights, f(x), defined by:

$$\frac{1}{f(x)} = \begin{cases}
\frac{1.0}{102.77} \times 10^{12} e^{-11.5x} & x < 0.023 \\
1.0 \times 10^{12} e^{-16.1x + 1.2 \log x} & 0.023 \le x < 0.231, & \text{where } x = \frac{m_{\tau \nu} [\text{TeV}]}{13 \text{TeV}} \\
\frac{1.0}{1.8675 \cdot 10^{-4}} \times 10^{12} e^{-31.7x + 4.6 \log x} & 0.231 \le x
\end{cases} (4.12)$$

In addition to the weights mentioned above, the Breit-Wigner peak can be reproduced using the corresponding formula to generate a signal with a specified pole mass  $m'_{W}$ :

$$B(m_{\tau \nu}; M) = \frac{1.0}{(m_{\tau \nu}^2 - M^2)^2 + (m_{\tau \nu}^2 \Gamma(M)/M)^2} , \qquad (4.13)$$

where the  $\Gamma(M)$  is the width of the W'.

Also higher-order QCD corrections in the form of mass-dependent k-factors are applied to the signal. Electroweak corrections are expected to be model-dependent and are not considered. For invariant masses  $m_{\tau\nu} > 9.5$  TeV the signal's expectation is set to 0 because no valid k-factors are available above this threshold.

The Family Model and non-universal G(221) (NU) model are two models that contain W' and Z'

4.4 Simulation

Table 4.1: Details of the generators and software packages used to simulate the background samples, including the generation of the matrix element and the corresponding PDF set as well as the modeling of non-perturbative effects such as parton showers, PDF set and MC tune.

Process	Generator	ME order	PDF	Parton Shower	Tune
W/Z+jets	Powнeg-Box [v1] [63, 64, 65, 66]	NLO	CT10nlo [67]	Рутніа [8.186] +CTEQ6L1 [69]	AZNLO [68]
$tar{t}$	Powнеg-Box [v2] [70, 63, 64, 65]	NLO	NNPDF3.0nlo [71]	Рутніа [8.230] +NNPDF2.3Lo	A14
Single top	Powheg-Box [v2] [72, 63, 64, 65]	NLO	NNPDF3.0nlo	Рутніа [8.230] +NNPDF2.3L0	A14
Diboson $Z(\rightarrow \nu\nu)+jets$	Sherpa [2.2.1] or 2.2.2 [73] Sherpa [2.2.1]	MEPS@NLO [74] MEPS@NLO	NNPDF3.0nnlo [71] NNPDF3.0nnlo	Sherpa [75, 76, 77, 74, 78, 79] Sherpa	Sherpa Sherpa

with enhanced couplings to third generation fermions. Both models exhibit the same extended gauge group  $SU_1(2) \times SU_2(2) \times U_Y(1)$  which is first broken to the Standard Model  $SU_L(2) \times U_Y(1)$  at some high energy scale, u, by a bi-doublet scalar field  $\eta$ , and is then broken to  $U_{EM}(1)$  at the Electroweak scale v by a Higgs mechanism. It is typical to defined  $\epsilon = \frac{v}{u} \approx M_W/m_{W'}$ , to characterize the small corrections to the couplings. The main difference between the two models is in the symmetry breaking at v, at which the Family Model employs a 2-Higgs Double Models (2HDM) with one Higgs doublet charged under the heavy  $SU_2(2)$  and a second Higgs doublet charged under the light  $SU_1(2)$ . The symmetry breaking mechanism used in the NUGIM model utilizes a single scalar doublet. Despite this difference, the predictions of the two models are approximately similar, and for that reason the distinction between the two is not relevant for the current search.

For both models, a mixing parameter is defined between the two SU(2) groups, which here is called  $\theta_E$ , which is defined as  $\cot(\theta_E) = \frac{g_2}{g_1}$  [81]. For  $\cot\theta_E > 1$ , the couplings of W' to third generation fermions are enhanced. Values of  $\cot\theta_E > 5.5$  result in gauge boson interactions that cannot be perturbatively treated [43].

The region of  $\cot \theta_E < 1$  is ignored as it better probed by searches for light leptons. It is also useful to define the quantities  $s_E = \sin \theta_E$ ,  $c_E = \cos \theta_E$  and  $t_E = \tan \theta_E$ . The Family Model, also inherits the usual 2HDM parameter  $\tan \beta = t_\beta \equiv \frac{v_2}{v_1}$  representing the ratio of the vacuum expectation values of the two doublets. For  $t_\beta >> 1$  the model can explain the split of masses between the first two and the third generation. For that reason the  $t_\beta >> 1(s_\beta \approx 1, c_\beta \approx 0)$  is adopted for our cases.

For the W' and the NU model, the couplings to light and heavy fermions are:

$$g_{W'}^1 = \frac{g_W}{\sqrt{2}} t_E (1 + \epsilon^2 s_E^2 c_E^2),$$

and

$$g_{W'}^2 = \frac{g_W}{\sqrt{2}} \frac{1}{t_E} (1 - \epsilon^2 s_E^4)$$

where  $g_W$  is the weak coupling of the SM. For lower W' masses, the impact of the  $\epsilon^2$  terms becomes more important. At W' masses of 500 GeV, the  $\epsilon^2 \approx 0.026$  and once squared in the cross section, its impact becomes well-below the percent level and so it is neglected.

The total W' width is given by:

$$\Gamma_{W'} = 2\Gamma_{W' \to ev} + 1\Gamma_{W' \to \tau v} + 2N_c \Gamma_{W' \to ud'} + 1N_c \Gamma_{W' \to tb'} + \Gamma_{W' \to Wh}$$

where  $N_c = 3$  (the number of degrees of freedom of color) and the corresponding partial widths to

fermions are:

$$\begin{split} \Gamma_{W' \to e\nu} &= \frac{m_{W'} g_W^2}{48\pi} t^2 \\ \Gamma_{W' \to \tau\nu} &= \frac{m_{W'} g_W^2}{48\pi} \frac{1}{t^2} \\ \Gamma_{W' \to ud'} &= \frac{m_{W'} g_W^2}{48\pi} t^2 \left( 1 + \frac{\alpha_s}{\pi} \right) \\ \Gamma_{W' \to tb'} &= \frac{m_{W'} g_W^2}{48\pi} \frac{1}{t^2} \left( 1 + \frac{\alpha_s}{\pi} \right) \cdot C_t(B) \end{split}$$

where the  $\alpha_S$  is the strong coupling evaluated at  $m_W^2$ . Depending on model parameters, Wh can make a minor contribution to the total width. The W'Wh coupling is model dependent, with general form:

$$g_{W'Wh} = \frac{g_{WV}^2}{2} \frac{s^2 - s_{\beta}^2}{cs} = g_W M_W \frac{s^2 - s_{\beta}^2}{cs}$$

The partial width is given by:

$$\Gamma_{W' \to Wh} = \frac{m_{W'}}{192\pi} \frac{g_{W'Wh}}{M_W^2} C_{Wh}(m_W, mH)$$

where

$$C_{Wh}(M_W,M_h) = \sqrt{1 - \frac{2(M_W^2 + M_h^2)}{m_{W'}^2} + \frac{(M_W^2 - M_H^2)^2}{m_{W'}^4}} \\ \times \left(1 + \frac{(10M_W^2 - 2M_H^2)}{2m_{W'}^2} + \frac{(M_W^2 - M_H^2)^2}{m_{W'}^4}\right)$$

is a phase-space reduction factor.

The cases  $t_{\beta} \gg 0$  and  $t_{\beta} \to 0$  are interesting, as they correspond to a) the assumption made in the Family model and b) the NU model, respectively. These cases yield the following partial widths:

$$\begin{split} & \Gamma_{W'Wh}|_{t_{\beta} \to 0} = \frac{m_{W'}g_{W}^{2}}{192\pi}t^{2} \cdot C_{Wh}(m_{W}, mH) = \frac{1}{4}\Gamma_{W' \to e\nu} \cdot C_{Wh}(m_{W}, mH) \\ & \Gamma_{W'Wh}|_{t_{\beta} \gg 1} = \frac{m_{W'}g_{W}^{2}}{192\pi}\frac{1}{t^{2}} \cdot C_{Wh}(m_{W}, mH) = \frac{1}{4}\Gamma_{W' \to \tau\nu} \cdot C_{Wh}(m_{W}, mH) \end{split}$$

where it can be seen that the Wh width behaves like a partial fermion, either light or heavy, depending on the  $t_B$  choice.

The total W' decay width as a fraction of  $m_{W'}$  is shown in Fig. 15(a) as a function of  $m_{W'}$  for different values of  $\cot \theta_E$  assuming no Wh contribution (solid lines) and also assuming a Wh contribution with  $t_\beta \gg 1$  (dotted lines). The Wh contribution can reach up to  $\sim 7\%$  for high  $\cot \theta_E$  but it is neglected for simplicity and model reinterpretation. For the values of  $\cot \theta_E$  considered, the case  $t_\beta \to 0$  (NU models) yields negligible contribution from Wh. Fig. 15(b) shows the branching fractions as a function of  $\cot \theta_E$  for different hypotheses on the Wh contribution. Figure 16 shows the W' line

shapes, comparing cases with and without the Wh contribution, emphasizing the minor impact from Wh decays. The cross section times branching fraction with and without the Wh contribution is compared in Figure 17, showing differences of up to 7% for low mass and large  $\cot\theta_E$ , consistent with the branching fraction numbers. The impact on the acceptance for considering the Wh is up to 5%, and mainly due to the broadening of the W' width when the Wh channel decays are included.

It is important to emphasize that while the couplings of the W' to the third generation of fermions are enhanced, this does not lead to an increased cross section compared to the SSM at leading order. The reason for this is that the couplings at the production vertex of the W' scale with  $t_E$  (due to the light generation partons), whereas the decay to  $\tau \nu$  is be enhanced by  $1/t_E$ . Moreover, the proton's partonic structure does not contain top-quark partons (e.g. see Fig. 9), and the couplings of b-quarks to the lighter quarks are suppressed by the CKM matrix elements [82]  $^3$ . Although the enhanced couplings do not change the cross section, they will influence the width of the W'. Consequently, experimental results obtained under the assumption of the SSM may not hold or may require reinterpretation in different width scenarios, which makes the exploration of these scenarios particularly interesting.

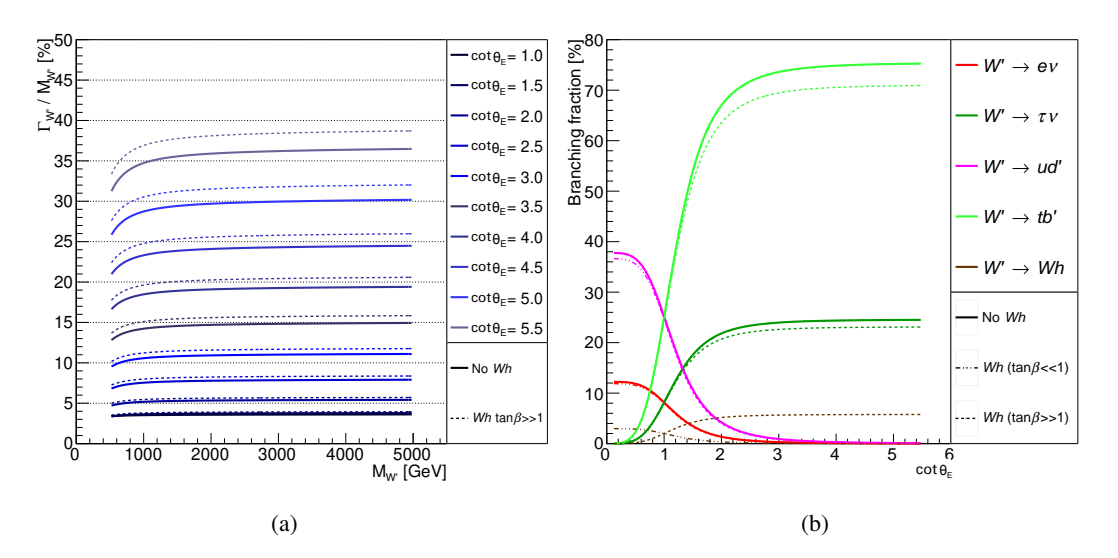


Figure 15: (a) The fractional W' decay width as a function of  $m_{W'}$  for different vaues of  $\cot \theta_E$  assuming no Wh contribution (solid lines) and also assuming a Wh contribution with  $t_{\beta} \gg 1$  (dotted lines). (b) The W' branching fractions as a function of  $\cot \theta_E$  for different hypotheses on the Wh contribution.

<sup>&</sup>lt;sup>3</sup> This is not the case for the Z', which can be produced by the  $b\bar{b}$  partons inside the proton.

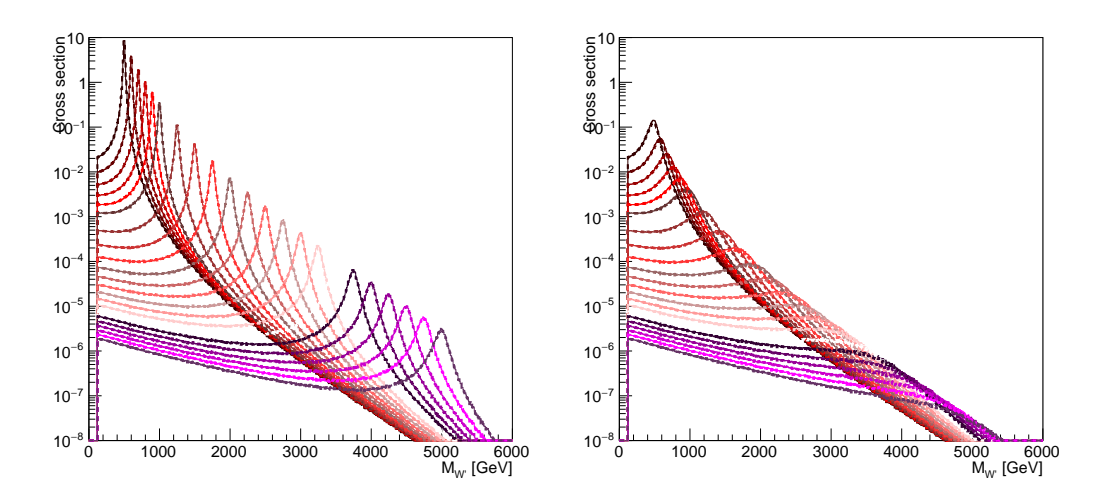


Figure 16: W' line shapes for (a)  $\cot \theta_E = 1$  and (b)  $\cot \theta_E = 5.5$  excluding Wh decays (thin solid line) and including Wh decays with  $t_\beta \gg 100$  (thick dotted lines). Note: it is almost impossible to differentiate the lines as they sit right on top of each other.

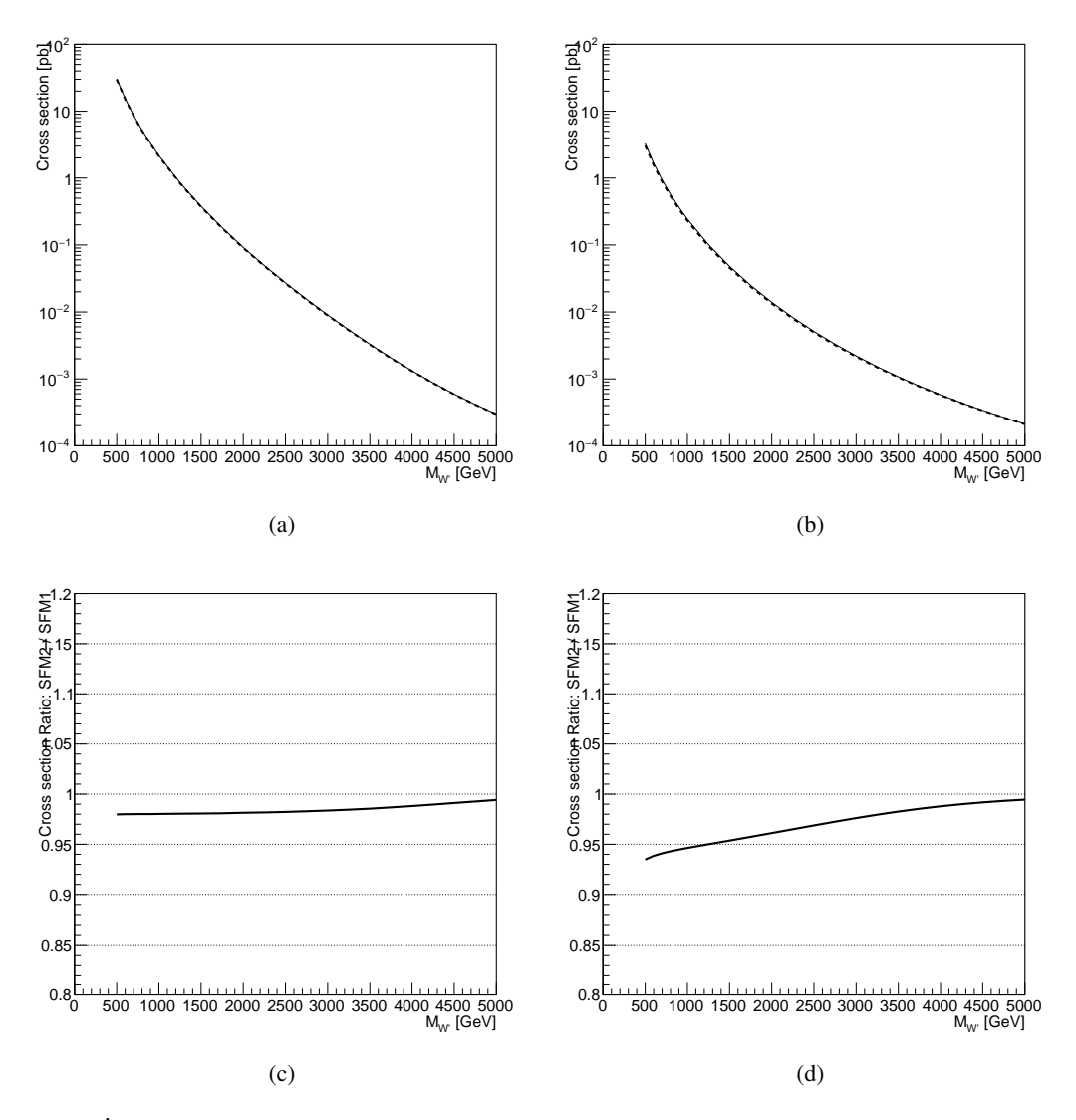


Figure 17: W' cross section times branching fraction as a function of  $m_{W'}$  for (a)  $\cot \theta_E = 1$  and (b)  $\cot \theta_E = 5.5$  excluding Wh decays (thin solid line) and including Wh decays with  $t_{\beta} \gg 100$  (thick dotted lines). The ratio with and without Wh is shown in (c) and (d), respectively.

# **Analysis**

# 5.1 Analysis Strategy

A search is presented for new resonances decay to final states with a tau lepton and a neutrino. The search is performed in the  $W' \to \tau \nu$  channel, where the  $\tau$  (tau)-lepton decays into hadrons ( $BR \sim 65\%$ ). The signature is a high- $p_{\rm T}$   $\tau_{\rm had-vis}$  and  $E_{\rm T}^{\rm miss}$  due to the undetected neutrino. The main discriminating variable is the transverse mass,

$$m_{\rm T} = \sqrt{2E_{\rm T}^{\rm miss}p_{\rm T}^{\tau_{\rm had-vis}} \left[1 - \cos\Delta\phi(\tau_{\rm had-vis}, E_{\rm T}^{\rm miss})\right]}$$
 (5.1)

where  $\Delta\phi(\tau_{\rm had\text{-}vis}, E_{\rm T}^{\rm miss}) \equiv \Delta\phi$  is absolute value of the azimuthal angle between the visible hadronic products of the tau decay and the  $E_{\rm T}^{\rm miss}$ . The transverse mass is particularly useful in cases where the full four-momentum of the daughter particles cannot be reconstructed, such as in the presence of neutrinos. In the case of hadronic decays of tau leptons in the  $W' \to \tau \nu$  search, the  $m_{\rm T}$  distribution has a unique shape. Below the mother particle's mass,  $m_{\rm T}$  decreases gradually; however, above the resonance mass, it falls off exponentially. This sharp drop-off helps distinguish the signal from background. The invariant and transverse mass distributions of a simulated W' signal with a mass of 2 TeV are shown in Fig. 18.

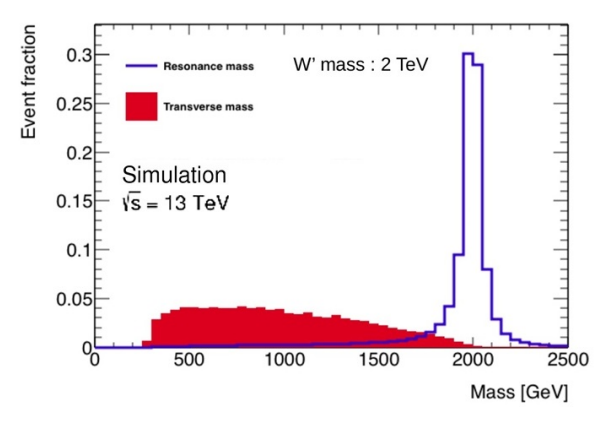


Figure 18: Overlay of the invariant mass (resonance mass) in blue and the transverse mass in filled red for a generated W' signal process, with mass of 2 TeV. Both distributions are normalized to unity.

The results are interpreted in the context of the benchmark Sequential Standard Model (SSM), for which the couplings of the W' to fermions are identical to those of the SM W. Interference effects between W/W' or decays into bosons are neglected.

A statistical analysis is finally performed (Sec. 6.2), where a shape fit of the transverse mass  $m_{\rm T}$  to data is performed. The parameter of interest is the signal cross section, proportional to the normalization of the signal contribution. A set of nuisance parameters (as estimated by the systematic uncertainties) control the variations of the background and signal yields. At the absence of signal in observed data, 95% CL upper limits on the considered signal models production cross section and decay to hadronically decaying taus are calculated using Frequentist inference with asymptotic formulas and the CLs approach. Upper limits on the visible cross section for generic models are also given after performing a cut and count search over the transverse mass range of 200 GeV to 2950 GeV. This approach allows the reinterpretation of this analysis results to different signal models that might differ in shape to the SSM or Non-Universal Models that are studied in this analysis.

## 5.2 Event selection

This search is performed on data collected by the ATLAS detector in pp-collisions during Run-2, which corresponds to integrated luminosity of 139 fb<sup>-1</sup>. Generic requirements are imposed on data, to ensure that the ATLAS detector parts and detectors operated optimally during the pp collisions, ensuring good quality data. This section describes the selection requirements used in this analysis.

First, the data are selected using the  $E_{\rm T}^{\rm miss}$  triggers, to take advantage of the large missing transverse momenta. Additional selection criteria are applied to obtain a signal-rich region and reduce background from other processes or detector inefficiencies. Events are required must contain at least one selected  $\tau_{\rm had-vis}$  candidate.

The signal region (SR) is defined by high  $E_{\rm T}^{\rm miss}$  to take advantage of the large mass of W' bosons, but to also provide high trigger efficiency (as seen in Fig. 30). The requirement is set to  $E_{\rm T}^{\rm miss} > 150\,{\rm GeV}$ . Since the W' bosons are produced nearly at rest in the transverse plane, the tau and neutrino from the W' decay, v[W'], are expected to be back-to-back with equal momenta. Due to the tau boost, the additional neutrino from the tau decay can partially cancel the  $E_{\rm T}^{\rm miss}$  of the v[W'], resulting in approximately balanced  $E_{\rm T}^{\rm miss}$  and  $\tau_{\rm had-vis}$ - $p_{\rm T}$ , as well as a back-to-back azimuthal topologies. The degree of  $E_{\rm T}^{\rm miss}$  cancellation depends on event kinematics, the final-state particles, and the initial W' mass. For a 2 TeV  $W'_{\rm SSM}$ , one expects around 50% cancellation between the neutrino momenta from the tau and W' decays. This is illustrated in Fig. 19 shows the ratio of the total transverse momentum of the neutrinos (i.e. the  $E_{\rm T}^{\rm miss}$  from the W' and  $\tau$ -lepton decays) to the transverse momentum of the v[W']. By requiring  $E_{\rm T}^{\rm miss}$  above 150 GeV, it was found that about 10% of the signal may be excluded at the truth level due to the additional tau neutrino in the final state, as illustrated in the  $p_{\rm T}$  distribution of v[W'] and  $p_{\rm T}^{\rm MET}$  in Fig. 20.

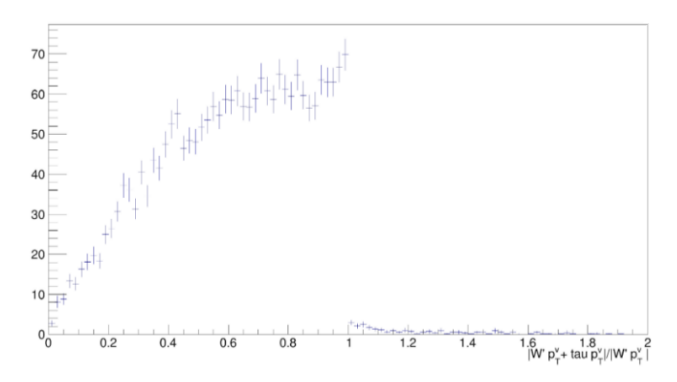


Figure 19: The ratio of the magnitude of the vectorial sum of the transverse momenta of the neutrinos from the tau lepton decays and the W' decay, over the transverse momentum magnitude of only the W' neutrino. This distribution corresponds to a SSM W' with mass of 2 TeV.

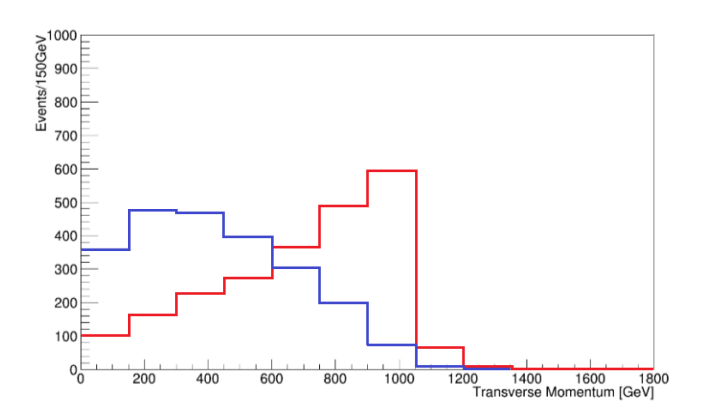


Figure 20: The transverse momentum distribution for the neutrino directly from a SSM W' with mass of 2 TeV (in red) and for the missing transverse energy ( $E_{\rm T}^{\rm miss}$ ), representing the sum of the vectorial transverse momenta of the two neutrinos from the W' decay chain,  $W' \to \tau \nu \to \tau_{\rm had\text{-}vis} \nu \nu$  (in blue).

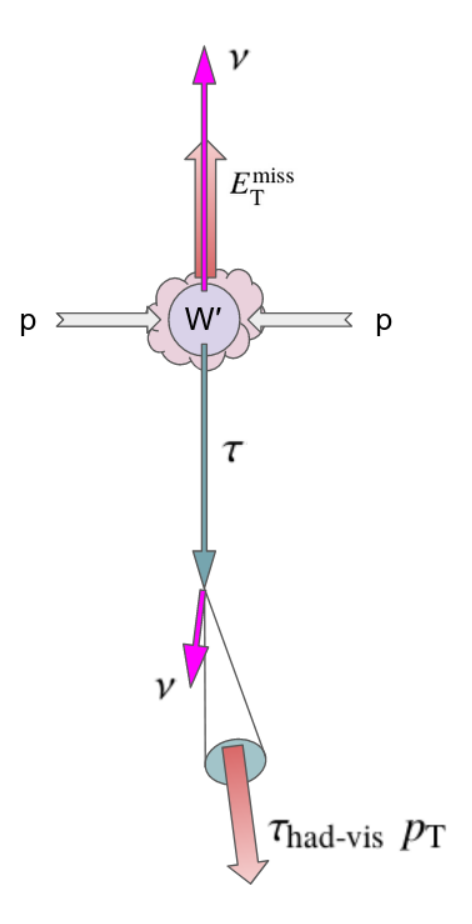


Figure 21: The topology aimed for the W' search.

These requirements are captured by selecting events with  $0.7 < \tau_{\text{had-vis}} - p_{\text{T}}/E_{\text{T}}^{\text{miss}} < 1.3$  and azimuthal separation  $\Delta \phi > 2.4$  rad. These selections were determined by scanning a variety of values and selecting the events that resulted in the optimal value of signal significance, defined as  $S/\sqrt{B}$ , where S(B) the number of signal (background) events in the SR. This topology is illustrated in Fig. 21, with the relevant distributions shown in Fig. 22.

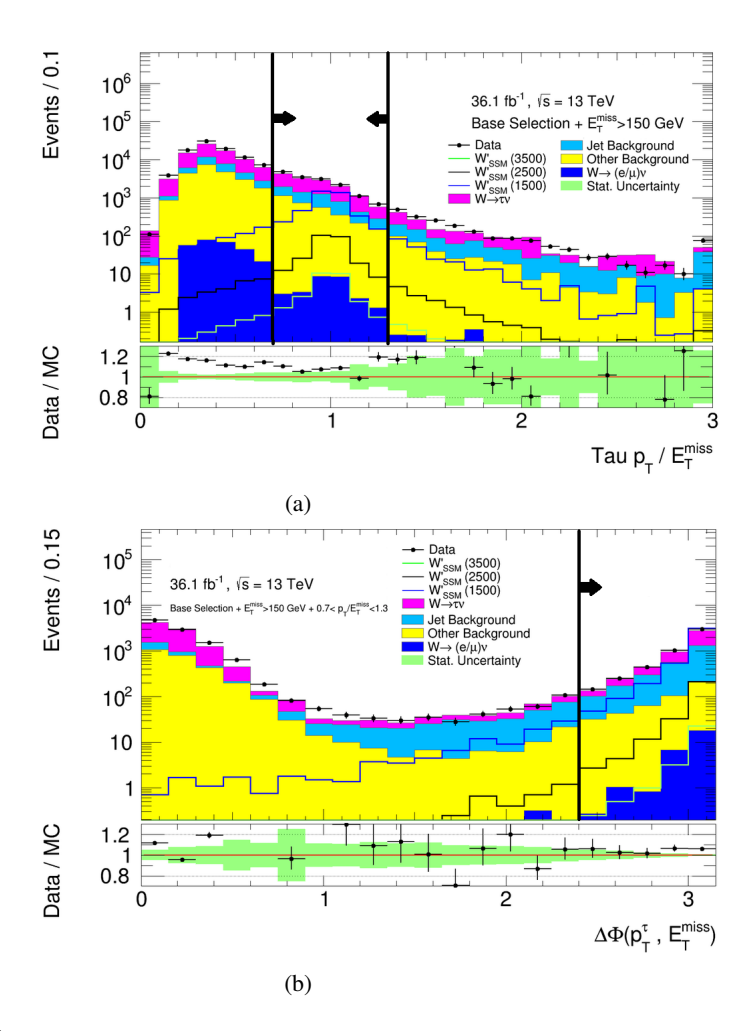
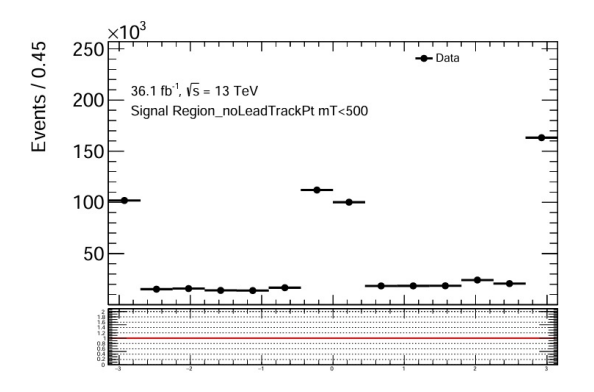


Figure 22: (a) the  $p_T/E_T^{\text{miss}}$  distribution of the background and three signal masses (1.5, 2.5 and 3.5 TeV) before cutting on  $p_T/E_T^{\text{miss}}$ . (b) the  $\Delta\phi$  distribution before the application of the cut on  $\Delta\phi$ . The black lines and arrows show the events falling in the definition of the SR.



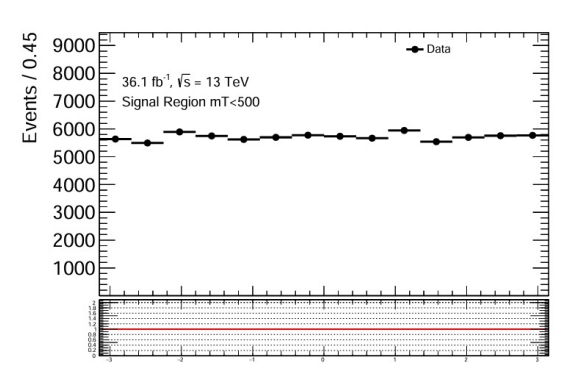


Figure 23: The  $\tau_{\text{had-vis}}$   $\phi$  distribution of the data in the Signal-like Region with  $m_{\text{T}} < 500$  GeV. The feature of the two spikes at  $\pm \pi$  and 0 (left plot) appears due to the NCB, and is removed by requiring the leading track of the  $\tau_{\text{had-vis}}$  to have transverse momentum above 10 GeV (right plot).

An analysis specific background originate from "Non-collisional backgrounds" (NCB). NCB stem from process that are not associated with the pp collisions inside the ATLAS detector. Such a background can, for example, be the beam-induced background, when an incoming proton interacts with gas inside the beam pipe and create a secondary shower of particles and muons. These muons can generally radiate energy in the calorimeter, sometimes creating a fake background that could be mistaken for a reconstructed jet or  $\tau_{\text{had-vis}}$  candidate if additional nearby tracks are present. This background typically appears as a spike at  $\tau_{\text{had-vis}}$   $|\phi| = 0$ ,  $\pi$  in back-to-back  $\tau_{\text{had-vis}}$  and  $E_{\text{T}}^{\text{miss}}$  topologies (see Fig. 23). The NCB is suppressed by requiring the leading track of the selected tau candidate to exceed 10 GeV. Additionally, as the production and W' decays are not expected to produce extra leptons, events containing a reconstructed loose electron or muon are rejected ("lepton veto"), which also reduces backgrounds with light leptons in the final state. The *Loose* quality criteria is used for tau-jet and tau-electron discrimination.

Events are further filtered by rejecting those in which the jet or tau closest to  $E_{\rm T}^{\rm miss}$  has an azimuthal separation from  $E_{\rm T}^{\rm miss}$  below 1.5 rad and overlaps with a known defective Tile Module. This helps eliminate events where the  $E_{\rm T}^{\rm miss}$  is mismeasured due to the presence of dead tile modules, which can cause spikes in the  $\phi(E_{\rm T}^{\rm miss})$  distribution, as shown in Fig. 24.

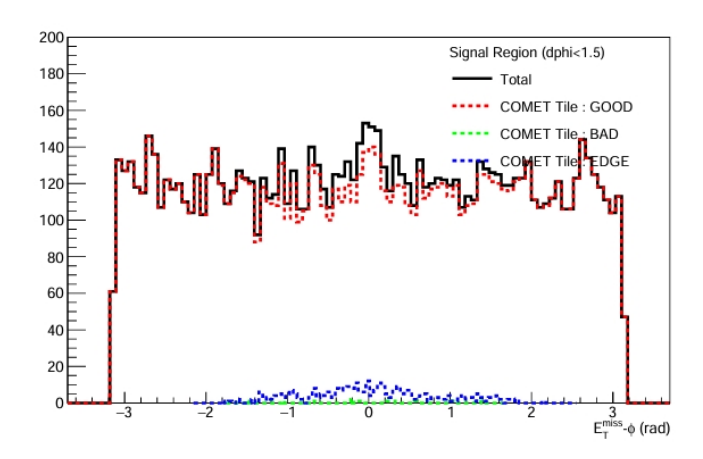


Figure 24: The  $E_{\rm T}^{\rm miss}$   $\phi$  distribution of the data collected in 2017 in the SR. The black line shows the total distribution. A small spike is observed at  $\phi\approx 0$ . The dashed red line shows the events where the closest object to the  $E_{\rm T}^{\rm miss}$  (COMET) is falling on an operational Tile Module. The cases where the COMET falls near the edges of and on a bad tile module are also shown in blue and green respectively. This indicates that the spike near  $\phi=0$  originates from mismeasured energies of the COMET.

Table 5.1: Summary of the event selection requirements. The top part of the table summarizes the "preselection" requirements that apply to all regions used in this analysis. The bottom part shows the additional selection requirements for each individual region. Here, the symbol L stands for *loose*  $\tau$ -lepton identification and VL\L denotes the requirement that the  $\tau$ -lepton candidate must satisfy the *very loose* but fail to satisfy the *loose* identification.

	Preselection	
E <sub>T</sub> <sup>miss</sup> trigger	70, 90, 110 GeV	
Event cleaning	applied	
$ au_{ m had-vis}$ tracks	1 or 3	
$ au_{ m had-vis}$ charge	±1	
$ au_{ m had ext{-}vis} ext{-}p_{ m T}$	> 30 GeV	
$ au_{ ext{had-vis}}  ext{$p_{ ext{T}}^{ ext{leadTrack}}}$	> 10 GeV	
Lepton veto	applied	
$\Delta\phi$	> 2.4 rad	

	Region requirements				
	SR	CR1	CR2	CR3	VR
au-lepton identification	L	$VL\L$	L	$VL\L$	L
$E_{ m T}^{ m miss}$	> 150 GeV	> 150 GeV	< 100 GeV	< 100 GeV	> 150 GeV
$ au_{ m had ext{-}vis} ext{-}p_{ m T}$ $/E_{ m T}^{ m miss}$	$\in [0.7, 1.3]$	$\in [0.7, 1.3]$	• • •	• • •	< 0.7
$m_{ m T}$	• • •				> 240 GeV

The event selection is summarized in Tab. 5.1. The definitions of additional regions used in this analysis are also provided. These regions were used for determining and validating the data driven backgrounds in the high- $m_{\rm T}$  region. In addition, the yields in data, the SM background processes and a SSM W' signal of mass 5 TeV are shown per selection defining the SR.

The acceptance times efficiency for various signal models is also shown in Fig. 25. The plot also demonstrates that for signal hypotheses with larger widths, the trigger selection's requirement of large- $E_{\rm T}^{\rm miss}$  negatively impacts the signal's acceptance.

Table 5.2: Overview of the selected numbers of events for data, the SM backgrounds and a  $W'_{SSM}$  signal of mass 5 TeV. The jet background is estimated from data and cannot be quantified before the requirements of  $E_{\rm T}^{\rm miss} > 150$  GeV and  $\tau$ -lepton identification. "Preselection" denotes all selection criteria described in Section 5 except for the  $\tau$ -lepton identification,  $E_{\rm T}^{\rm miss}$  and  $\tau_{\rm had-vis}$ - $p_{\rm T}$  / $E_{\rm T}^{\rm miss}$  requirements. The last row summarizes the number of observed and expected events above a large  $m_{\rm T}$  threshold, but is not part of the SR selection. The quoted uncertainties include both statistical and systematic sources of uncertainty.

Selection	Data	$W \to \tau \nu$	Jet background	Other background	$W'_{SSM}$ (5 TeV)
Preselection	3 640 749	$102000\pm6000$		$73000 \pm 6000$	18 ± 5
au-lepton identification	1 189 863	$84000 \pm 5000$	•••	$52000$ $\pm 4000$	17 ± 4
$E_{\rm T}^{\rm miss} > 150~{\rm GeV}$	58 528	$13400\pm1600$	$31000 \pm 9000$	$12000$ $\pm 1500$	15 ± 4
$0.7 < \frac{\tau_{\text{had-vis}} p_{\text{T}}}{E_{\text{T}}^{\text{miss}}} < 1.3$	18 528	$9700 \pm 1400$	$5800 \pm 400$	$2900\pm500$	14 ± 4
$m_{\rm T} > 1 {\rm TeV}$	58	$51 \pm 12$	$10 \pm 4$	$12.0 \pm 2.7$	$7.2 \pm 3.3$

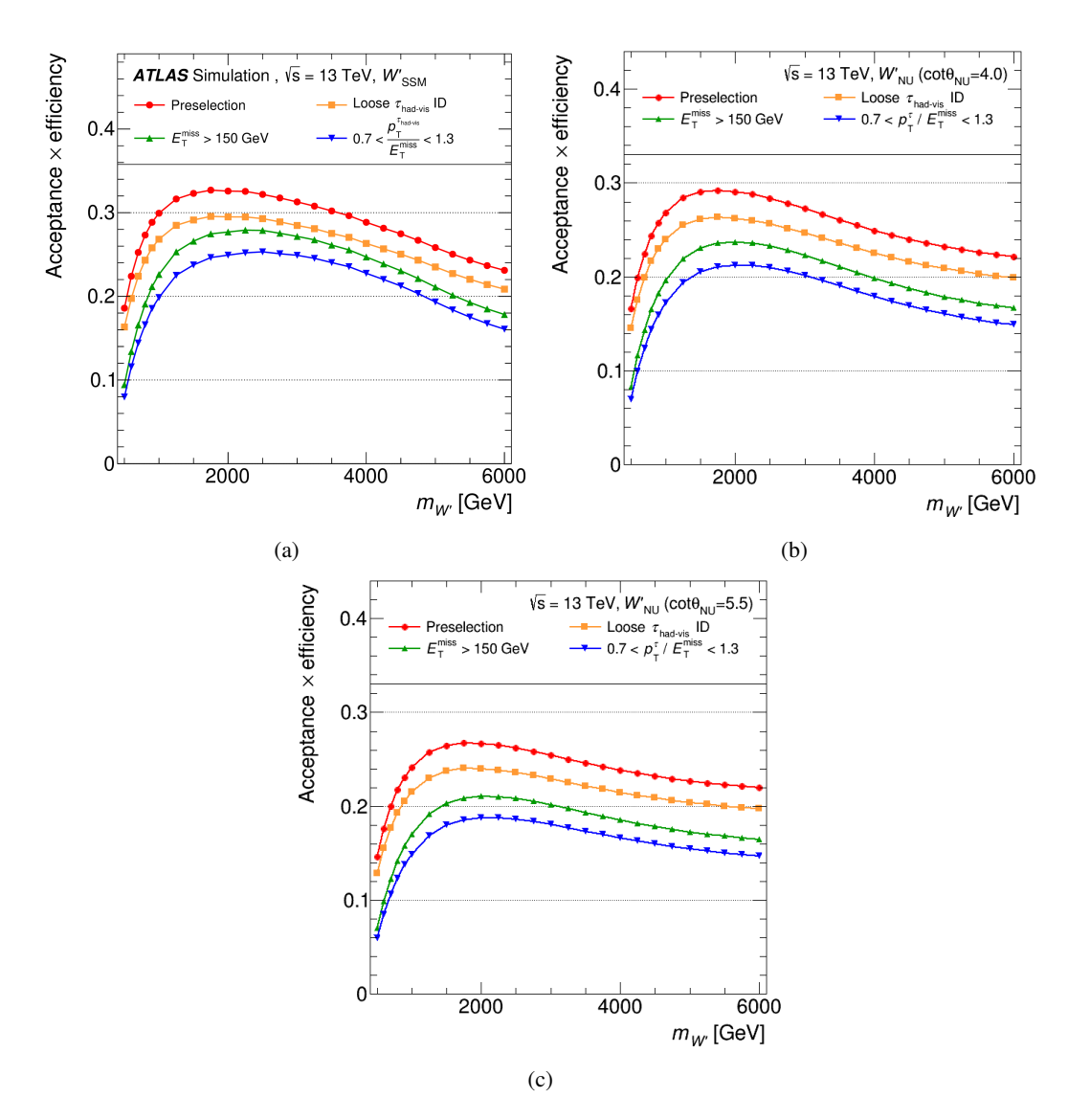


Figure 25: The acceptance times efficiency of a W' signal in (a) SSM model, (b)  $\cot \theta_E = 4$  NUGIM model, and (c)  $\cot \theta_E = 5.5$  NUGIM model, versus its mass after successively applying the reconstruction level selections.

# 5.3 Background Modeling

At high mass, the main background process is the offshell production and decay of W-bosons,  $W(\to \tau \nu)+jets$ , which is estimated using simulation data. Subleading backgrounds, also estimated through simulations, include other processes such as  $W(\to \ell \nu)+jets$ ,  $Z(\to \ell \ell)+jets$ ,  $Z(\to \tau \tau)+jets$ , as well as diboson decays (WW, ZZ, WZ),  $t\bar{t}$ , single-top production. Each of these backgrounds involves either a real tau, or a light lepton that is misidentified as a tau hadronic decay (lepton fakes).

Multijet production and processes where associated jets are misidentified as tau hadronic decays (such as  $Z(\to \nu\nu)+jets$ ) are estimated by using fake factors to reweight data in which the tau candidates did not meet the identification requirements. The fake factors are calculated in a multijet-rich control region, are binned in  $\tau_{\text{had-vis}}$ - $p_{\text{T}}$  and  $\tau_{\text{had-vis}}$  prongness ( $N_{\text{Trk}} \in 1, 3$ ). The jet estimate distribution, derived from the fake factor method described in Sec. 5.3.1, and shown in Fig. 26, is compared to simulations where the tau is matched to a generated jet. From this we determine that the jet background mainly consists of  $Z(\to \nu\nu)+jets$ , and  $W(\to \ell\nu)+jets$ ,  $W(\to \nu\nu)+jets$  where the additional jet mimics the  $\tau_{\text{had-vis}}$  decay.

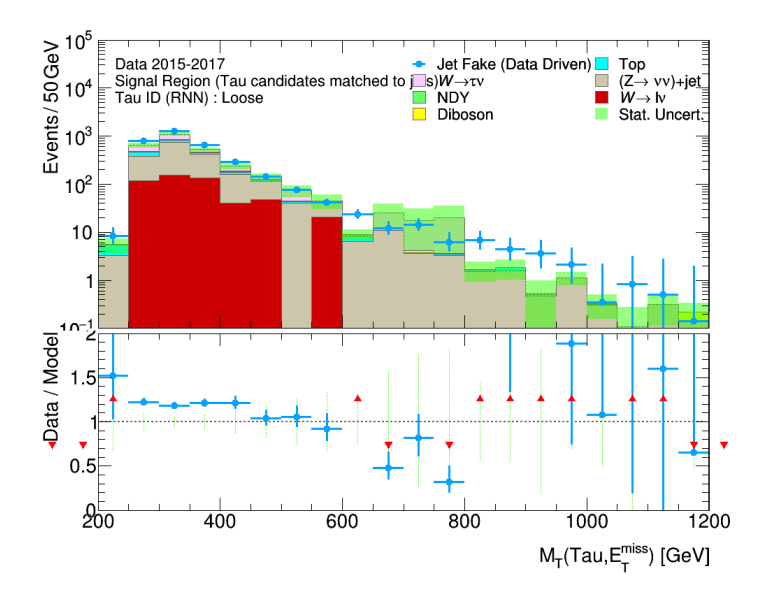


Figure 26: The  $m_{\rm T}$  distribution of jet background in the SR, as estimated by the fake factor method for the years 2015–2017, is shown as cyan data points and compared to simulated events where the  $\tau_{\rm had-vis}$  is matched to a jet.

#### 5.3.1 Fake Factor Method

The fake-factor method is a data-driven approach used to determine the  $\tau_{\text{had-vis}}$  background that originates from jet misidentification. The method relies on identifying two uncorrelated variables that can be used to differentiate the signal region, where the simulated background prediction is not reliable, from control regions that are enriched in the events of the background that one aims to determine. To achieve this goal, this analysis uses the tau identification and the event's missing transverse momentum.

To estimate the background from jets that are misidentified as the tau hadronic decays, three control regions are used. The events in the first control region (CR1) are required to pass the same selections used in the main analysis, but fail the tau identification requirement. In this analysis, the regions failing the identification requirement are defined such that the tau candidate will fail the *Loose* jet-RNN identification criteria but also pass the *Very Loose* requirement. The last requirement ensures that the control regions failing the identification are as close to the signal region as possible, i.e. with similar quark/gluon ratios, without losing statistical power due to the size of the region. The contamination of real leptons is measured from simulation and is about 12% (for both 1 and 3-prong) and is subtracted from data.

The other two control regions are used to measure fake factors and are designed to be rich in dijet events with minimal signal contamination. To achieve this, events in these regions are required to have  $E_{\rm T}^{\rm miss}$  below 100 GeV. Additionally, the requirement of balanced  $\tau_{\rm had-vis}$ - $p_{\rm T}/E_{\rm T}^{\rm miss}$  is removed, allowing the fake factor measurement at high  $p_{\rm T}$  even with low  $E_{\rm T}^{\rm miss}$  values. All other selections remain consistent with those in the main analysis. The control regions are differentiated by events that pass (CR2) or fail (CR3) the  $\tau$  identification. To get an estimate of jets present in data, the real lepton contamination is estimated from simulation and is subtracted. For 1-prong (3-prong)  $\tau$  candidates, the contamination of real leptons is about 7% (11%) in CR2 and 1% (1%) in CR3. Real lepton contamination in all regions related to the fake factor method are summarized in Tab. 5.3.

	Calculation	Region			Application	Region
	CR3		CR2		CR1	
$E_{\rm T}^{\rm miss}$ window [GeV]	1-prong	3-prong	1-prong	3-prong	1-prong	3-prong
[0, 100] (Nominal)	1	1	7	11	13	11
[30, 100]	1	1	8	12	13	11
[50, 100]	1	1	9	14	13	11
[70, 100]	2	2	11	17	13	11
[0, 150]	1	1	9	16	13	11

Table 5.3: The real lepton contamination [%] in data, split in  $\tau_{\text{had-vis}}$  prongness, for each of the different regions used to derive the fake factors (CR1, CR2, CR3). The contamination in the alternative definition of low- $E_{\text{T}}^{\text{miss}}$  regions of used for addressing systematic uncertainties of the method (see Sec. 5.6.2), are also shown.

The W' signal contamination in data across all control regions is estimated from simulation, normalized to the upper cross-section limits from previous searches. For signal hypotheses with masses above 1 TeV, the contamination in all control regions is negligible ( $\frac{1}{1}\%$ ).

The background estimation method then relies on measuring and applying the fake factors  $F_{ij}$  as

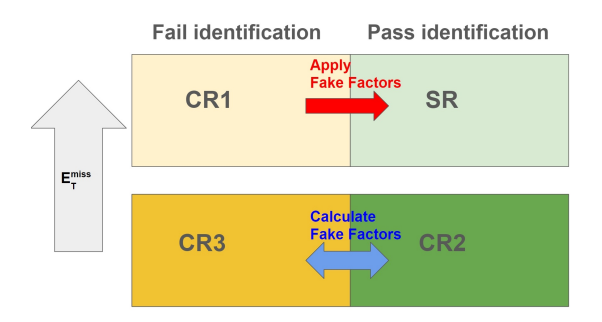


Figure 27: A schematic of the fake factor method.

defined in Eq. 5.2 and illustrated in Fig. 27. They are measured in intervals of the  $tauhadvis-p_T$  (denoted by index i), and separately for 1-prong and 3-prong  $\tau$ -lepton candidates (denoted by index j). This binning allows to capture the dependencies of the fake factors on the various reconstructed variables of the  $\tau_{had-vis}$  objects, while sustaining enough statistics in the control regions. Further dependencies on other observables, such as the  $\tau_{had-vis}$   $\eta$  or the event's trigger or year, is found to give negligible effects (less than 2%) and is not considered for simplicity.

The number of jet background events in the signal region,  $N_{SR}^{\text{jet}}$ , is computed from the number of data events in CR1 using the Fake factors:

$$N_{\rm SR}^{\rm jet} = \sum_{i,j} (N_{{\rm CR1},ij}^{\rm data} - N_{{\rm CR1},ij}^{\rm non-jet}) F_{ij} \text{, where } F_{ij} = \frac{N_{{\rm CR2},ij}^{\rm data} - N_{{\rm CR2},ij}^{\rm non-jet}}{N_{{\rm CR3},ij}^{\rm data} - N_{{\rm CR3},ij}^{\rm non-jet}},$$
 (5.2)

and where  $N_{X,ij}^{\text{data}}$  ( $N_{X,ij}^{\text{non-jet}}$ ) corresponds to the number of data (simulated) events populating the i-th and j-th intervals of  $\tau_{\text{had-vis}}$ - $p_{\text{T}}$  and number of prongs, respectively, in the region  $X \in \{\text{CR1}, \text{CR2}, \text{CR3}\}$ . They are measured in the  $\tau_{\text{had-vis}}$ - $p_{\text{T}}$  range of 100–500 GeV. The fake factors measured in the  $\tau_{\text{had-vis}}$ - $p_{\text{T}}$  interval of 350–500 GeV are also used for reweighting events with  $\tau_{\text{had-vis}}$ - $p_{\text{T}}$  above 500 GeV. The calculated fake factors as a function of the  $\tau_{\text{had-vis}}$ - $p_{\text{T}}$  for the 1 and 3-prong tau decays are shown in Figure 28.

### 5.3.2 High- $m_{\rm T}$ extrapolation and smoothening

One issue of the fake factor approach is the low statistics of data in the high- $m_{\rm T}$  tails, where the signal events are expected. To account for this, the jet background estimate for  $m_{\rm T}$  above 500 GeV is smoothened and extrapolated using fitted functions. Two choices of functions, given in Eq. 5.3, were considered, which described well the fitted jet background. Similar functional form choices have been previously used by other W'/Z' analyses in ATLAS [83, 84]. For this analysis, both these functions were tested over multiple ranges, with the lowest fitting range spanning 250 to 450 GeV in increments of 50 GeV, and the highest spanning 600 to 2100 GeV in similar steps. The parameters for both functions were determined through a binned-likelihood minimization fit, which is better suited to the low-statistics regions of higher mass bins. The quality of the fit was assessed via  $\chi^2/\text{NDF}$  and was used to determine optimal ranges. The set that gives the optimal value is given in Tab. 5.4.

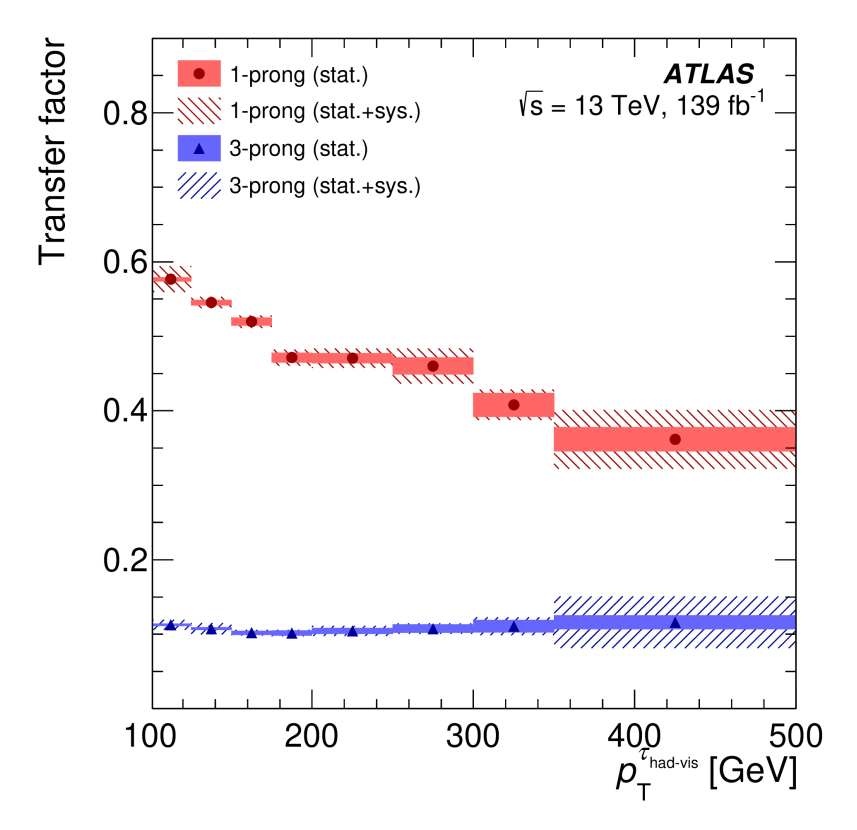


Figure 28: The fake factors used for the jet-background estimation as a function of  $\tau_{\text{had-vis}}$ - $p_{\text{T}}$ , for 1-prong (circles) and 3-prong (upward triangles)  $\tau$ -lepton decays. The uncertainty due to the limited number of events in CR2 and CR3 is shown in solid filled areas. The hatched areas indicate the total statistical and systematic uncertainties.

$$\begin{split} f(m_{\mathrm{T}}) &= N m_{\mathrm{T}}^{A+B \log m_{\mathrm{T}}} \quad logarithmic \ power \ function, \\ f(m_{\mathrm{T}}) &= A m_{\mathrm{T}}^{B} \quad power \ function, \end{split} \tag{5.3}$$

Function Type	m <sub>T</sub> Range [GeV]	$\chi^2/\text{NDF}$
Logarithmic Power Function	[400, 1900]	1.02
Power Function	[450, 1200]	0.98

Table 5.4: The fit function choices with their respective ranges and fit quality.

From the above fits, the *power function* and the range of [450,1200] GeV was chosen to model the jet distribution, as it scores a  $\chi^2/\text{NDF}$  value close to unity and gives a better agreement with the data-derived estimate tail integrals (as seen in Table 5.5). The *logarithmic power function* is used for as a systematic variation originating from the arbitrary choice of function.

For the sake of simplicity, these functions are not convoluted with additional kinematic suppression that may arise due to the kinematics of the interacting partons in the proton, the available beam

$m_{\mathrm{T}}^{\mathrm{thresh}}$	Estimate	Logarithmic	Power	$m_{\mathrm{T}}^{\mathrm{thresh}}$	Estimate	Logarithmic	Power
200	5770 ± 60	5800 <sup>+50.0</sup> -50.0	5780 <sup>+50.0</sup> <sub>-50.0</sub>	1600	1.2 ± 0.6	$0.196^{+0.035}_{-0.035}$	0.91 <sup>+0.2</sup> <sub>-0.16</sub>
250	$5760 \pm 60$	$5780^{+50.0}_{-60.0}$	$5760^{+50.0}_{-60.0}$	1650	$1.2 \pm 0.6$	$0.154^{+0.029}_{-0.029}$	$0.78^{+0.17}_{-0.14}$
300	4430 ± 50	$4450^{+50.0}_{-40.0}$	$4430^{+50.0}_{-50.0}$	1700	$1.2 \pm 0.6$	$0.122^{+0.024}_{-0.021}$	$0.67^{+0.15}_{-0.13}$
350	2187 ± 33	$2208^{+32.0}_{-33.0}$	$2193^{+32.0}_{-32.0}$	1750	$1.1 \pm 0.6$	$0.098^{+0.02}_{-0.018}$	$0.57^{+0.14}_{-0.11}$
400	1100 ± 23	$1121^{+22.0}_{-25.0}$	$1107^{+22.0}_{-24.0}$	1800	$0.7 \pm 0.5$	$0.078^{+0.016}_{-0.015}$	$0.50^{+0.12}_{-0.1}$
450	$587 \pm 17$	$608^{+17.0}_{-18.0}$	$594^{+18.0}_{-16.0}$	1850	$0.7 \pm 0.5$	$0.063^{+0.013}_{-0.012}$	$0.43^{+0.11}_{-0.09}$
500	$336 \pm 13$	$357^{+10.0}_{-12.0}$	$343^{+10.0}_{-12.0}$	1900	$0.7 \pm 0.5$	$0.051^{+0.011}_{-0.01}$	$0.38^{+0.1}_{-0.07}$
550	$212 \pm 10$	$214^{+8.0}_{-10.0}$	$211^{+8.0}_{-9.0}$	1950	$0.4 \pm 0.4$	$0.041^{+0.009}_{-0.008}$	$0.33^{+0.09}_{-0.07}$
600	136 ± 8	$132^{+6.0}_{-7.0}$	$135^{+7.0}_{-7.0}$	2000	$0.4 \pm 0.4$	$0.034^{+0.007}_{-0.007}$	$0.29^{+0.07}_{-0.06}$
650	92 ± 6	$84^{+5.0}_{-5.0}$	$90^{+5.0}_{-6.0}$	2050	$0.4 \pm 0.4$	$0.027^{+0.006}_{-0.005}$	$0.26^{+0.07}_{-0.05}$
700	65 ± 5	$54.2^{+4.0}_{-3.5}$	$62^{+5.0}_{-4.0}$	2100	$0.0 \pm 0.0$	$0.023^{+0.005}_{-0.005}$	$0.23^{+0.06}_{-0.05}$
750	46 ± 4	$35.8^{+2.5}_{-2.9}$	$43.3^{+4.0}_{-3.5}$	2150	$0.0 \pm 0.0$	$0.019^{+0.004}_{-0.004}$	$0.20^{+0.05}_{-0.04}$
800	$36 \pm 4$	$24.1^{+2.0}_{-2.0}$	$31.2^{+3.1}_{-2.7}$	2200	$0.0 \pm 0.0$	$0.0153^{+0.004}_{-0.0033}$	$0.18^{+0.05}_{-0.04}$
850	$24.4 \pm 3.2$	$16.4^{+1.4}_{-1.6}$	$22.9_{-2.2}^{+2.5}$	2250	$0.0 \pm 0.0$	$0.0127^{+0.0032}_{-0.0028}$	$0.159^{+0.05}_{-0.035}$
900	$17.4 \pm 2.6$	$11.4^{+1.1}_{-1.2}$	$17.1^{+2.1}_{-1.8}$	2300	$0.0 \pm 0.0$	$0.0106^{+0.0027}_{-0.0024}$	$0.143^{+0.04}_{-0.032}$
950	12.1 ± 2.2	$8.0^{+0.8}_{-0.8}$	$13.0^{+1.7}_{-1.4}$	2350	$0.0 \pm 0.0$	$0.0088^{+0.0023}_{-0.002}$	$0.128^{+0.04}_{-0.029}$
1000	9.1 ± 1.9	$5.7^{+0.6}_{-0.6}$	$10.0^{+1.3}_{-1.2}$	2400	$0.0 \pm 0.0$	$0.0074^{+0.0019}_{-0.0017}$	$0.115^{+0.034}_{-0.027}$
1050	$8.3 \pm 1.8$	$4.1^{+0.5}_{-0.5}$	$7.8^{+1.1}_{-1.0}$	2450	$0.0 \pm 0.0$	$0.0062^{+0.0016}_{-0.0014}$	$0.103^{+0.031}_{-0.024}$
1100	$6.7 \pm 1.7$	$3.0^{+0.4}_{-0.4}$	$6.1^{+0.9}_{-0.8}$	2500	$0.0 \pm 0.0$	$0.0052^{+0.0014}_{-0.0012}$	$0.093^{+0.029}_{-0.022}$
1150	$5.8 \pm 1.5$	$2.19^{+0.27}_{-0.3}$	$4.9^{+0.8}_{-0.7}$	2550	$0.0 \pm 0.0$	$0.0044^{+0.0012}_{-0.0011}$	$0.084^{+0.025}_{-0.021}$
1200	$4.5 \pm 1.3$	$1.63^{+0.23}_{-0.22}$	$3.9^{+0.7}_{-0.5}$	2600	$0.0 \pm 0.0$	$0.0037^{+0.001}_{-0.0009}$	$0.076^{+0.024}_{-0.018}$
1250	$3.8 \pm 1.2$	$1.22^{+0.18}_{-0.17}$	$3.2^{+0.5}_{-0.5}$	2650	$0.0 \pm 0.0$	$0.0031^{+0.0009}_{-0.0008}$	$0.069^{+0.021}_{-0.017}$
1300	$2.7 \pm 1.0$	$0.92^{+0.13}_{-0.14}$	$2.6^{+0.5}_{-0.4}$	2700	$0.0 \pm 0.0$	$0.0027^{+0.0007}_{-0.0007}$	$0.063^{+0.021}_{-0.015}$
1350	$2.5 \pm 1.0$	$0.70^{+0.11}_{-0.11}$	$2.16^{+0.4}_{-0.35}$	2750	$0.0 \pm 0.0$	$0.0023^{+0.0007}_{-0.0006}$	$0.057^{+0.019}_{-0.014}$
1400	$1.9 \pm 0.8$	$0.53^{+0.09}_{-0.08}$	$1.79^{+0.34}_{-0.3}$	2800	$0.0 \pm 0.0$	$0.0019^{+0.0006}_{-0.0005}$	$0.052^{+0.018}_{-0.013}$
1450	$1.9 \pm 0.8$	$0.41^{+0.07}_{-0.06}$	$1.50^{+0.3}_{-0.26}$	2850	$0.0 \pm 0.0$	$0.0017^{+0.0005}_{-0.0004}$	$0.048^{+0.016}_{-0.012}$
1500	$1.9 \pm 0.8$	$0.32^{+0.06}_{-0.05}$	$1.26^{+0.26}_{-0.22}$	2900	$0.0 \pm 0.0$	$0.0014^{+0.0004}_{-0.0004}$	$0.044^{+0.014}_{-0.011}$
1550	$1.2 \pm 0.6$	$0.25^{+0.05}_{-0.04}$	$1.07^{+0.23}_{-0.18}$	2950	$0.0 \pm 0.0$	$0.00121^{+0.0004}_{-0.00032}$	$0.040^{+0.014}_{-0.01}$

Table 5.5: The total number of expected jet events in 2015-2018 data in the SR above each cut on the transverse mass,  $m_{\rm T}^{\rm thresh}$ , taken from the fake factor method without extrapolation (Estimate) and after using the *Logarithmic power function* (Logarithmic Power) and *power function* (Power) fitted in the range of [400, 1900] GeV and [450, 1200] GeV respectively to estimate the fakes above  $m_{\rm T}$  of 500 GeV. The comparison between the *Power* or *Logarithmic Power* yields and the Estimate shows that the *Logarithmic Power* function tends to underestimate the number of expected events at the high masses. The errors correspond to the statistical uncertainty.

energy, etc. Such effects would only affect the highest  $m_{\rm T}$  bin of our search. To check the impact of this assumption on this analysis, the overall jet background impact at the highest  $m_{\rm T}$  threshold of this analysis is accessed (of 2.95 TeV in the model-independent limits). In the total background of 0.108 events, the expected jet background in that bin is  $N_{\rm fake} = 0.0391$ , amounting to 36%. The  $N_{\rm fake}$  was scaled by 0.01 in that bin, to reflect the fact that in the main analysis we are overestimating the fakes. The choice of this particular scaling is motivated by comparisons between the fitted functions and simulated fake background samples in the high- $m_{\rm T}$  region, in which one can see that for  $m_{\rm T}$  above 2 TeV the fitted function is overestimating the dominant backgrounds by at least a factor of 100 (Fig. 29). This resulted in a change to the upper limit of the model-independent visible cross section (Sec. 6.3) by less than 3%.

- 95% CL upper limits observed (expected) with  $N_{\text{fake}} = 0.039100 : 3.2107501 (3.3686201)$
- 95% CL upper limits observed (expected) with  $N_{\text{fake}} = 0.000391 : 3.1636941 (3.2853355)$

For lower  $m_{\rm T}$  thresholds, or for model-dependent limits that only use values up to  $m_{\rm T} \leq 2$  TeV, the results are less sensitive to the small contribution from  $N_{\rm fake}$  above 3 TeV. This is because the background at these high  $m_{\rm T}$  values is minimal and has little effect on the search's upper limits.

Since the last point of the fake background estimate was observed at 2.25 TeV, we conducted the same check as above by rescaling  $N_{\rm fake}$  for  $m_{\rm T} > 2.25$  TeV by 0.01. This adjustment resulted in only a 4% change in the upper limits. These small variations from overestimating the jet background, along with limited MC statistics to further verify background estimates in the extrapolated regions, led this analysis to adopt the more conservative upper limits.

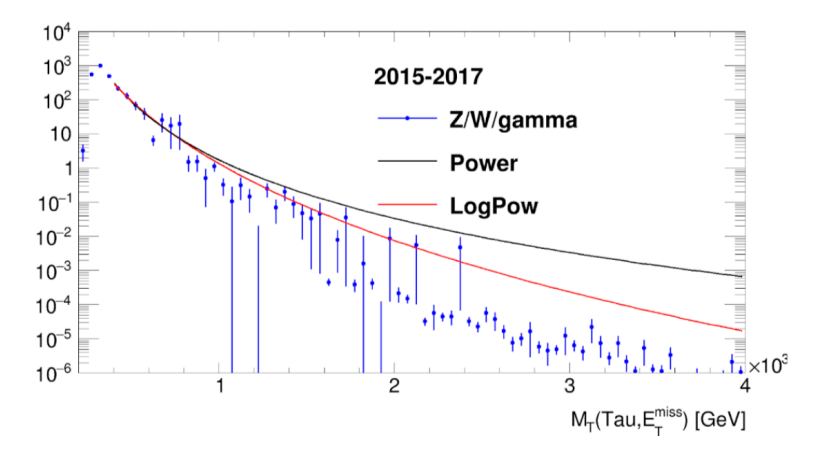


Figure 29: The  $m_{\rm T}$  distributions for the jet background fit functions (black and red) for the years 2015-2017 are compared to the simulated  $W/Z/\gamma^*$ +jets distribution of fake taus (blue). For  $m_{\rm T} > 2$  TeV, one can see that that the jet background could be underestimated by a factor of 100.

### 5.4 HLT corrections

The  $E_{\rm T}^{\rm miss}$ -trigger response is highly sensitive to the reconstructed objects and event topology in both the L1 and HLT stages. Consequently, ATLAS does not provide centralized data/MC calibration factors. Instead, each analysis has to derive specific trigger scale factors relevant for its topologies. This section details the methodology and results of these trigger scale factor measurements.

To measure  $E_{\rm T}^{\rm miss}$ -trigger efficiencies, we used a topology resembling the signal region as closely as possible. The  $E_{\rm T}^{\rm miss}$  calculation at trigger level solely relies on information from the calorimeter systems, where muons deposit minimal energy. As such, they can be treated as "invisible" particles in the trigger decision. Therefore, trigger efficiencies were measured in both data and simulation using a boosted  $Z(\to \mu\mu)+jets$  topology. By requiring that the tau-jet object recoils against the Z boson, we can select events where tau candidates appear with significant missing transverse momentum in the opposite azimuthal direction. For this measurement, muons were also treated as invisible in the offline  $E_{\rm T}^{\rm miss}$  calculation.

Events were selected using the single-muon triggers HLT\_mu26\_ivarmedium and HLT\_mu50, which ran unprescaled with the lowest thresholds during the Run-2<sup>1</sup>. The leading muon  $p_T$  was required to be above 30 GeV or 55 GeV, depending on the trigger, ensuring the muon trigger operated efficiently in data and simulation. The two leading muons had to pass loose quality requirements, have opposite charges and and originate from a Z boson decay with an invariant mass between 66.6 GeV and 116.6 GeV. Events with any reconstructed electron or poorly reconstructed muon were vetoed. Additionally, the azimuthal angle between the reconstructed  $E_T^{\text{miss}}$  (with muons as invisible) and the tau jet had to be over 2.4 rad, ensuring that the Z boson recoils from a tau-like jet.

Trigger efficiencies and calibration factors were also measured in  $W(\to \mu\nu)+jets$  and  $t\bar{t}$  events using the single-muon triggers. For both regions, the presence of exactly one reconstructed muon is required and the transverse mass between the muon and  $E_{\rm T}^{\rm miss}$  (calculated with the muon treated as visible) was required to exceed 50 GeV. Events rich in W processes were selected by vetoing the presence of b-jets, while  $t\bar{t}$  events required at least one b-jet to be present. Other selection requirements were consistent with the  $Z(\to \mu\mu)+jets$  selection. The maximum observed difference between calibration factors from  $Z(\to \mu\mu)+jets$  and  $W(\to \mu\nu)+jets$  or  $t\bar{t}$  events was treated as a systematic uncertainty. The  $t\bar{t}$  region, enriched in real taus, also provides insight into the impact of the tau energy scale, as most taus in the  $Z(\to \mu\mu)+jets$  and  $W(\to \mu\nu)+jets$  topologies are not matched to generated taus and do not get calibrated to the tau energy scale. The event requirements for each region are summarized in Tab. 5.6.

The  $E_{\rm T}^{\rm miss}$ -trigger efficiencies are determined in data and simulation, by looking at events passing the corresponding trigger in a given period in which the  $E_{\rm T}^{\rm miss}$ -triggers ran unprescaled. The periods are given in Tab. 5.7. In order to increase statistics, the  $E_{\rm T}^{\rm miss}$ -triggers do not have to be the lowest unprescaled ones in a given period.

The efficiencies are shown in Fig. 30. The measured efficiencies in data (simulation),  $\epsilon_{data(mc)}$ , were calculated using the ROOT's functionality of TGraphAsymErrors and follow a known distribution of a modified Beta-function: Beta(1+k, 1+n-k) where k, (n) the number of passing (total) events. Using this distribution, in total 100,000 random efficiencies were generated for data and simulation in each  $E_{\rm T}^{\rm miss}$ -bin and taking their ratio:  $\epsilon_{data}/\epsilon_{mc}$ , the distribution of the calibration factors was

<sup>&</sup>lt;sup>1</sup> The exception is in year 2015, where lower-threshold muon triggers were available, though higher thresholds were used for retaining simplicity.

Baseline	
Feature	Criterion
Trigger	Lowest-unprescaled single muon trigger
Muon $p_{\mathrm{T}}$	$p_{\rm T}^{\rm lead-\mu} > 30(55) {\rm GeV}$
Event Cleaning	EC_LooseBad + Detector cleaning + Dead Tile Module cleaning
BadJet Cleaning	TightBad
eVeto and BadMuon veto	$N_{\mu-\text{bad}} + N_{e-\text{loose}} = 0$
Tau Multiplicity	$N_{\tau} \ge 1$
Tau Charge	$ q  = 1$ if $(1  3)$ -tracks else $ q  \le 2$
Tau Identification	Very Loose
Back-to-Back topology	$\Delta \phi(\tau, E_{\rm T}^{\rm miss}) > 2.4$
Z Region	
Number of muons	$N_{\mu-\mathrm{loose}} = 2$
Oppositely charged muons	$q_{0-\mu}q_{1-\mu} < 0$
Invariant Mass window	$m_{\mu\mu} \in [66.6, 116.6] \text{ GeV}$
W Region	
Number of muons	$N_{\mu-\mathrm{loose}} = 1$
Transverse Mass requirement	$m_{\rm T}(\mu, E_{\rm T}^{\rm miss}) > 50{\rm GeV}$
B-veto	$N_{b ext{-jets}} = 0$
top Region	
Number of muons	$N_{\mu-\mathrm{loose}} = 1$
Transverse Mass requirement	$m_{\rm T}(\mu, E_{\rm T}^{\rm miss}) > 50{\rm GeV}$
B-tag	$N_{b ext{-jets}} > 0$

Table 5.6: The event selections for the trigger efficiency measurement regions.

Data	trigger	period
2015-2016	HLT_xe70_mht	[276262, 284484]
	HLT_xe90_mht_L1XE50	[282712, 302872] ∪
		{302925, 302956}∪
		[303264, 303892]
	HLT_xe110_mht_L1XE50	[302737, 311481]
2017	HLT_xe110_pufit_L1XE50	[331697, 340453]∪
		{331033, 329835, 329716 ,329778 ,327862, 328042}∪
		[330166, 330294]∪
		[325790, 327490]
	HLT_xe110_pufit_L1XE55	[325713, 340453]
2018	HLT_xe110_pufit_xe65_L1XE50	[350067, 364292]
	HLT_xe110_pufit_xe70_L1XE50	[348885, 364292]

Table 5.7: The periods in which each  $E_{\rm T}^{\rm miss}$ -trigger efficiency is measured in data and simulation.

determined. The calibration factors are then determined by the median of this distribution and their error as the range containing the  $\pm 34.1\%$  of entries.

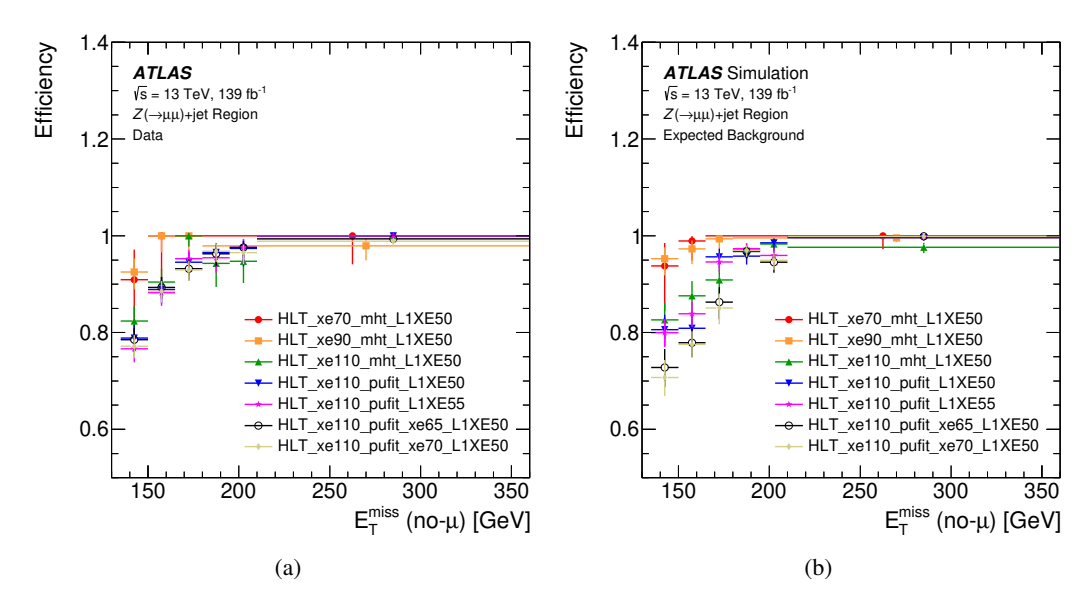


Figure 30: The trigger efficiencies in (a) data and (b) simulation as measured in  $Z(\to \mu\mu)+jets$  events relative to the offline  $E_T^{miss}$  without the muon contribution.

# 5.5 High- $p_T$ tau reconstruction corrections

This search examines  $\tau$ -leptons produced at high transverse momenta ( $p_{\rm T}$ ). It is essential to ensure consistent treatment between data and simulations to accurately model the high-mass regions. However, a challenge arises because hits from long-lived  $\tau$ -leptons in the inner detector are not simulated. This issue resulted in a drop of the  $\tau$ -reconstruction efficiency in simulation for high- $p_{\rm T}$ , boosted  $\tau$ 's decaying beyond the initial inner detector layers. In past analyses, a one-sided systematic uncertainty was introduced to account for reduced efficiency in 1-prong  $\tau$  leptons, assuming flat efficiency at high- $p_{\rm T}$ . Here, we adopted a different approach – applying truth corrections to align simulations with data expectations.

#### 5.5.1 Measurement of correction factors

The signal sample without  $\tau$  simulation ("Material Transport OFF") represents expectations from centrally produced Monte Carlo, while the one with simulated  $\tau$  hits ("Material Transport ON") reflects the expectations from data. Reconstruction efficiencies,  $\epsilon_{\rm data}$  and  $\epsilon_{\rm mc}$ , are calculated from these samples, and truth correction weights are derived as their ratio ( $\epsilon_{\rm data}/\epsilon_{\rm mc}$ ). Efficiency is measured as a function of the generated  $\tau$ - $p_{\rm T}$  for both 1- and 3-prong  $\tau$ -lepton decays and for barrel ( $|\eta| < 1.37$ ) and endcap ( $|\eta| > 1.52$ ) regions. They are calculated as the ratio of reconstructed to generated 1(3)-prong  $\tau$ -lepton decays, with baseline requirements of  $\tau$ -leptons having at least 20 GeV transverse momentum and be within pseudorapidities of  $|\eta| < 2.5$  (reconstructed and generated), and matched to an isolated  $\tau$  from a W' boson. These efficiencies and correction weights are displayed in Fig. 31.

In addition, a similar approach was used for W' signal sample that was made to go through the Full-Simulation of ATLAS. The impact of omitting long-lived particle simulation on reconstruction efficiency is expected to be similar between Full-Simulation and AF2. As shown in Fig. 32, both approaches yield similar reconstruction efficiencies. This justifies applying the corrections across both signal (AF2) and background (Full-Simulation) samples, as they are parameterized in generator-level quantities independent of simulation methods.

For high- $p_{\rm T}$  1-prong  $\tau$ -lepton decays, the reconstruction efficiency significantly degrades in centrally produced MC, as generated 1-prong  $\tau$ 's fail to provide enough hits and are misidentified as 0-prong. Simulating the inner detector  $\tau$  hits recovers many of these  $\tau$ -leptons by reconstructing tracks from the hits. However, for low- $p_{\rm T}$   $\tau$ -leptons, simulating hits slightly decreases the reconstruction efficiency due to a pronounced decay vertex kink, making track reconstruction difficult. These trends are illustrated in Fig. 34.

High- $p_{\rm T}$  3-prong  $\tau$  reconstruction suffers mainly from track merging, an effect when the tracks are so close together that the reconstruction algorithms cannot distinguish between them. This causes a large migration of 3-prong tau-leptons into tau-leptons with lower track multiplicities. While the 3-prong reconstruction efficiency declines, this has minimal impact on the overall analysis due to the low branching ratio of 3-prong decays. Including  $\tau$  hits in simulation can further degrade the 3-prong reconstruction efficiency, mainly due to the following reasons, also illustrated in Fig. 33:

- The  $\tau$  hits combining into a single-track particle, and so the  $\tau$  lepton is still reconstructed as 1-prong. This effect is clearly notable in cases where the  $\tau$  decays into three charged mesons after the inner detector.
- Track reconstruction failure for two of the three charged pions. Such a scenario can for example

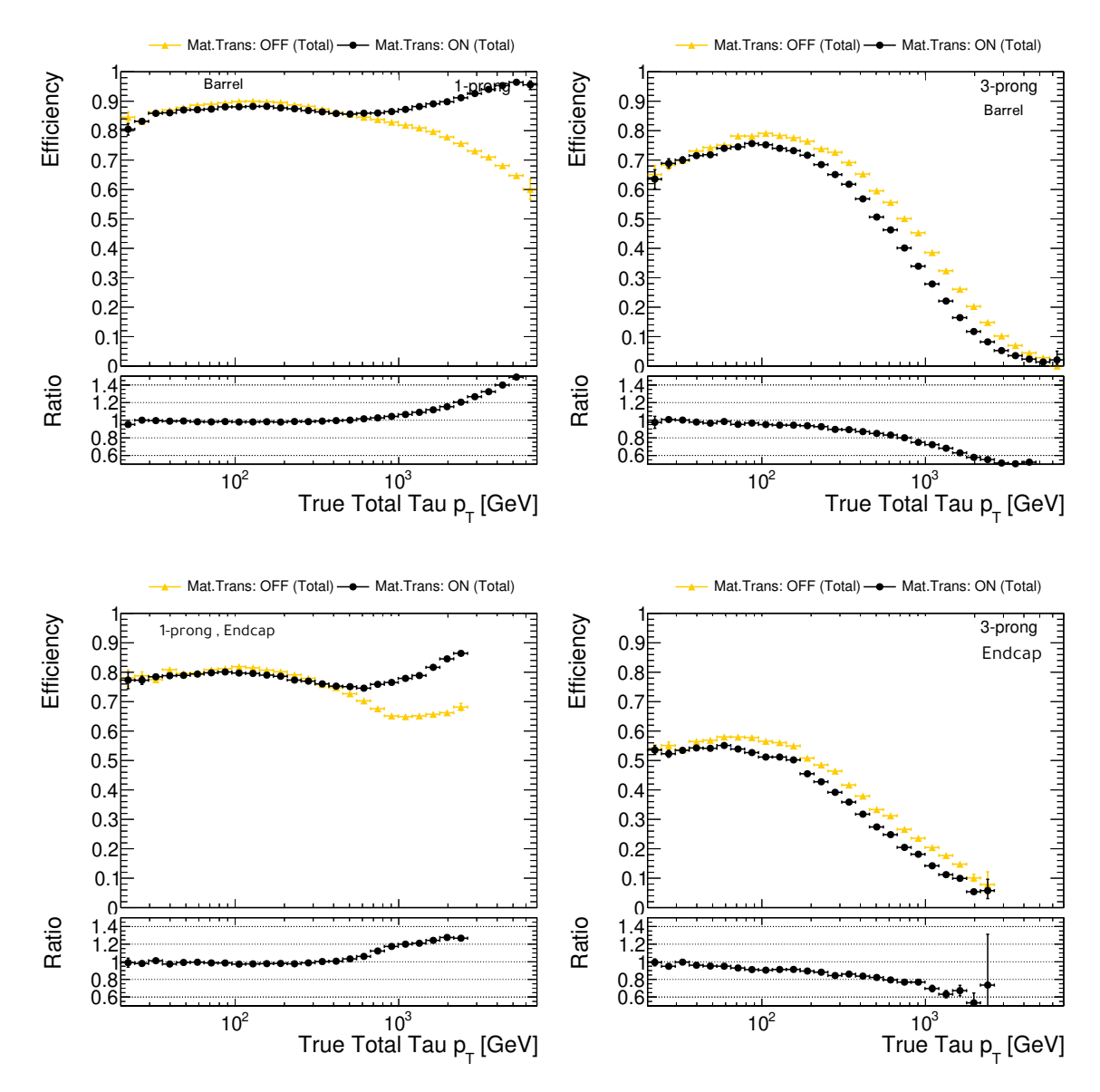


Figure 31: The  $\tau_{\rm had}$  reconstruction efficiencies and their ratios as a function of the generated  $\tau$ - $p_{\rm T}$  for 1-prong (left) and 3-prong (right) taus. The top plots show the reconstruction efficiencies in the Barrel region and the bottom plots in the Endcap region. The orange data points correspond to the centrally-produced MC expectations, in which tau hits are not simulated. The black data points correspond to the special MC simulations in which the tau hits are simulated (expected data). The ratio, defined as  $\epsilon_{\rm data}/\epsilon_{\rm mc}$ , is the truth correction weights used to reweight the truth-matched simulated taus in the analysis.

appear by a  $\tau$  that decays into three charged mesons, one layer before the leaving the inner detector.

The above efficiencies, once taking into account the various migrations to lower multiplicities, are shown in Fig. 35, where a range of reconstructed multiplicities is allowed in the numerator.

An additional consideration is that the tau identification algorithm was trained on samples without

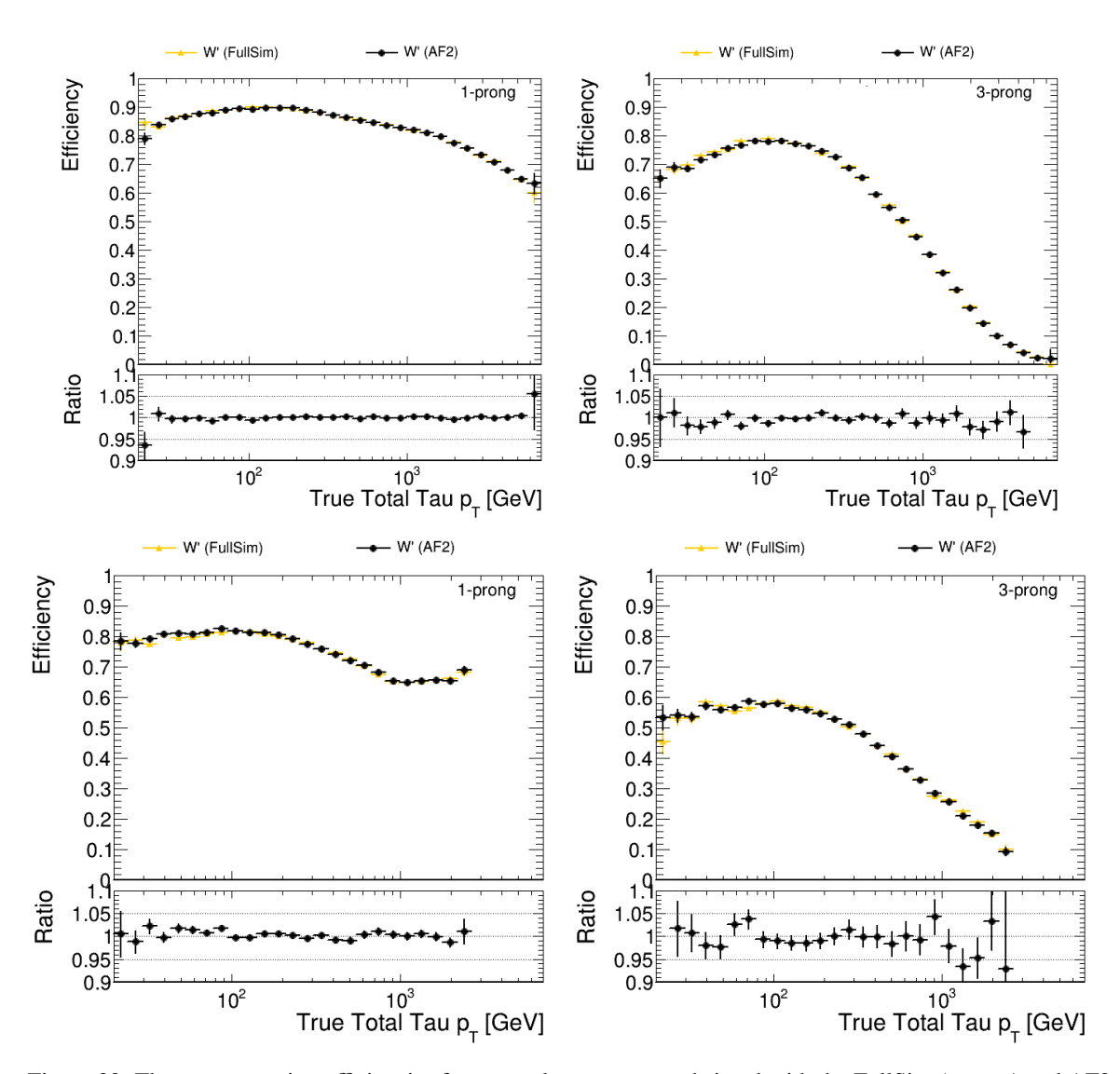


Figure 32: The reconstruction efficiencies for correctly reconstructed signal with the FullSim (orange) and AF2 (black) chains as a function of  $\tau$ -lepton's total  $p_T$ .

simulated long-lived particles. Due to reliance on  $\tau$  track information, we observe that with the tau identification requirement, efficiencies between samples with and without simulated  $\tau$  hits align better across a broader  $p_{\rm T}$  range (Fig. 36). This alignment suggests the identification algorithm learned to exclude non-simulated 0-prong  $\tau$ s, implying that more  $\tau$  candidates in real data with early detector decays would also be rejected. Thus, to avoid double counting this correction, the measured efficiency is further defined to include both reconstruction and the Loose RNN identification requirements.

The calibration factors later are applied as binned scale factors to truth-matched  $\tau_{\rm had}$  that fulfill the analysis selection criteria. A binned approach was chosen for simplicity to apply these factors on simulated events and the binning was done in truth quantities of the  $\tau$ - $p_{\rm T}$ ,  $\eta$  and decay mode. The binning is optimized to capture the  $p_{\rm T}$ -dependent trends in those factors.

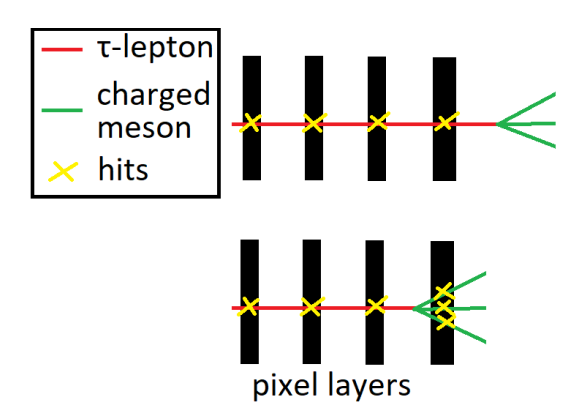


Figure 33: Schematic of the origins of 3-prong  $\tau_{\text{had-vis}}$  reconstruction inefficiency. On top the tau hits would provide a tau candidate of 1-prong. On the bottom, even though the tau can decay inside the inner detector, it may be the case that the additional hits of the charged mesons do not result in a track, resulting in tau candidate with lower track multiplicity.

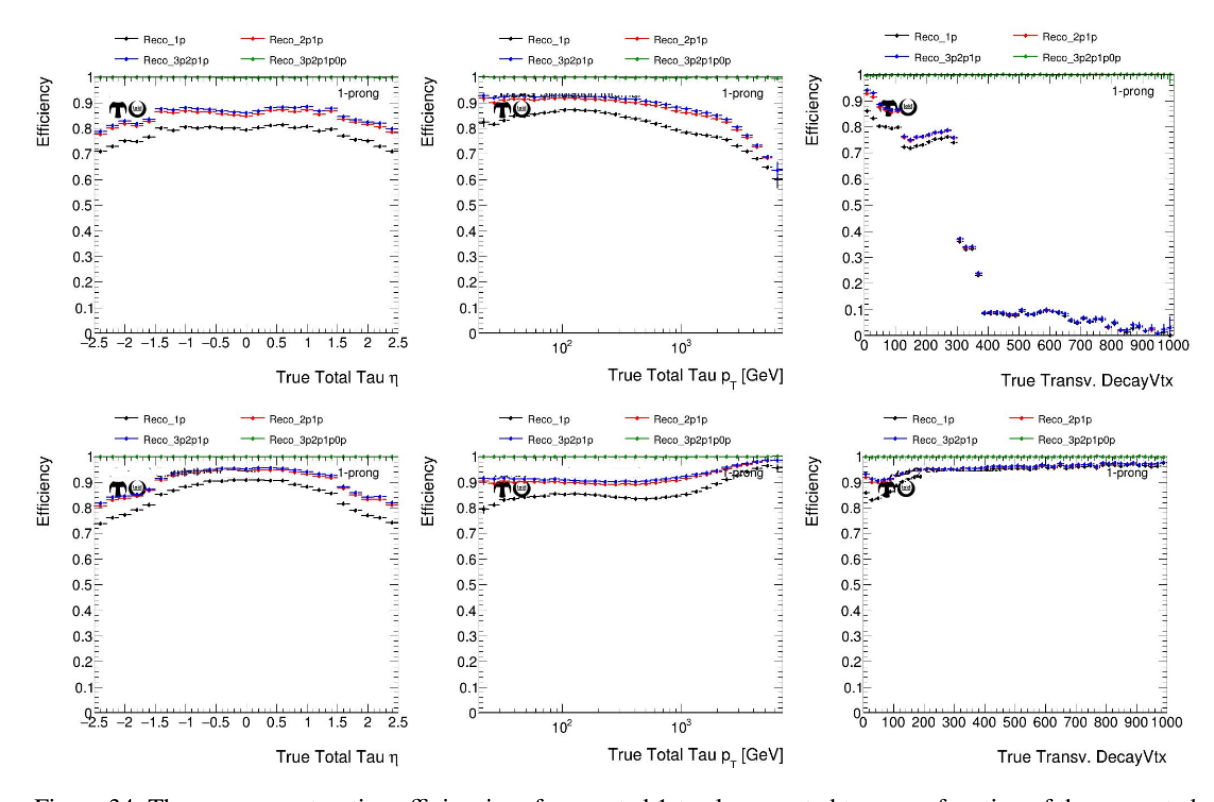


Figure 34: The  $\tau_{had}$  reconstruction efficiencies of generated 1-track generated taus as a function of the generated  $\tau$ - $\eta$  (left),  $p_T$  (middle) and decay vertex transverse distance in mm (right). The top plots show the case where taus hits are not simulated, and the bottom plots show the case where they do. The black lines show the reconstruction efficiency of generated 1-prong taus to be reconstructed as 1-prong taus, the red lines show the reconstruction efficiency of generated 1-prong taus to be reconstructed as 1 or 2 prong-taus and the blue and green lines to be reconstructed as 1,2 or 3 and 0,1,2 or 3 prong taus respectively.

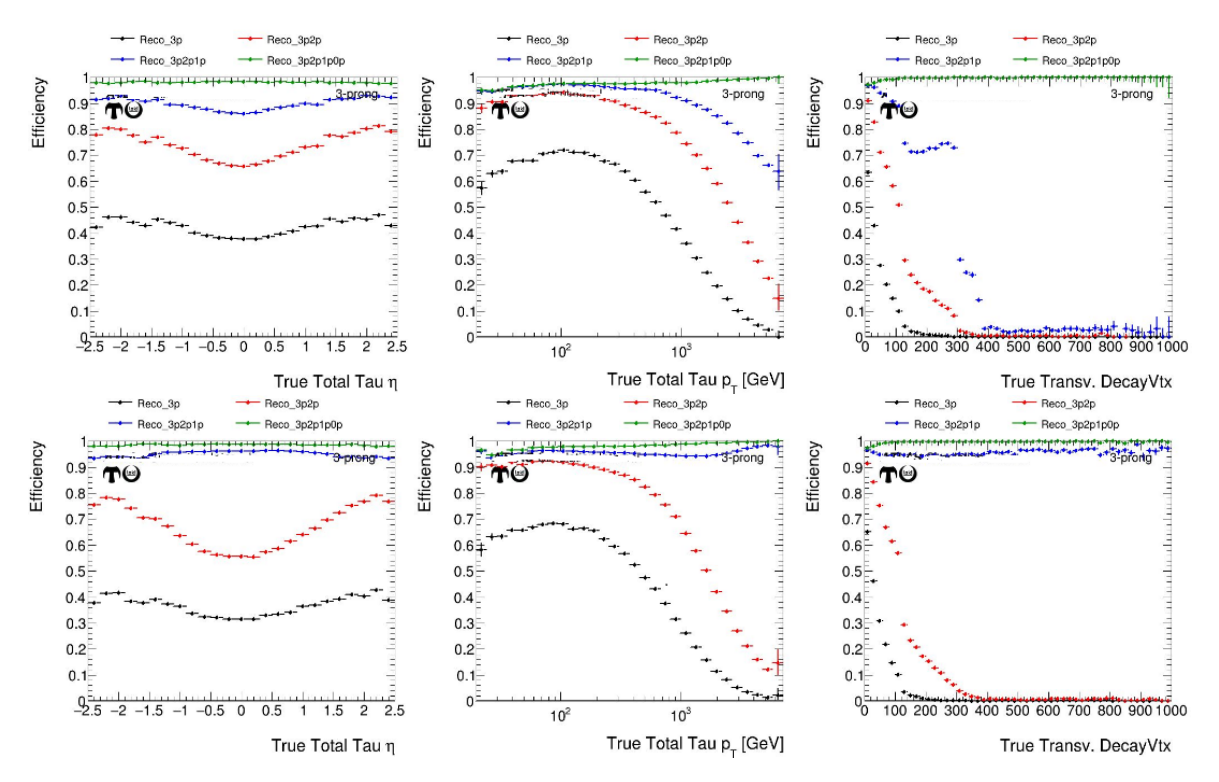


Figure 35: The  $\tau_{\rm had}$  reconstruction efficiencies of generated 3-track generated taus as a function of the generated  $\tau$ - $\eta$  (left),  $p_{\rm T}$  (middle) and decay vertex transverse distance in mm (right). The top plots show the case where taus hits are not simulated, and the bottom plots show the case where they do. The black lines show the reconstruction efficiency of generated 3-prong taus to be reconstructed as 3-prong taus, the red lines show the reconstruction efficiency of generated 3-prong taus to be reconstructed as 3 or 2 prong-taus and the blue and green lines to be reconstructed as 1,2 or 3 and 0,1,2 or 3 prong taus respectively.

#### 5.5.2 Uncertainties on the truth-level correction weights

Correction factors were also measured using a flat  $\gamma \to \tau \tau$  sample generated with Pythia8. The correction factors from the  $\gamma \to \tau \tau$  sample were compared to those from the  $W' \to \tau \nu$  sample, and the differences were used as a systematic uncertainty in the fit results. These differences may arise from the distinct polarization of the  $\tau$ -leptons and the differing kinematics of the final events. Including the  $\gamma \to \tau \tau$  measurement as a systematic is useful, as the correction factors are applied universally to all simulated  $\tau$ -leptons, independent of their origin.

#### 5.5.3 Results

The high- $p_{\rm T}$  calibration factors for 1- and 3-prong reconstructed  $\tau_{\rm had\text{-}vis}$  are shown in Fig. 39. The impact of applying the correction factors on the simulated SM backgrounds and a sample of SSM W'  $m_{\rm T}$  distributions is shown in Fig. 37 and 38. The application of the correction factors reduces the SM background by 3–5%. At the same time, it significantly boosts the SSM signal yields in the high- $m_{\rm T}$  bins. This is expected, as for high-mass signals the  $\tau$ -leptons are produced with higher  $p_{\rm T}$ , which amplifies the impact of the correction factors.

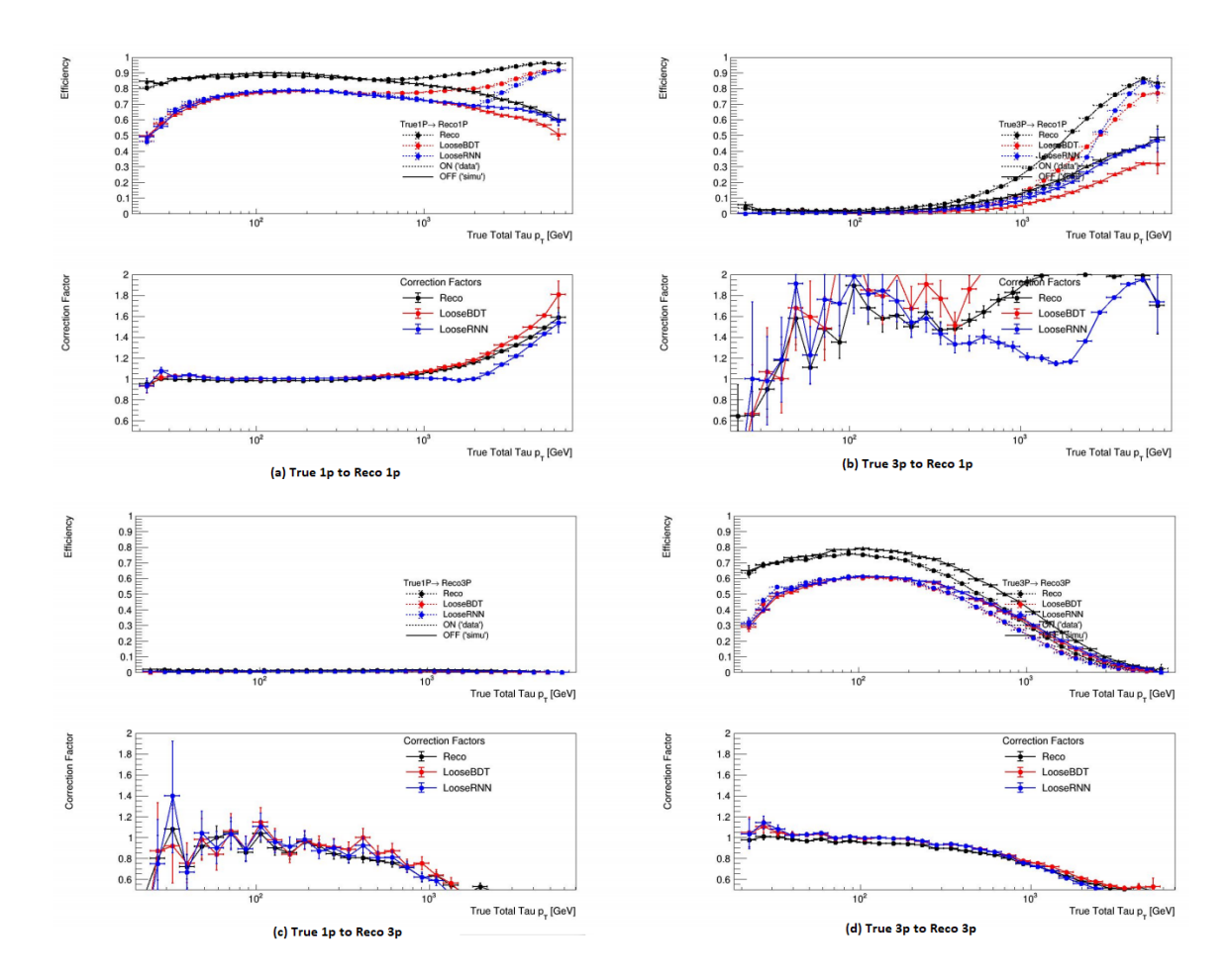


Figure 36: The efficiencies and calibration factors as a function of the generated total  $\tau$ - $p_T$  for the  $W' \to \tau \nu$  and different decay mode migrations. For each case, the top figure shows the reconstruction efficiency (black), and the combined reconstruction and RNN Loose identification efficiency (blue) or deprecated BDT Loose identification efficiencies. They are shown both with the effects of long-lived particles included (dotted lines) and without them (solid lines). The bottom plots display the ratio of these two efficiencies, providing the calibration factors. In most of the cases the RNN calibration factors are closer to unity suggesting a better expected agreement between data expectations and MC efficiencies.

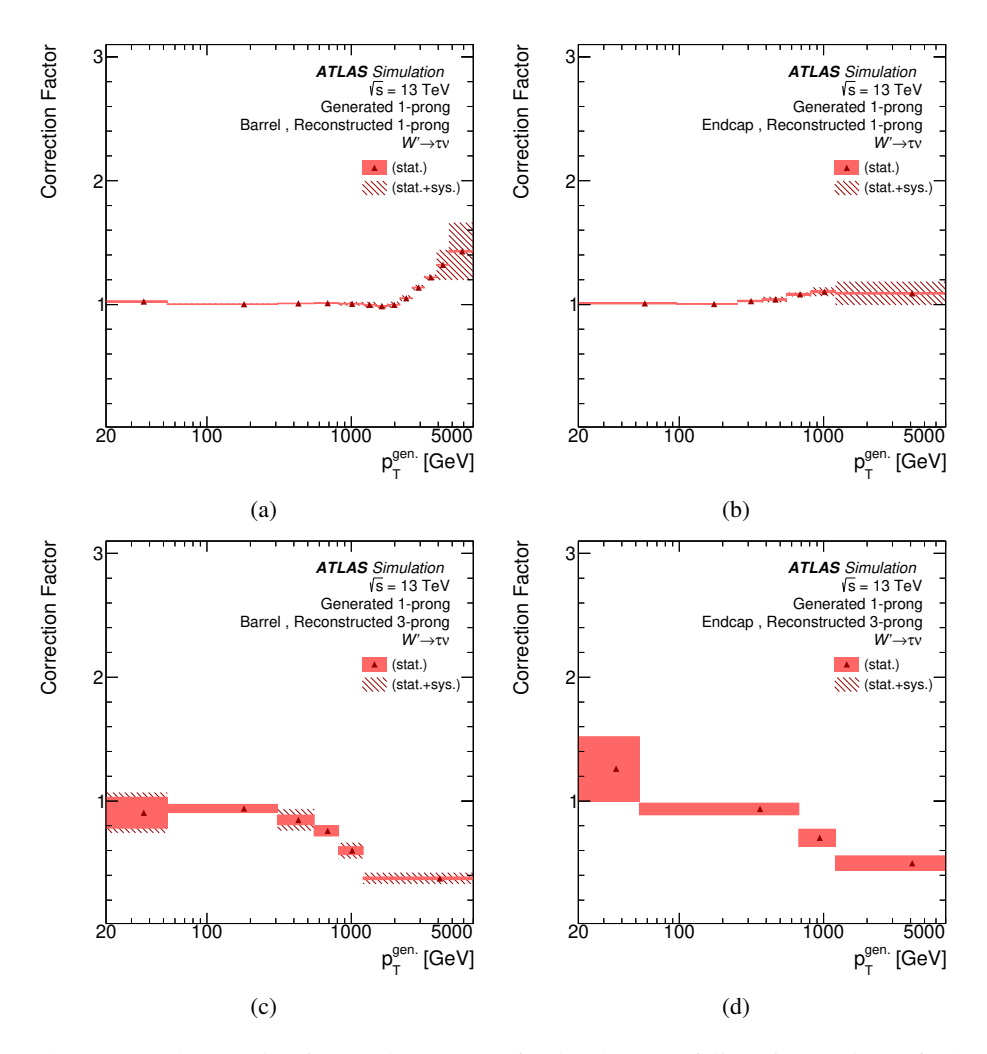


Figure 37: The measured correction factors that account for the absence of direct interactions of  $\tau$ -leptons with the detector material in the simulation for  $\tau$ -leptons decaying into one charged hadron. The correction factors are shown for generated 1-prong  $\tau$ -lepton decays reconstructed as (a) 1-prong  $\tau$ -lepton candidates in the central detector region, (b) 1-prong  $\tau$ -lepton candidates in the outer detector region, (c) 3-prong  $\tau$ -lepton candidates in the central detector region, (d) 3-prong  $\tau$ -lepton candidates in the outer detector region, as a function of the generated  $\tau$ -lepton momentum,  $p_{\rm T}^{\rm gen}$ .

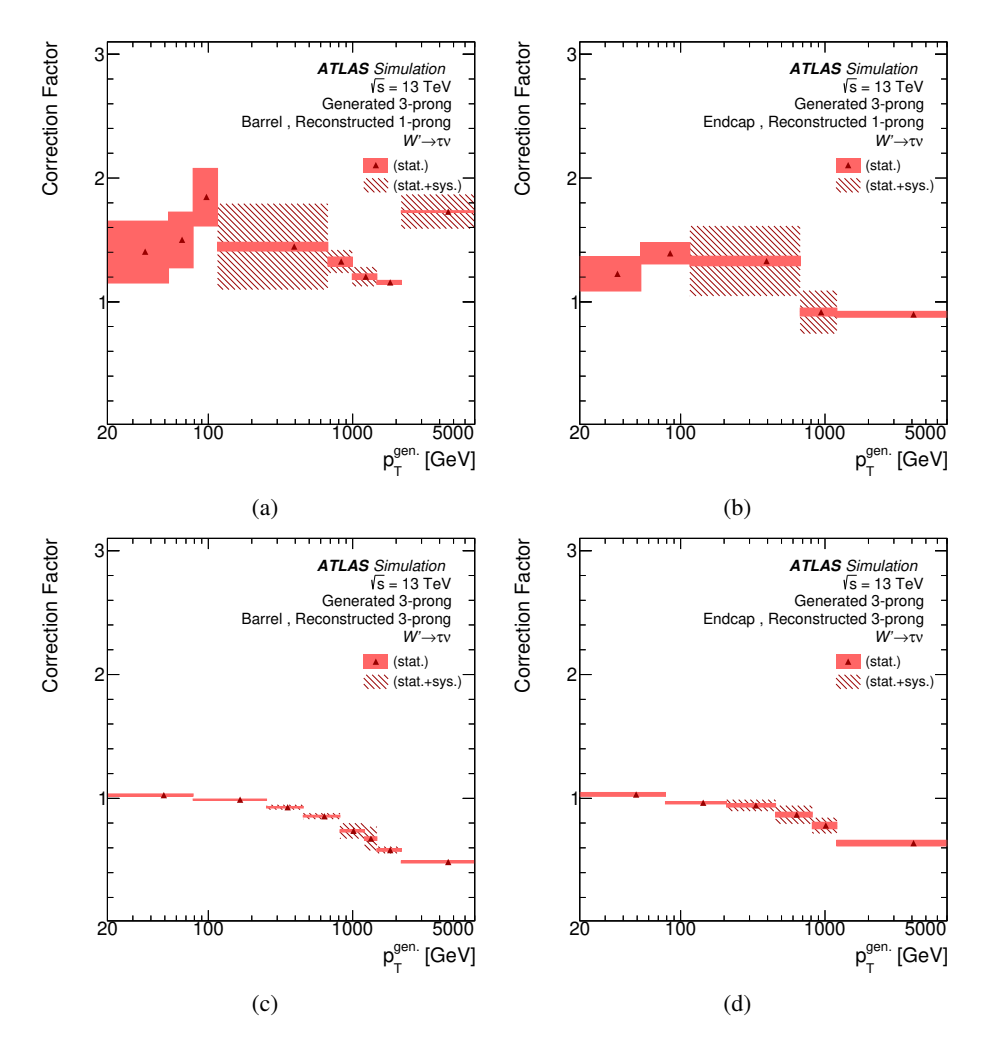


Figure 38: The measured correction factors that account for the absence of direct interactions of  $\tau$ -leptons with the detector material in the simulation for  $\tau$ -leptons decaying into three charged hadron. The correction factors are shown for generated 3-prong  $\tau$ -lepton decays reconstructed as (a) 1-prong  $\tau$ -lepton candidates in the central detector region, (b) 1-prong  $\tau$ -lepton candidates in the outer detector region, (c) 3-prong  $\tau$ -lepton candidates in the central detector region, (d) 3-prong  $\tau$ -lepton candidates in the outer detector region, as a function of the generated  $\tau$ -lepton momentum,  $p_{\rm T}^{\rm gen}$ .

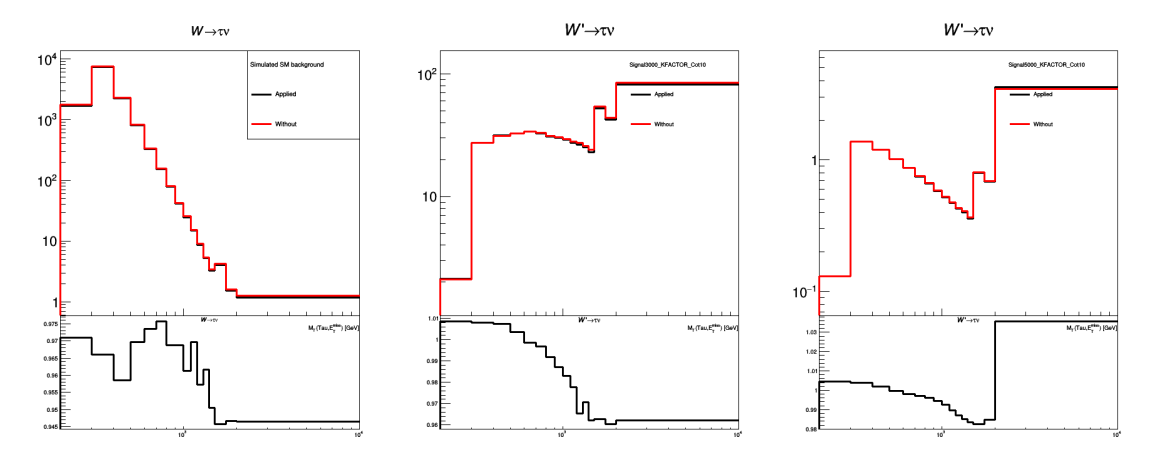


Figure 39: The transverse mass distributions of the SM background (left) and 3 TeV (middle) and 5 TeV SSM signal mass hypotheses. The  $m_{\rm T}$  distributions after applying the correction factors is shown in black, while the  $m_{\rm T}$  distribution shown in red is without these correction factors. The ratio on the bottom pads shows the effect the correction had on the distribution yields.

## 5.6 Systematics

This section outlines the systematic uncertainties and their effects on the estimated SM background and the W' signal. These uncertainties can arise from experimental sources, such as intrinsic uncertainties in determining the  $\tau_{\text{had-vis}}$ - $p_{\text{T}}$  or identification efficiencies, or from theoretical sources, like uncertainties in process cross-sections.

However, as detailed in Sec. 5.7 the analysis is statistically limited, meaning that systematic uncertainties minimally impact the results. The primary constraint in excluding high-mass signal hypotheses is the restricted dataset size.

#### 5.6.1 Experimental uncertainties

The main source of experimental uncertainty originates from the tau energy scale (TES). The TES uncertainty has been evaluated centrally by ATLAS using MC and data with  $Z \to \tau\tau$  samples and is 3%–4% on the  $\tau_{\text{had-vis}}$ - $p_{\text{T}}$  [22]. The impact of this uncertainty is found to vary with  $m_{\text{T}}$ , from 2% at  $m_{\text{T}} = 200\,\text{GeV}$  to 10% at  $m_{\text{T}} = 2\,\text{TeV}$  for a signal with  $m_W' = 5\,\text{TeV}$  TeV, from 10% to 40% for  $W \to \tau \nu$  and from 15% to 45% for the other backgrounds. It is the largest systematic uncertainty for the simulated backgrounds.

A secondary source of experimental uncertainty originates from correctly measuring the  $\tau_{\text{had-vis}}$  identification and reconstruction efficiencies (collectively called  $\tau_{\text{had-vis}}$  efficiency). This contains the following sources:

- Identification efficiency: The uncertainty in the τ-lepton identification efficiency is 5%-6%, as determined from measurements of Z → ττ events [22]. For τ<sub>had-vis</sub>-p<sub>T</sub> beyond the range of 100 GeV that can be probed with Z → ττ decays, this uncertainty is inflated by 9% per TeV for 1-prong and 6% per TeV for 3-prong candidates, in accordance with studies of high-p<sub>T</sub> jets [85].
- Reconstruction efficiency: The tau reconstruction efficiency uncertainties are evaluated with MC studies of Z → ττ samples, in which the experimental setup is modified, e.g. by changing the amount of the dead material. An additional uncertainty of 22.5%/TeV is used for 3-prong τ<sub>had-vis</sub> with p<sub>T</sub> >150 GeV to account for potential mismodeling of the track merging probability. This results in a reconstruction uncertainty of about 1–3%, depending on the m<sub>T</sub> value.
- Electron veto efficiency: This uncertainty is measured in Z → ee simulated samples [22]. For
  the tau-electron identification efficiency and the analysis relevant kinematics, the uncertainty is
  about 2%.
- High- $p_{\rm T}$  tau reconstruction corrections: These are the uncertainties in the correction factors applied to account for missing tau hits in the inner detector, as discussed in Sec. 5.5.2. This uncertainty ranges from 0.5% at  $m_{\rm T} \approx 200$  GeV to 2% for  $m_{\rm T}$  above 3 TeV.

Additional subdominant source of experimental uncertainties were also considered in this search. These are summarized below and collectively referred to as "Other" in the following sections.

• Jet Energy Scale/Resolution: The jet energy scale and resolution uncertainties [86] are included in this study. While jets are not directly involved in this analysis, their measured energy can indirectly influence the  $E_{\rm T}^{\rm miss}$  measurement. The impact of these uncertainties is of the order of 2% for the signal of 5 TeV and  $W(\to \tau \nu)$  background.

- Missing transverse energy: Uncertainties related to the determination of the  $E_{\rm T}^{\rm miss}$  soft-term scale and resolution [87] are considered. Since the soft-term contribution is relatively small in comparison to the total  $E_{\rm T}^{\rm miss}$  from neutrinos in this analysis, the effect of these uncertainties is minimal. The impact reaches up to 1% for the signal  $(m_{W'} == 5 \text{ TeV})$  and the  $W(\to \tau \nu)$  background.
- Trigger efficiency scale factors: As discussed in Sec. 5.4, the trigger efficiency scale factors for each trigger and their uncertainties are measured in  $Z(\to \mu\mu)+jets$ ,  $W(\to \mu\nu)+jets$  and  $t\bar{t}$  events up to  $E_{\rm T}^{\rm miss}$  of 360 GeV. The statistical uncertainty of the scale factors is of the order of 5% and drops to approximately 1% as  $E_{\rm T}^{\rm miss}$  increases. Above  $E_{\rm T}^{\rm miss}$  of 360 GeV the trigger effects on data and simulation are assumed identical and the scale factors are set to unity with no uncertainty. The envelope of the differences between  $Z(\to \mu\mu)+jets$  and  $W(\to \mu\nu)+jets$  or  $t\bar{t}$  scale factors represents the systematic uncertainty, reaching up to 10%. The overall impact of the trigger scale factor uncertainties on the signal and background yields varies from 10% at low- $m_{\rm T}$  of 200 GeV up to 0% for high- $m_{\rm T}$  ( $m_{\rm T}$  above 1 TeV).
- **Luminosity**: The uncertainty in the combined 2015–2018 integrated luminosity of 139 fb<sup>-1</sup> is 1.7 % [88], obtained using the LUCID-2 detector [4] for the primary luminosity measurements.
- **Pile-up uncertainty**: The impact of pile-up reweighting uncertainties was found to give a systematic uncertainty of up to 1% for the signal, sub-percent for  $W \to \tau \nu$  and other backgrounds.

### 5.6.2 Jet background uncertainties

The fake factor method assumes that the weights calculated in CR2 and CR3 are also valid for CR1. To assess the effect the dijet CRs selection criteria have on the et background event yield, and thus the applicability of the fake factors, the defining cuts of the control regions are varied. By measuring the impact these variations have on the jet background distributions, the systematic uncertainties associated with the fake factors can be quantified.

For all the systematic sources that are not directly linked to the fitted function, the impact on the nominal distribution of the jet background was evaluated. These variations were later propagated through a set of 10,000 pseudo-experiments, where the jet background  $m_{\rm T}$  distribution was allowed to vary. For each pseudo-experiment, the same function as the nominal case was fitted and the jet background  $m_{\rm T}$  was smoothened. The differences between the jet background  $m_{\rm T}$  distributions in the pseudo-experiments and the nominal distribution were used to derive the per-bin uncertainty of the jet background at the 68% confidence level. This approach provided a natural way to include the impact of inter-bin correlations of the jet background uncertainties. The following variations were studied:

• Variation of  $E_{\rm T}^{\rm miss}$  criteria: The low- $E_{\rm T}^{\rm miss}$  region in which the CR2 and CR3 are defined was varied. The upper threshold of 100 GeV was increased to 150 GeV accepting more signal-like events. Alternative low- $E_{\rm T}^{\rm miss}$  regions were defined, but instead of altering the upper threshold, the lower threshold was varied from 0 GeV up to 70 GeV, thus rejecting events that do not resemble the signal-like backgrounds. This approach can also partially target the systematic uncertainty for defining the CR2 and CR3 below the trigger efficiency plateau. For each variation, the jet background in the SR was estimated with the new fake factors. The uncertainty on the

jet background yields was taken as the maximum distance between the nominal expectation and each variation. This systematic impacts the jet background yields from 2% at low- $m_T$  to 16% at high- $m_T$ .

- Quark/gluon ratio differences: An important factor to consider is the similarity in quark- and gluon-initiated jet ratios between the jet backgrounds in CR1 and CR3. In the signal-like region CR1, it's expected that high- $p_{\rm T}$  quarks are the primary source of the jet background, whereas the quark/gluon-initiated jet fraction may differ in the low- $E_{\rm T}^{\rm miss}$  region. The width of the jet seeding the reconstructed tau candidate provides an effective discrimination between quark-and gluon-initiated jets, with the gluon jets typically producing wider jets [89]. To quantify a systematic uncertainty for the assumption of similar quark/gluon fractions in CR1 and CR3, the tau-lepton's jet seed width distributions were compared between these regions. To remove differences arising from the different  $\tau_{\rm had-vis}$ - $p_{\rm T}$  spectra in the two regions, the regions are reweighted to match their  $\tau_{\rm had-vis}$ - $p_{\rm T}$  spectra. The residual differences in the tau jet seed width between CR3 and CR1 were then applied as reweighting factors in CR1 before applying the fake factors. Moreover, the fake factors were additionally binned in jet seed width intervals to account for dependence on this variable. The impact of this approach on the jet background varied from 3% at low- $m_{\rm T}$  to 13% at high- $m_{\rm T}$ .
- Extrapolation of fake factor: As mentioned before, the last  $\tau_{\text{had-vis}}$ - $p_{\text{T}}$  bin of the fake factor  $F_{ij}$  was calculated for up to 500 GeV. To access the impact of neglecting events beyond that level, the fake factors were recalculated for  $\tau_{\text{had-vis}}$ - $p_{\text{T}}$  up to 1 000 GeV. This systematic uncertainty affects the jet background yields, ranging from 2% at low- $m_{\text{T}}$  to 16% at high- $m_{\text{T}}$ .
- **Subtraction of simulated background**: As shown in Eq. 5.2, the calculation and application of fake factors involves the subtraction of simulated background from data. This simulated background, comes with intrinsic experimental and theoretical systematic uncertainties. The total systematic uncertainty of the simulated background was propagated in the fake factor calculation and application. This affects mostly the CR1 which posits the highest real lepton and tau contamination. The impact of the systematic uncertainties of the simulated background on the jet background yields is asymmetric and ranges from 2% at low- $m_T$  to 17% at high- $m_T$ .
- Functional fit: Fitting the  $m_{\rm T}$ -distribution with empirical functions may introduce systematic biases that originate from the choice of the functional form, its fitted range, as well as the bin size of the fitted data. To address these systematics, that affect the jet background only for  $m_{\rm T} > 500$  GeV, the following methods were implemented. For the choice of function, as mentioned in Sec. 5.3.2, the difference between the nominal function and the alternative function that also fitted well the jet background data is used. This systematic can drive the jet background uncertainty up to 58% at high- $m_{\rm T}$ . For the fitted ranges, the lower and upper fitted ranges were varied by  $\pm 50$  GeV. The lower threshold variation leads to differences in the jet background of up to 19%. The fit result is not very dependent on the upper threshold, and thus this impacts the jet background by up to 2% at high- $m_{\rm T}$ . Finally, for the  $m_{\rm T}$ -binning, the jet background data were rebinned into wider bins before attempting to fit the nominal function. This rebinning also had minor impact on the jet background, affecting it by up to 2% at high- $m_{\rm T}$ .

Other source of systematic uncertainty on the jet background that was considered but found to give negligible effects (sub-percent), was the propagation of the statistical uncertainty of the fake

factors, originating from the limited size of the CR2 and CR3. The experimental uncertainties of the jet background as a function of  $m_{\rm T}$  are shown in Fig. 40 and a sample of their values for different  $m_{\rm T}$  bins is given in Tab. 5.8.

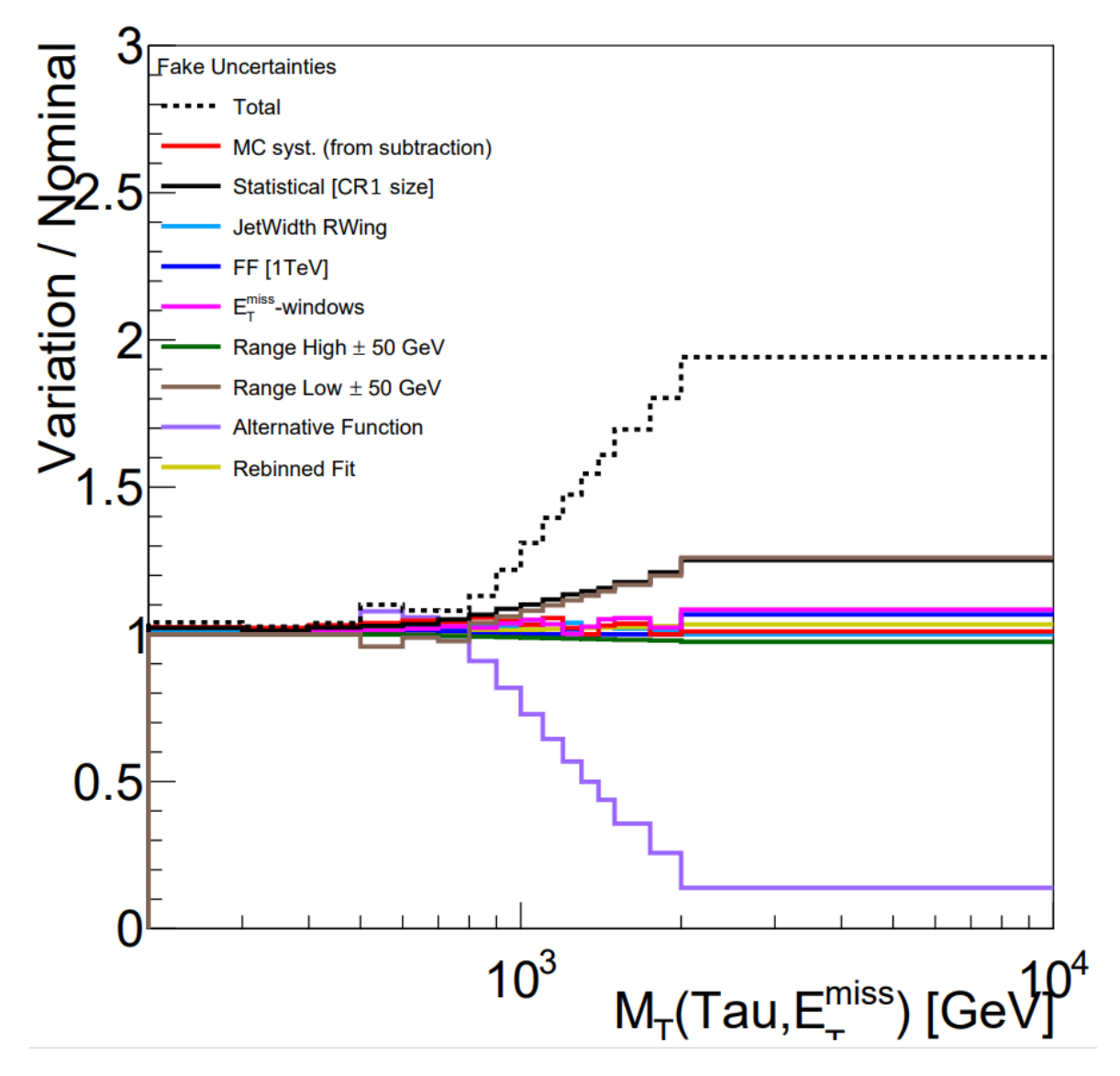


Figure 40: The relative upward-uncertainties on the  $m_{\rm T}$ -distribution of the fake estimate of the statistical and the statistical and systematic variation in the SR for all years.

Table 5.8: Summary of the uncertainties in the jet background estimate. The "···" symbol indicates that the	he
uncertainty source is not applicable in the relevant $m_{\rm T}$ range.	

Systematic uncertainty	Relative uncertainty in the j $200 \text{GeV} < m_{\text{T}} < 300 \text{GeV}$	_
Non-jet background subtraction	+2/-3	+2/-17
Variation of $E_{\rm T}^{\rm miss}$ thresholds	± 2	± 16
Quark/gluon ratio differences	± 3	± 13
Extrapolation of transfer factor	±2	±16
Alternative fit function	•••	± 58
Lower fit range ±50 GeV	•••	± 19
Higher fit range ±50 GeV	•••	± 2
$m_{\mathrm{T}}$ rebinning		± 2

#### 5.6.3 Theoretical uncertainties

The theoretical uncertainties refer to uncertainties related to the simulated processes' cross-sections. For the signal, W and Z processes, the uncertainty of the cross sections was studied using variations of several parameters that affect the mass-dependent k-factors,  $k_F$ . The uncertainty attributed to the determination of the k-factors were obtained from combining the following sources:

- $\alpha_S$  uncertainty: The k-factors were recalculated by adjusting the strong coupling constant,  $\alpha_S$ , from the CT14NNLO PDF set's default value of 0.13 to 0.118 [90].
- **PDF uncertainty**: the higher-order corrections were re-evaluated using the 90% confidence level (CL) eigenvector variations from the nominal CT14NNLO PDF set.
- PDF set choice uncertainty: The impact of the choice of PDF set was determined by comparing the values obtained from CT14NNLO to those of the ATLAS-epWZ16 [91] and NNPDF3.0 PDF sets, following prescriptions as described in Ref. [92].
- Scale uncertainties: The uncertainty of the normalization and factorization scale of the W/Z bosons were also considered. They were determined by scaling the respective scales up and down by a factor of two.
- **Photon-induced correction**: For the Z processes, the photon induced corrections to the higher-order correction were taken into account. The latter arise from theoretical initial state radiation of photons.
- Electroweak correction uncertainty: The k-factors are calculated by the "multiplicative approach",  $k_F = (K_{\rm QCD}/K_{\rm LO}) \times K_{\rm EW}$ , where  $K_{\rm QCD~(EW)}$  is the QCD (EW) higher-order corrections and  $K_{\rm LO}$  the LO cross-section, instead of the nominal "additive approach" (recommended in [93]), where the higher-order corrections are added together,  $k_F = K_{\rm QCD} + K_{\rm EW} K_{\rm LO}$ .

Both approaches are theoretically motivated and they cover the true value of the higher-order corrections. These corrections were not taken into account for the signal W' process, as they strongly depend on the model assumptions [84].

The combined  $k_F$  uncertainties, calculated as the sum in quadrature of the above, are the largest source of theoretical uncertainty in this analysis. Their impact on the  $m_T$  distribution of the simulated background ranges from 4% at  $m_T \approx 200\,\text{GeV}$  to 15% for  $m_T$  above 2 TeV. For the W' signal, the theory uncertainty increases from 2.4% to 81% with  $m_T$  and the mass of the W'. For the purpose of deriving exclusion upper limits on the cross-section (Sec. 6), the signal theory uncertainty is not included in the fit. Instead, it is used to calculate the cross-section uncertainty band of the W' in the illustration. This approach reduces the model dependence of the experimentally derived limits. Consistent with previous similar searches[84], the impact of theory uncertainties on the signal acceptance are not taken into account in this study.

The rest theoretical uncertainties are derived by dedicated measurements. Their impact in the analysis is small because they mainly affect subdominant backgrounds.

- $t\bar{t}$  cross-section: The predicted  $t\bar{t}$  production cross-section is  $\sigma_{t\bar{t}} = 831.76^{+40}_{-46}$  pb after combining the scale and PDF+ $\alpha_S$  uncertainties in quadrature.
- Parton shower radiation, hadronization and fragmentation: Additional uncertainties originating from the parton shower radiation and hadronization/fragmentation are evaluated by using alternative simulated samples. This have an overall impact on the other backgrounds of the order of 8% throughout the  $m_T$  distribution.
- Single top cross-section: The predicted t-channel single-top (anti-top) cross-section for pp collisions at  $\sqrt{s}$  =13 TeV is  $\sigma_t^{\text{t-chan}}$  =  $136.02^{+5.4}_{-4.57}$  ( $\sigma_{\bar{t}}^{\text{t-chan}}$  =  $80.95^{+4.06}_{-3.61}$ ) pb. The predicted s-channel single-top (anti-top) cross-sections are  $\sigma_t^{\text{s-chan}}$  =  $6.35^{+0.23}_{-0.2}$  ( $\sigma_{\bar{t}}^{\text{s-chan}}$  =  $3.97^{+0.19}_{-0.17}$ ) pb. Finally, the Wt channel cross-section is  $\sigma_{Wt}$  =  $71.7 \pm 3.8$  pb.
- **Diboson cross-section**: The diboson cross-section uncertainty is taken to be 10% combining PDF+ $\alpha_S$  and scale variation uncertainties in quadrature.

The overall cross-section and top-modeling uncertainties have an impact on the other backgrounds that does not exceed the 10% throughout the  $m_{\rm T}$  distribution. The summary of all theoretical-based uncertainties on the cross-sections are given in Tab. 5.9.

Sample	Uncertainty on cross-section
$W \to (\tau/\ell)\nu$ $Z \to (\tau\tau/\ell\ell)$	k-factor uncertainties (5-20%) k-factor uncertainties (5-20%)
$t\bar{t}$	+4.8/-5.5 %
s-chan. single (anti-)top	+3.6/-3.1 (4.8/-4.3) %
<i>t</i> -chan. single (anti-)top	+4.0/-3.4 (5.0/-4.5) %
Wt single top	±5.3 %
Diboson	±10 % Norm.

Table 5.9: The summary of the theoretical uncertainties used for each sample's cross-section.

## 5.7 Background validation

An alternative validation region (VR) is defined (see Tab. 5.1) to validate the SM background estimate in a high- $E_{\rm T}^{\rm miss}$  region with data. The VR definition is similar to the signal region, but requires an imbalance between the  $\tau_{\rm had\text{-}vis}$ - $p_{\rm T}$  and the  $E_{\rm T}^{\rm miss}$ :  $\tau_{\rm had\text{-}vis}$ - $p_{\rm T}$  / $E_{\rm T}^{\rm miss}$  < 0.7. To better match the conditions in the signal region, an  $m_{\rm T}$  requirement of 240 GeV or higher is applied. The reversal of the ratio  $\tau_{\rm had\text{-}vis}$ - $p_{\rm T}$  / $E_{\rm T}^{\rm miss}$  in the VR definition results in negligible signal contamination, making this region ideal for validating the background prediction against the data. The data versus background distributions of some variables in the VR are shown in Fig. 41.

No statistically significant deviations are observed, indicating that the background modeling describes the observed data well. Thus, no additional systematic uncertainty is derived from this closure test. This comparison also gives confidence to the jet background estimation method, which relies on the applicability of the transfer factors measured in events with low- $E_{\rm T}^{\rm miss}$  (below the trigger efficiency plateau), to events of high- $E_{\rm T}^{\rm miss}$ .

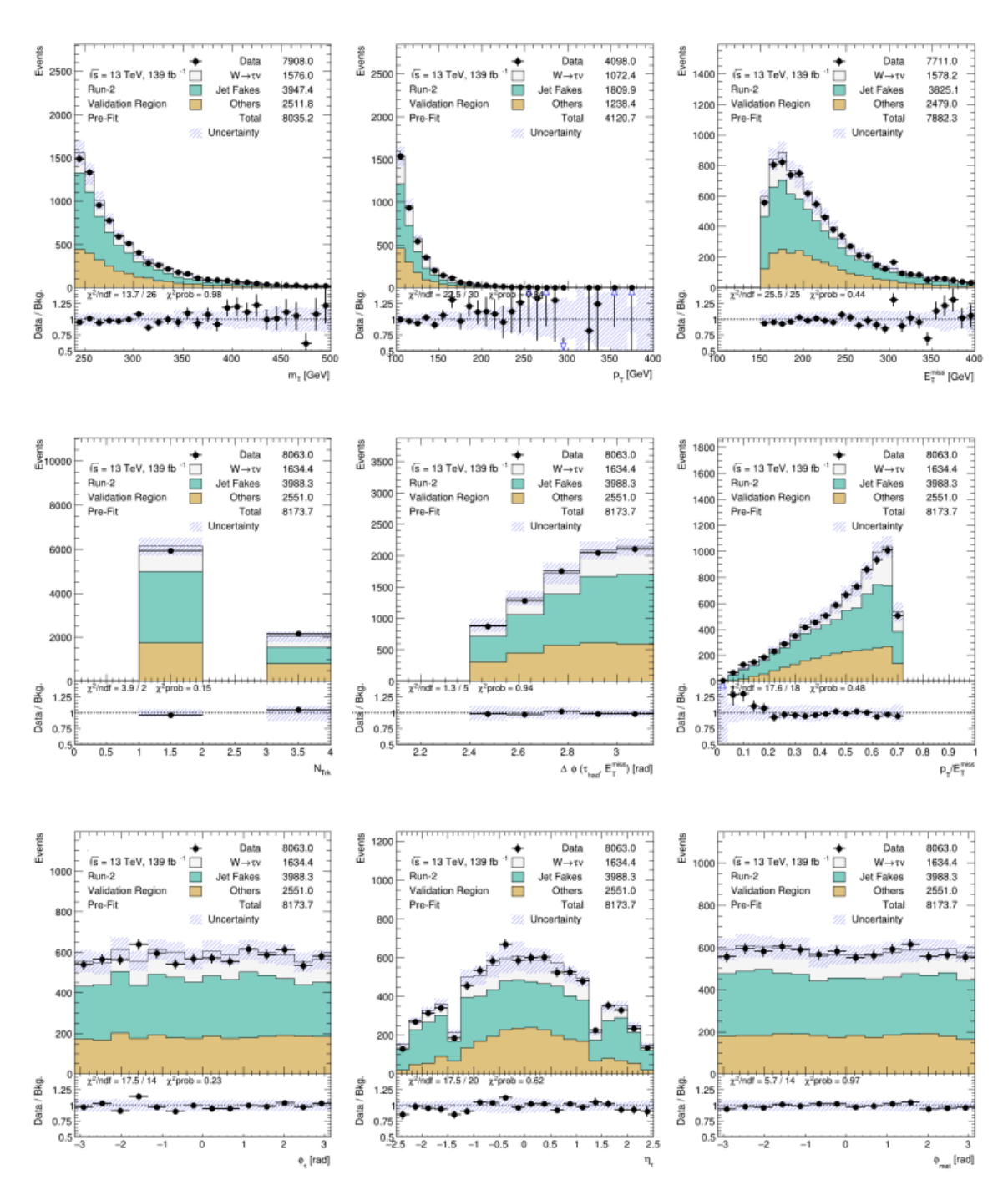


Figure 41: Variable distributions in the VR for data collected in the years 2015-2018. There is a good agreement between data and the SM background estimate. The shown uncertainties (hashed area) are coming from the statistical and systematic uncertainties.

## **Statistical Inference**

## 6.1 Hypothesis Testing

The discovery of a new particle in relies on statistically significant deviations from the expected background. To quantify the evidence of a discovery, a test statistic is used which assesses the compatibility of the observed data with the "null" hypothesis (background-only model),  $H_0$ , and compare it with the "alternative" hypothesis (signal-plus-background model),  $H_1$ . The null hypothesis assumes that the data is well described by the background-only model, i.e. there is no significant signal contribution in the observation, whereas the alternative hypothesis suggests otherwise. This section outlines the concept, formalism and interpretation of the discovery significance test statistic.

As mentioned in Section 5.1, the search for new physics phenomena is performed on the distribution of the transverse mass of the tau visible decay products and the missing transverse momentum. The main goal of the statistical analysis is to provide an answer of how likely the observed  $m_{\rm T}$  distribution is described by the "null" hypothesis (Standard Model expectation) against an "alternative" hypothesis (New Physics model). The statistical model that is used in this analysis is described in Section 6.1.1, while the results of the statistical inference in the analysis are discussed in Section 6.2

#### 6.1.1 The Likelihood Model

The binned likelihood function is defined as:

$$L(\mu, \theta) = \prod_{i=1}^{N_{\text{bins}}} \text{Pois}(n_i \mid b_i + \mu s_i) \times \prod_{\theta} f(\tilde{\theta} \mid \theta)$$
 (6.1)

where

- Pois $(n_i \mid b_i + \mu s_i)$  is the Poisson probability of observing  $n_i$  events in the bin i of some distribution x binned in  $N_{\text{bins}}$  bins, given the expected number of signal  $(s_i)$  and background  $(b_i)$  events in that bin.
- $\mu$  is the *signal strength* or the parameter of interest, and is a normalization factor for the signal extracted from the fitting procedure. When  $\mu = 0$ , the results are consistent with the Standard Model prediction, while  $\mu = 1$  corresponds to the observed signal cross section matching the assumed cross section for New Physics.

• The nuisance parameters  $\theta$  encode the impact of systematic uncertainties (Sec. 5.6). These parameters are constrained by auxiliary measurements  $\tilde{\theta}$ , and the constraint is represented by the term  $f(\tilde{\theta} \mid \theta)$ . The constrain term is assumed to be a normal distribution.

The values of  $\mu$  and  $\theta$  are determined by maximizing the likelihood function during the fit procedure. In the unconditional Maximum Likelihood Fit (MLF), both the signal strength  $\mu$  and the nuisance parameters  $\theta$  are allowed to vary freely, yielding their best-fit values  $\hat{\mu}$  and  $\hat{\theta}$ . The resulting best-fit value  $\hat{\mu}$  quantifies the agreement between the observed data and the signal hypothesis, while the nuisance parameters  $\hat{\theta}$  account for systematic uncertainties.

In contrast, a conditional MLF is performed under a fixed assumption for the signal strength,  $\mu = \mu^*$ . In this case, the likelihood is maximized only with respect to the nuisance parameters  $\theta$ , yielding their conditional best-fit values,  $\hat{\theta}(\mu^*)$ .

These two types of fits are central to constructing the likelihood ratio test, which is discussed in the next section.

#### 6.1.2 The Likelihood Ratio Test Statistics

The likelihood ratio is used to define the test statistic, which compares the likelihood of the data under the null hypothesis ( $\mu = 0$ ) to that under the alternative hypothesis ( $\hat{\mu} > 0^1$ ). The likelihood ratio test statistic  $\lambda$  is defined as:

$$\lambda(\mu) = \frac{L(\mu, \hat{\theta})}{L(\hat{\mu}, \hat{\theta})}, \qquad (6.2)$$

where:

- $L(\mu=0,\hat{\theta})$  is the value of the conditional maximum likelihood under the null hypothesis (background-only model). As the product of a conditional fit, the nuisance parameters' best-fit values  $\hat{\theta}$  are determined by  $\mu=0$ .
- $L(\hat{\mu}, \hat{\theta})$  is the value of the unconditional maximum likelihood, corresponding to the best-fit signal-plus-background model.

The profile likelihood ratio  $\lambda$  quantifies how well the signal-plus-background model describes the data compared to the background-only model. A value of  $\lambda$  close to unity 1 indicates that the data are consistent with the null hypothesis, whereas smaller values indicate deviation from the null hypothesis.

Taking the natural logarithm of  $\lambda$  leads to the discovery test statistic:

$$q_{0} \equiv -2 \ln \lambda = \begin{cases} -2ln \frac{L(\mu=0,\hat{\theta})}{L(\hat{\mu},\hat{\theta})} & , \hat{\mu} \geq 0 \\ 0 & , \hat{\mu} < 0 \end{cases}$$
 (6.3)

The disagreement between the observed data and the null hypothesis is quantified via the p-value, which represents the probability of observing a test statistic  $q_0$  as extreme as  $q_0^{\text{obs}}$  or more, assuming the null hypothesis ( $\mu = 0$ ) is true:

<sup>&</sup>lt;sup>1</sup> Only positive New Physics signal contributions are considered.

$$p_0 = \int_{q_0^{\text{obs}}}^{\infty} f(q_0 \mid \mu = 0) \ dq_0 \tag{6.4}$$

Here,  $f(q_0 \mid \mu = 0)$  is the probability density function (pdf) of the test statistic  $q_0$  under the null hypothesis. Using Wald's approximation [94], this pdf can be expressed as a combination of a Dirac delta function and a chi-squared distribution with one degree of freedom:

$$f(q_0 \mid \mu = 0) = \frac{1}{2}\delta(q_0) + \frac{1}{\sqrt{8\pi q_0}} \exp(-q_0/2)$$
 (6.5)

The corresponding cumulative distribution function (cdf),  $F(q_0 \mid \mu = 0)$ , can be written in terms of the cumulative distribution of the standard normal distribution  $\Phi$ , which has zero mean and unit standard deviation:

$$F(q_0 \mid \mu = 0) = \Phi(\sqrt{q_0}) \equiv \int_{-\infty}^{q_0} \frac{1}{\sqrt{2\pi}} \exp(-q^2/2) \, dq \tag{6.6}$$

From this, the *p*-value is obtained as:

$$p_0 = 1 - \Phi(\sqrt{q_0}) \tag{6.7}$$

It is often useful to express the *p*-value in terms of the discovery significance Z, which corresponds to the number of standard deviations by which  $q_0^{\text{obs}}$  deviates from the null hypothesis:

$$Z = \Phi^{-1}(1 - p_0) = \sqrt{q_0}$$
(6.8)

A typical value for the discovery significance used in high-energy physics to reject the null hypothesis and claim a discovery corresponds to  $Z \ge 5$  ( $p = 2.87 \cdot 10^{-7}$ ).

For cases where the null hypothesis cannot be ruled out by observation, upper limits on the signal strength  $\mu$  can be set by slightly modifying the test statistic definition. The new test statistic  $q_{\mu}$  is defined as:

$$q_{\mu} \equiv -2 \ln \lambda' = \begin{cases} -2ln \frac{L(\mu, \hat{\theta})}{L(\hat{\mu}, \hat{\theta})} &, \hat{\mu} \geq \mu \\ 0 &, \hat{\mu} < \mu \end{cases}$$
 (6.9)

where  $\lambda'$  is the modified profile likelihood ratio. Here, the numerator  $L(\mu, \hat{\theta})$  is the conditional maximum likelihood under the signal-plus-background hypothesis  $\mu$ , and  $L(\hat{\mu}, \hat{\theta})$  remains the global maximum likelihood, as in the unconditional case.

The agreement between the observed data and a non-vanishing signal strength  $\mu$  is again quantified via the p-value. It is calculated similarly to the earlier case as:

$$p_{\mu} = \int_{q_{\mu}^{\text{obs}}}^{\infty} f(q_{\mu} \mid \mu) \, dq_{\mu} = 1 - \Phi(\sqrt{q_{\mu}}) \tag{6.10}$$

where  $f(q_{\mu} \mid \mu)$  is the pdf of the test statistic under the signal-plus-background hypothesis.

The upper limit of  $\mu$ , denoted as  $\mu_{\rm up}$  at a given CL 1 –  $\alpha$  is set by requiring  $p_{\mu} < 1 - \alpha^2$ . This

<sup>&</sup>lt;sup>2</sup> Typically  $\alpha = 0.05$  is used for 95% CL upper limits

corresponds to the value of  $\mu$  below which the signal-plus-background hypothesis can excluded at the chosen CL. Under the asymptotic approximation,  $\mu_{up}$  can be expressed as:

$$\mu_{\rm up} = \hat{\mu} + \sigma \Phi^{-1} (1 - \alpha) \tag{6.11}$$

where  $\sigma$  represents the uncertainty on the signal strength  $\hat{\mu}$ . The uncertainty  $\sigma$  is derived using the Asimov dataset, which is a representative dataset constructed to match the expected background and signal contributions under the null hypothesis.

To quantify the uncertainty on  $\mu_{\rm up}$ , the error bands  $\Delta \mu_{\rm up}$  are determined by varying the limit by N standard deviations <sup>3</sup>:

$$\Delta\mu_{\rm up} = \hat{\mu} + \sigma(\Phi^{-1}(1-\alpha) \pm N) \tag{6.12}$$

In order to avoid the over-exclusion of signal hypotheses in the presence of limited data or fluctuation, the  $CL_s$  method is used to derive upper limits on the signal strength. The  $CL_s$  method uses instead the following test statistic:

$$q_{0} \equiv -2 \ln \lambda = \begin{cases} -2ln \frac{L(\mu, \hat{\theta}_{\mu})}{L(\mu=0, \hat{\theta}_{0})} &, \hat{\mu} < 0\\ -2ln \frac{L(\mu, \hat{\theta}_{\mu})}{L(\hat{\mu}, \hat{\theta})} &, 0 \leq \hat{\mu} < \mu\\ 0 &, \hat{\mu} \geq \mu \end{cases}$$
(6.13)

where the  $\hat{\theta}_{\mu}$  corresponds to the best-fit value of  $\theta$  for a fixed  $\mu$ . Additionally, to avoid technical difficulties arising from negative pdf,the cases with  $\mu < 0$  are treated as  $\mu = 0$ . The quantity  $CL_s$  is then defined by:

$$CL_s = \frac{CL_{s+b}}{CL_b} \equiv \frac{p_{s+b}}{1 - p_b}$$
 (6.14)

where

- $p_{s+b} = \int_{q_{\mu}^{\text{obs}}}^{\infty} f(q_{\mu} \mid \mu, \hat{\theta}_{\mu})$  is the *p*-value for the signal-plus-background hypothesis.
- $p_b = \int_{-\infty}^{q_0^{\text{obs}}} f(q_0 \mid \mu = 0, \hat{\theta}_0)$  the *p*-value for the background-only hypothesis.

The *p*-values can either be determined from integrating the test statistic sampling distribution via pseudo-experiments or by asymptotic formulae [95].

The upper limit on the signal strength is then set by requiring  $CL_s < 1 - \alpha$ . An advantage of the  $CL_s$  method is that it avoids setting overly conservative exclusions in cases where there are downward fluctuations in the observed data. Also, by dividing by  $CL_b$ , the exclusion of signal hypotheses is not very aggressive when the data are consistent with background expectations.

## 6.2 Upper limits on Signal hypotheses

for model-dependent upper limits, the binned  $m_{\rm T}$  distribution is used to perform the final fit.

<sup>&</sup>lt;sup>3</sup> typically 1- and 2- $\sigma$  bands are quoted in searches.

#### 6.2.1 Fit procedure

To assess the discovery potential of this search, a background-only fit is performed on the data using the likelihood model described in the previous section. The nominal background histograms, along with their systematic variations (discussed in Sec. 5.6), are incorporated into the fit.

During the fitting procedure, it was observed that the dataset size in the low- $m_{\rm T}$  SR is highly sensitive to the  $\tau_{\rm had\text{-}vis}$  energy scale, resulting in an over-constraint of this nuisance parameter. To mitigate this, the original  $\tau_{\rm had\text{-}vis}$  energy scale uncertainty was divided into two correlated but independent nuisance parameters. These were defined based on their impact on the background processes for  $\tau_{\rm had\text{-}vis}$ - $p_{\rm T}$  >500 GeV ("HIGHPT") and  $\tau_{\rm had\text{-}vis}$ - $p_{\rm T}$  <500 GeV ("LOWPT"). This approach allows the low- $m_{\rm T}$  range of the SR to constrain the "LOWPT" nuisance parameter while leaving the "HIGHPT" parameter free to vary in the high-mass signal region. Consequently, the "HIGHPT" nuisance parameter could vary within the more conservative uncertainty estimate derived from the auxiliary measurement, thus ensuring that the fit remains robust in the regions most sensitive to potential high-mass signals. Checks on other  $\tau_{\rm had\text{-}vis}$ -related variables, such as the number of prongs or the  $\tau_{\rm had\text{-}vis}$ - $\eta$ , showed no significant changes in the observed constraints, and thus no additional divisions were deemed necessary (Fig. 42).

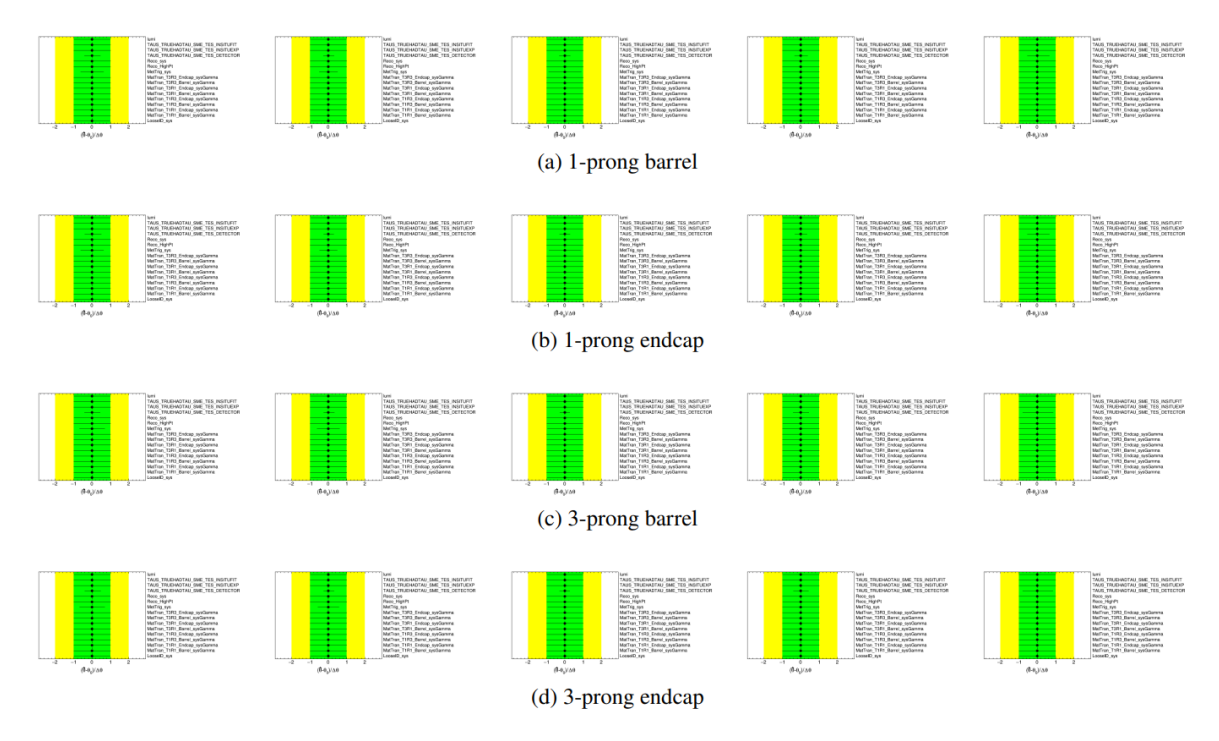


Figure 42: The constraints on some nuisance parameters used in the fit (using Asimov dataset) for the (a) 1-prong in barrel, (b) 1-prong in endcap, (c) 3-prong in barrel, (d) 3-prong in endcap. From left to right the plots show events in the  $\tau_{\text{had-vis}}$ - $p_{\text{T}}$  bins of [50,150], [150,200], [200,250], [250,500] and [500,  $\infty$ ) GeV. The most significant constrains appear for the  $\tau_{\text{had-vis}}$  energy scale nuisance parameter in the range of  $\tau_{\text{had-vis}}$ - $p_{\text{T}}$  < 500 GeV.

The binning of the  $m_{\rm T}$  distribution is selected by looking at different binning options and selecting the one that gives adequate expected events in the high mass bins, without significantly decreasing the search sensitivity. The different options considered are shown in Tab. 6.1 and the option **bin0** is selected. The event yields per bin for each background and two signal hypotheses with masses 3 TeV and 5 TeV are shown in Tab. 6.2.

A set of kinematic distributions after performing the background-only fit to the data is shown for the VR and SR in Fig.43 and Fig.44, respectively. After the background-only fit, the SM background agrees well with the observed data. This is evident in the distribution of  $m_{\rm T}$  in the SR, shown in Fig. 45. Two 4 TeV signal hypotheses for the  $m_{\rm T}$  distribution are overlaid with different couplings to the third generation. One corresponds to the SSM hypothesis and the other to large  $\cot\theta_{\rm E}$  (hereafter referred to as  $\cot\theta_{\rm NU}$ ). The agreement is illustrated in the bottom panel of Fig.45, showing the Poisson significance of the background-only model. This significance is calculated separately for each bin and is shown only for the bins where the p-value is less than 0.5 (indicating a "significant" occurrence), using the method described in Ref.[96]. Positive significances indicate excess of data, while negative significances correspond to data deficits.

Table 6.1: The binning for  $m_T$  used for each different Bin Option. Option 5 (bolded) is the one chosen for the analysis.

Bin Opt	Bin edges [GeV]
0	$\overline{[200,\!300,\!400,\!500,\!600,\!700,\!800,\!900,\!1000,\!1100,\!1200,\!1300,\!1400,\!1500,\!1750,\!2000,10000]}$
1	[200,300,400,500,600,700,800,900,1000, 1250, 1500,1750,2000,3000,10000]
2	[200,300,400,500,600,700,800,900,1000, 1250, 1500, 10000]
3	[200,300,400,500,600,700,800,900,1000, 10000]
4	[200, 400,500,600,700,800,900,1000, 1250, 1500,1750,2000,3000,10000]
5	[200,300,400,500,600,700,800,900,1000,1100,1200,1300,1400,1500,1750, 10000]

Table 6.2: The event yield for each  $m_{\rm T}$  bin with total uncertainty (statistical and systematic combined in quadrature). Additional yields are shown for two SSM signal hypotheses with mass 3 TeV and 5 TeV.

	<del>-</del>		31		
$m_{\mathrm{T}}$ [GeV]	(200,300)	(300,400)	(400,500)	(500,600)	(600,700)
$W(\to  au  u)$	$1110 \pm 180$	$5600 \pm 800$	$1800 \pm 270$	$660 \pm 110$	$270 \pm 40$
Jet Fakes	$1340 \pm 70$	$3320 \pm 150$	$760 \pm 40$	$210 \pm 23$	$74 \pm 8$
Others	$589 \pm 110$	$1660 \pm 300$	$450 \pm 90$	$139 \pm 24$	$57 \pm 12$
W'(3 TeV)	$2.1 \pm 0.4$	$27.4 \pm 2.5$	$31.3 \pm 2.2$	$32.7 \pm 2.5$	$33.9 \pm 2.7$
W'(5 TeV)	$0.131 \pm 0.016$	$1.38 \pm 0.09$	$1.20 \pm 0.05$	$1.01 \pm 0.05$	$0.87 \pm 0.04$
Total background	$3040 \pm 290$	$10600 \pm 1100$	$3000 \pm 300$	$1010 \pm 130$	$400 \pm 60$
$m_{\rm T}$ [GeV]	(700,800)	(800,900)	(900,1000)	(1000,1100)	(1100,1200)
$W(\to \tau \nu)$	$128 \pm 23$	$65 \pm 12$	$35 \pm 5$	$20 \pm 3$	$12 \pm 3$
Jet Fakes	$31 \pm 3$	$14.1 \pm 2.5$	$7.1 \pm 1.8$	$3.8 \pm 1.3$	$2.2 \pm 0.9$
Others	$24 \pm 6$	$14.0 \pm 2.5$	$6.5 \pm 1.8$	$4.9 \pm 1.8$	$3.0 \pm 0.9$
W' SSM (3 TeV)	$32.8 \pm 1.7$	$30.8 \pm 2.0$	$30 \pm 3$	$29.0 \pm 2.9$	$27.4 \pm 1.8$
W' SSM (5 TeV)	$0.75 \pm 0.04$	$0.66 \pm 0.03$	$0.58 \pm 0.04$	$0.52 \pm 0.04$	$0.470 \pm 0.029$
Total background	$183 \pm 28$	93 ± 14	$48 \pm 7$	$28 \pm 4$	$17 \pm 4$
$m_{\rm T}$ [GeV]	(1200,1300)	(1300,1400)	(1400,1500)	(1500,1750)	(1750,2000)
$W(\to \tau \nu)$	$7.1 \pm 2.0$	$4.4 \pm 1.4$	$2.7 \pm 0.8$	$3.4 \pm 1.1$	$1.3 \pm 0.5$
Jet Fakes	$1.3 \pm 0.7$	$0.8 \pm 0.5$	$0.5 \pm 0.3$	$0.7 \pm 0.5$	$0.28 \pm 0.24$
Others	$1.5 \pm 0.6$	$0.9 \pm 0.3$	$0.57 \pm 0.18$	$0.67 \pm 0.23$	$0.27 \pm 0.08$
W' SSM (3 TeV)	$26.3 \pm 2.3$	$25.1 \pm 1.8$	$23.0 \pm 1.7$	$52 \pm 4$	$42 \pm 4$
W' SSM (5 TeV)	$0.430 \pm 0.028$	$0.400 \pm 0.028$	$0.360 \pm 0.028$	$0.80 \pm 0.06$	$0.68 \pm 0.06$
Total background	$9.9 \pm 2.6$	6.1 ± 1.7	$3.8 \pm 1.1$	$4.7 \pm 1.4$	$1.8 \pm 0.6$
$m_{\rm T}$ [GeV]	(2000,10000)	Inclusive			
$W(\to \tau \nu)$	$0.9 \pm 0.4$	$9700 \pm 1400$			
Jet Fakes	$0.29 \pm 0.29$	$5760 \pm 250$			
Others	$0.28 \pm 0.10$	$2900 \pm 500$			
W' SSM (3 TeV)	$82 \pm 24$	$530 \pm 40$			
W' SSM (5 TeV)	$3.6 \pm 0.6$	$13.8 \pm 1.0$			
Total background	$1.5 \pm 0.5$	$18400 \pm 1900$			

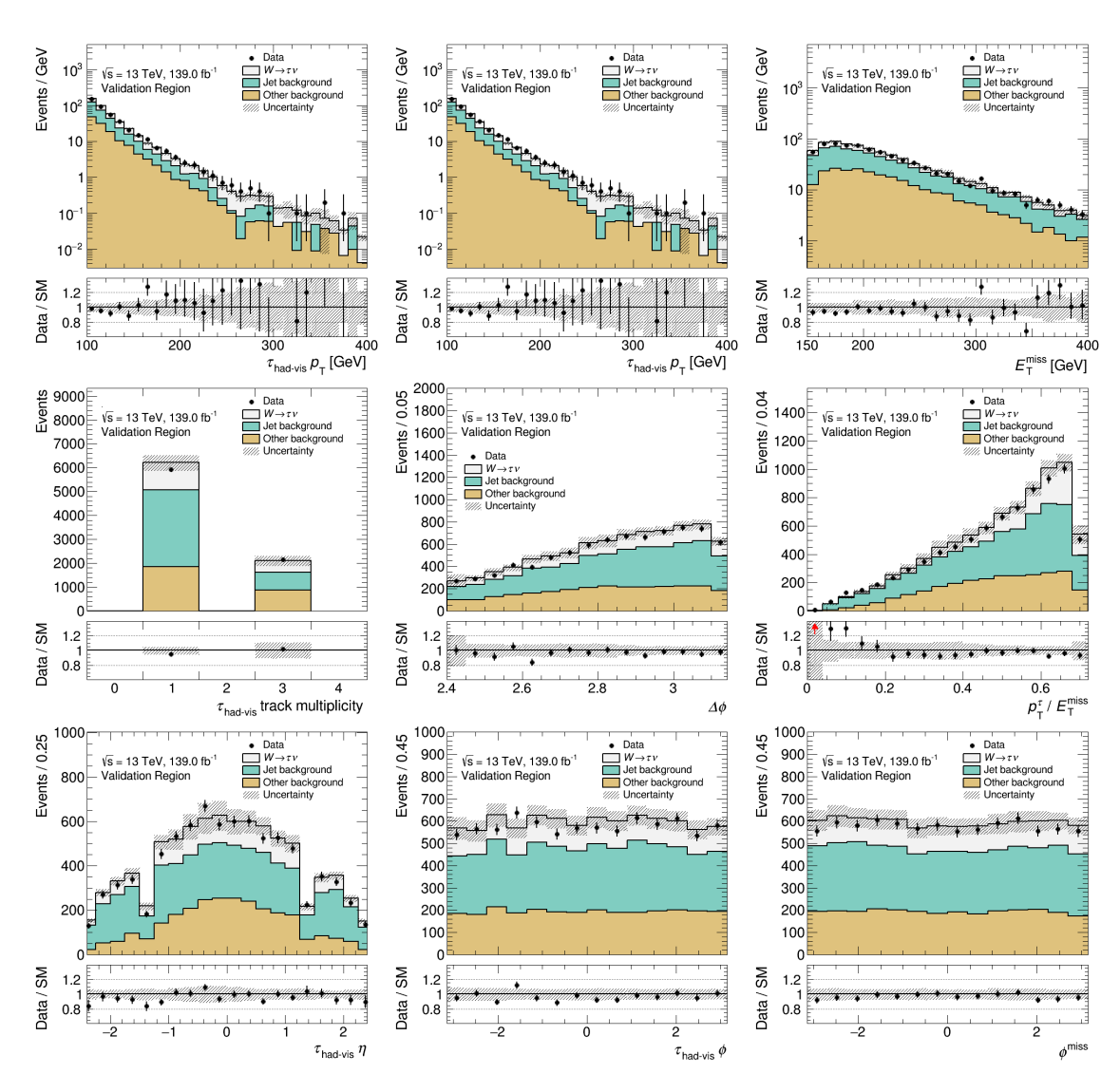


Figure 43: Post-fit distributions in the alternative validation region for data collected in the years 2015-2018. There is a good agreement between data and expected background estimate. The shown uncertainties correspond to the combined statistical and systematic uncertainties.

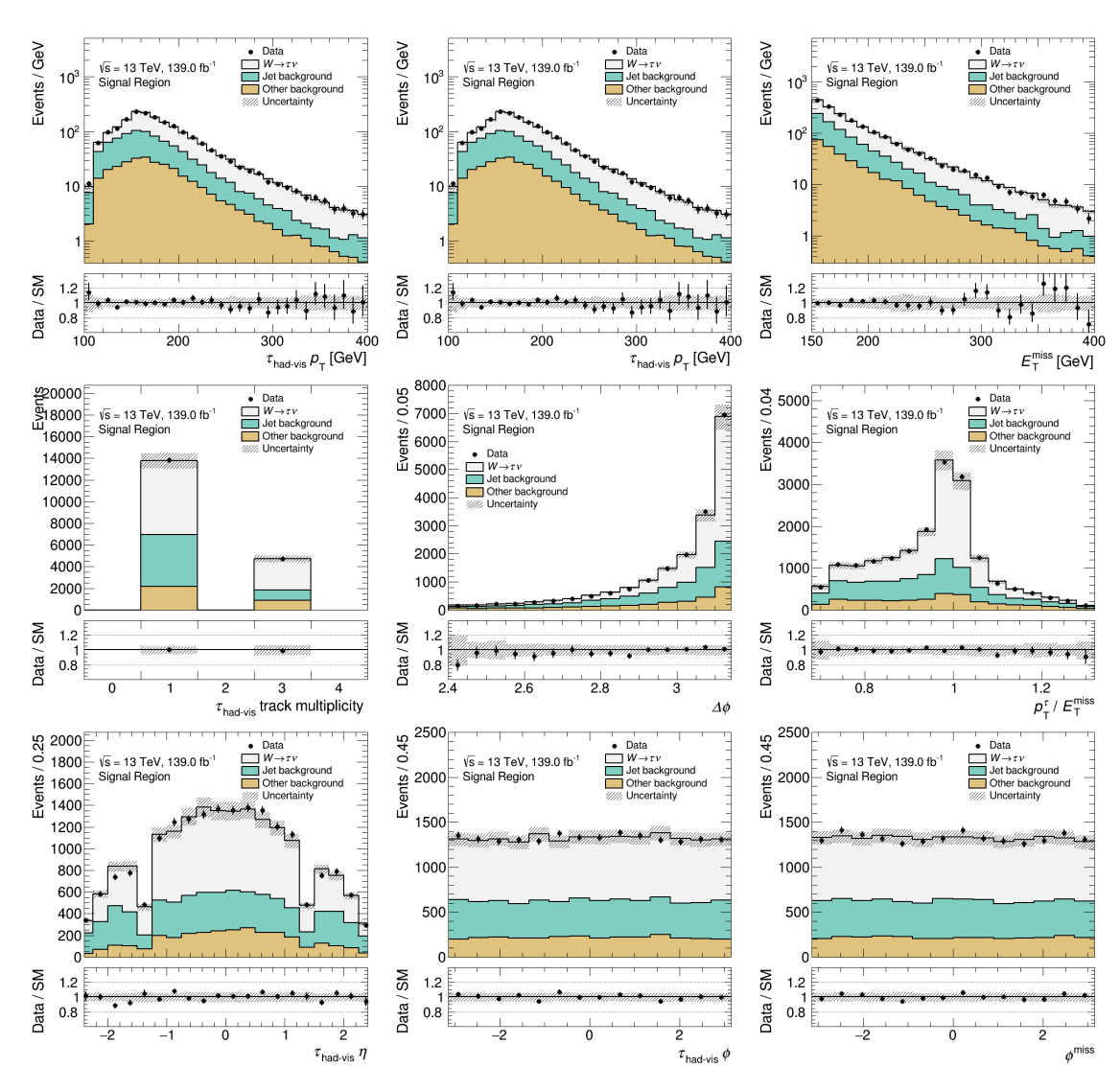


Figure 44: Post-fit distributions in the signal region for data collected in the years 2015-2018. There is a good agreement between data and expected background estimate. The shown uncertainties correspond to the combined statistical and systematic uncertainties.

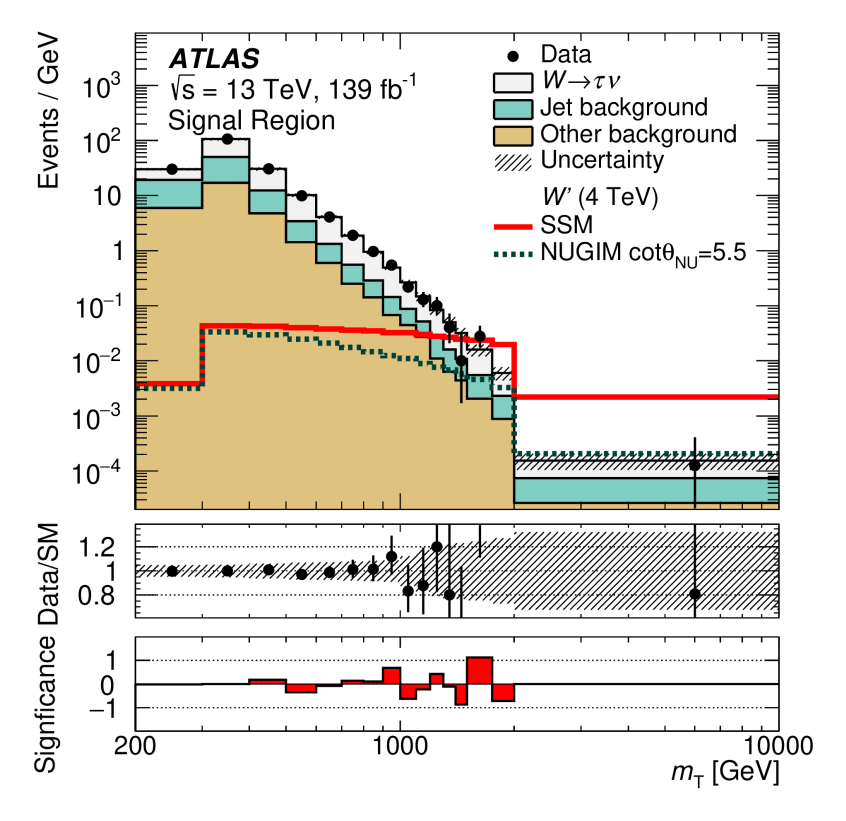


Figure 45: The post-fit distribution of the  $m_{\rm T}$ , in the SR after the likelihood fit to data under the background-only hypothesis. The uncertainty band (hatched) shows the combined statistical and systematic uncertainty. The  $m_{\rm T}$  distributions of a W' signal with mass of 4 TeV within the SSM (red solid line) and NUGIM with cot  $\theta_{\rm NU} = 5.5$  (dark green dotted line) hypotheses are overlaid. The significance of the data given the SM expectation and its uncertainty is given in the lower panel.

#### 6.2.2 Limits on Sequential Standard Model

As discussed in Sec. 6.2.1, no significant deviation from the SM expectation is observed. Consequently, upper limits at 95% CL are derived for the cross-section times branching ratios of the different signal mass hypotheses,  $\sigma \cdot B \equiv \sigma(pp \to W' + X) \cdot B(W' \to \tau \nu)$ . The 95% upper limit on  $(\sigma \cdot B)$  is shown in Fig. 46. Based on the observed upper limits, the SSM with W' masses below 5 TeV is excluded at 95% CL by this search.

The 95% CL upper limits on  $(\sigma \cdot B)$  were obtained using asymptotic formulae. The validity of the asymptotic formulae for the low-statistics, high- $m_T$  range was verified by deriving the  $CL_s$  for signal masses above 4 TeV using pseudo-experiments. The comparison between the two methods showed that the asymptotic formulas provide adequately precise upper limits, within 10% to the upper limits from pseudo-experiments. Moreover, the quoted exclusion mass for  $W'_{SSM}$  remained unchanged.

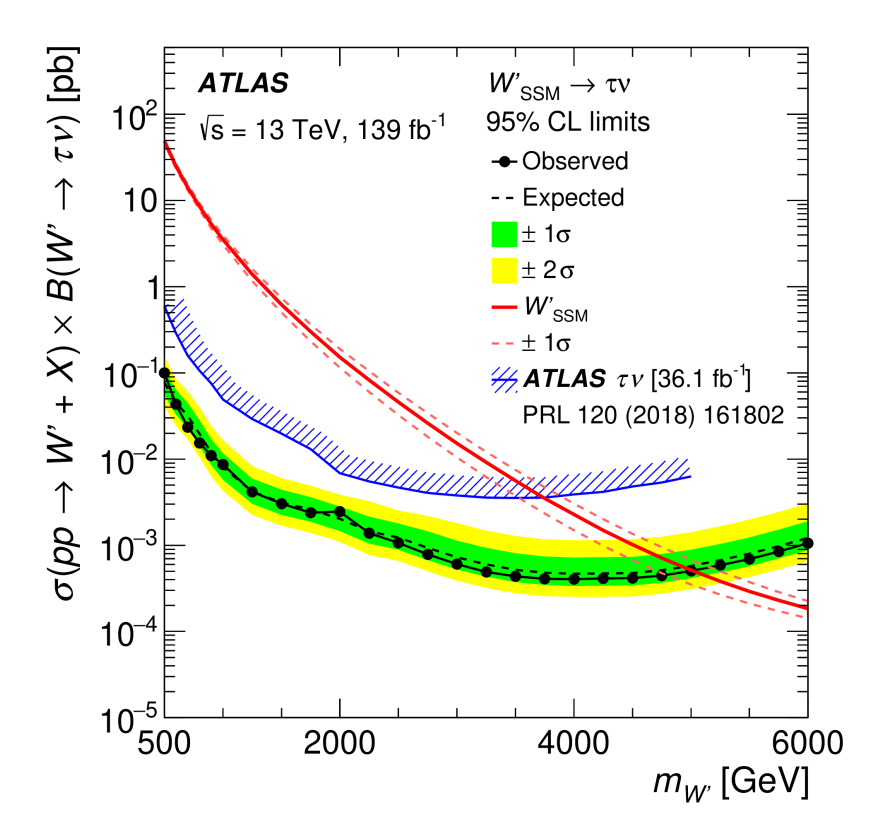


Figure 46: Observed (black markers) and expected (black dashed line) 95% CL upper limits on the cross-section times branching ratio  $(\sigma \cdot B)$  as a function of the W' mass in the SSM. The inner and outer bands show the  $N=\pm 1$  and  $\pm 2$  standard deviations, respectively, of the expected limit. The solid red line represents the SSM signals' predicted cross-section and the dashed red lines represent its theoretical uncertainty. The blue hatched line indicates the observed 95% CL upper limits on  $\sigma \cdot B$  of the previous ATLAS  $W' \to \tau \nu$  search based on 36.1 fb<sup>-1</sup> integrated luminosity.

#### 6.2.3 Limits on Non-Universal Gauge Interaction Models

This search also looked for signal hypotheses with preferential couplings to the third generation of fermions. A set of  $\cot\theta_{\rm NU}$  values in the range of  $1<\cot\theta_{\rm NU}<5.5$  was scanned, and 95% CL upper limits on each individual  $(\sigma\cdot B)$  were derived. The 95% CL upper limits on  $(\sigma\cdot B)$  for each value of  $\cot\theta_{\rm NU}$  are shown in Fig. 47. The available phase-space of the TopFlavor models of Ref. [43] is also overlaid on the plot. The results of this search exclude the studied TopFlavor models for W' masses below approximately 2 TeV at 95% CL, regardless of the W' couplings. Additionally, a large fraction of the phase space for W' is excluded, for W' masses between 2 TeV and 5.5 TeV. A large fraction of NUGIM models, mainly with large signal widths that exist in the lowest end of the shaded region, remains viable, as they are not excluded by this search. The same plot shows the impact of resonance width on the experimental results, which can become significant for larger widths. For this reason, direct comparisons of such models'  $(\sigma\cdot B)$  with the SSM upper limits generally provide less conservative limits on the W' masses. As an example, the regions with the lowest  $\sigma\cdot B$  in the Top Flavor model correspond to very large-width resonances. A direct comparison of such models with the SSM (with  $\cot\theta_{\rm NU}=1.0$ ) excludes W' masses up to 1.8 TeV. In contrast, a comparison with the

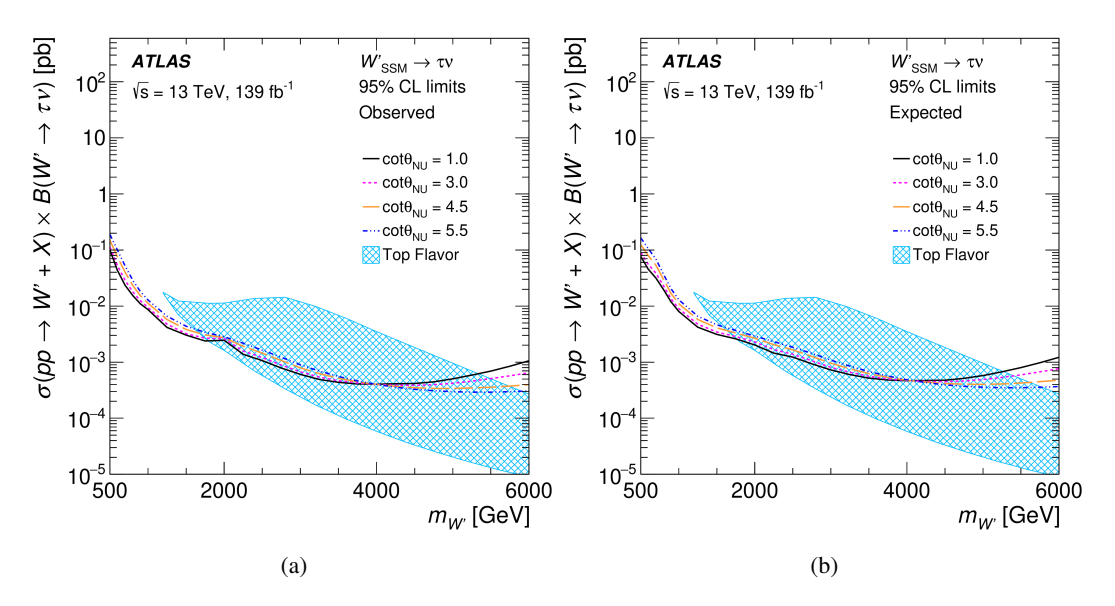


Figure 47: (a) Observed and (b) expected 95% CL upper limits on the  $(\sigma \cdot B)$  as a function of the W' mass in several NUGIM models defined by the value of the parameter  $\cot \theta_{\text{NU}}$ . The dashed lines illustrate the available phase space as predicted by the TopFlavor model of Ref. [43].

limits obtained by the NUGIM model (with  $\cot \theta_{\text{NU}} = 5.5$ ) excludes W' masses up to 1.6 TeV.

The derived excluded NUGIM signal mass exclusions are shown in the plane of  $(\cot \theta_{\text{NU}}, M_W')$  in Fig. 48. These results of this search cover an important region of the available phase space on this plane  $(\cot \theta_{\text{NU}} \ge 1.6)$ , as demonstrated by the comparison with other direct and indirect searches for new heavy gauge bosons in the same figure.

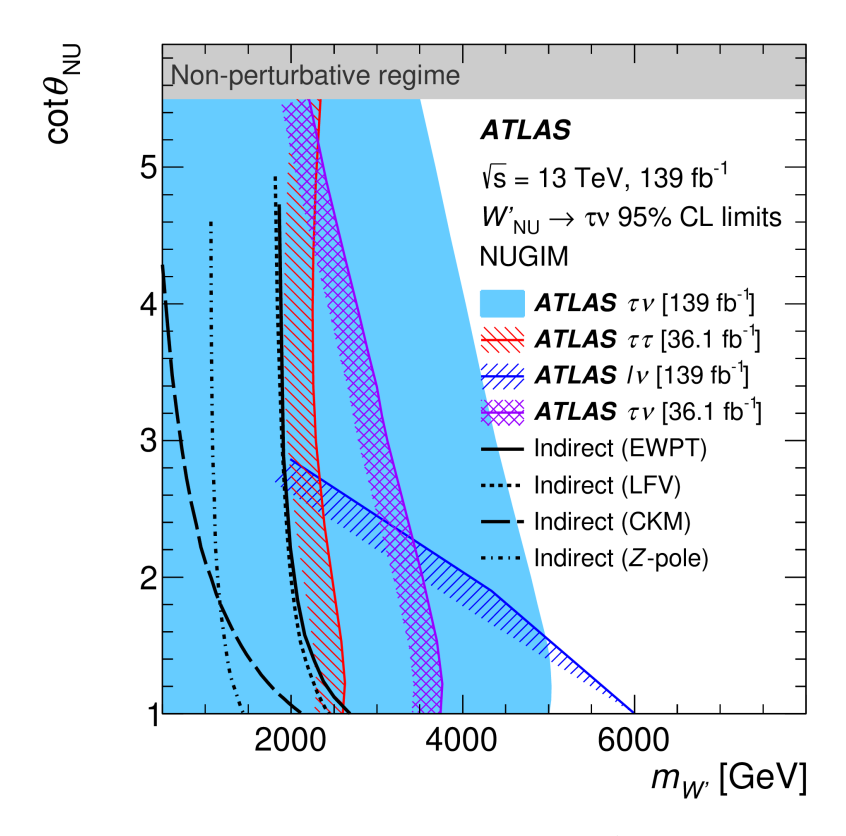


Figure 48: Observed 95% CL lower limit on the NUGIM models' W' mass as a function of the parameter  $\cot\theta_{\rm NU}$ . The blue shaded area represents the exclusion limits set by this search. For the same data sample, the exclusion limits set by the  $W' \to \ell \nu$  search [48] are also shown as blue forward hatched line. The observed limits from the ATLAS 36.1 fb<sup>-1</sup> searches for  $W' \to \tau \nu$  [49] (purple diagonal crosses) and  $Z' \to \tau \tau$  [85] (red backward hatched line) are overlaid for comparison. For this illustration, the W' and Z' bosons are assumed to be degenerate in mass. Indirect limits at 95% CL from EWPT [56], LFV [57], CKM unitarity [58] and the Z-pole data [39] are also overlaid.

## 6.3 Model independent limits

In addition to the model-dependent limits, which assume a specific signal model, this search also derived results for model-independent upper limits. These limits do not rely on a particular signal hypothesis, offering a broader constraint on potential new models that contain a  $\tau_{\text{had-vis}} + E_{\text{T}}^{\text{miss}}$  final state.

In order to derive upper limits in a model-independent way, a lower threshold on the transverse mass,  $m_{\rm T}^{\rm thresh}$ , is employed, and the visible cross section above this threshold is measured. The visible cross section is defined as:

$$\sigma_{\text{vis}} = \sigma \cdot B \cdot \mathcal{A} \cdot \varepsilon \equiv \frac{N_{\text{sig}}}{L} \tag{6.15}$$

where  $\mathcal{A}$  is the model's acceptance,  $\varepsilon$  is the efficiency, and  $N_{\text{sig}}$  and L are the signal yields and integrated luminosity, respectively.

The advantage of using a cut-and-count approach, with thresholds on  $m_{\rm T}$ , is that different new physics models can predict different signal shapes for the  $m_{\rm T}$  distribution. By applying the  $m_{\rm T}^{\rm thresh}$ , one can integrate out the acceptance of their model and the efficiency to determine the total cross section above a given  $m_{\rm T}^{\rm thresh}$ . If the model's cross section above the  $m_{\rm T}^{\rm thresh}$  exceeds the reported upper limits, the model is excluded at 95% CL by this analysis.

Figure 49 compares the generated  $m_{\rm T}$  distributions for SSM signals after applying the full event selection at generator and reconstruction level. The agreement between the high- $m_{\rm T}$  regions of these distributions suggests that the acceptance,  $\mathcal{A}$ , can be reliably determined at generator level for a given  $m_{\rm T}$  threshold. The same figure shows the efficiency  $\varepsilon$ , which is defined as:

$$\varepsilon = \frac{m_{\text{T (generated -- reco-selections)}}}{m_{\text{T (generated -- generated-selections)}}}$$
(6.16)

where  $m_{\rm T\,(generated\,-\,reco-selections)}$  is the  $m_{\rm T}$  distribution at generator-level after the events pass the reconstruction-level requirements, and  $m_{\rm T\,(generated\,-\,generated-selections)}$  is the  $m_{\rm T}$  distribution at generator-level after the events pass the requirements at generator-level. A third-degree polynomial was used to fit the calculated efficiencies, and two approaches were tested:

- Approach A: Fitting the polynomial to the efficiencies derived from a flat W' signal sample.
- **Approach B**: Fitting the polynomial to the weighted average of the efficiencies from multiple W' signal mass hypotheses.

The results from both approaches were consistent, with deviations within an absolute difference of  $\Delta \varepsilon = 0.1$ . **Approach A** was chosen as the nominal method, as it does not rely on specific signal mass considerations, thus providing a more model-independent estimation of the efficiency. The fitted efficiency is:

$$\varepsilon^{\text{fit-flat}}(m_{\text{T}}) = 0.8143(26) - 0.3094(39) \cdot m_{\text{T}}[\text{TeV}] + 0.0863(13) \cdot m_{\text{T}}^2[\text{TeV}] - 0.00545(11) \cdot m_{\text{T}}^3[\text{TeV}]$$
(6.17)

The efficiency increases for transverse masses above 4 TeV, mainly due to the application of correction factors that account for the simulation of the tau-lepton hits in the inner detector. This

effect is mainly due to an increased fraction of reconstructed 1-prong events at high  $m_{\rm T}$ , caused by the migration of 0-prong and 3-prong  $\tau$  decays to 1-prong.

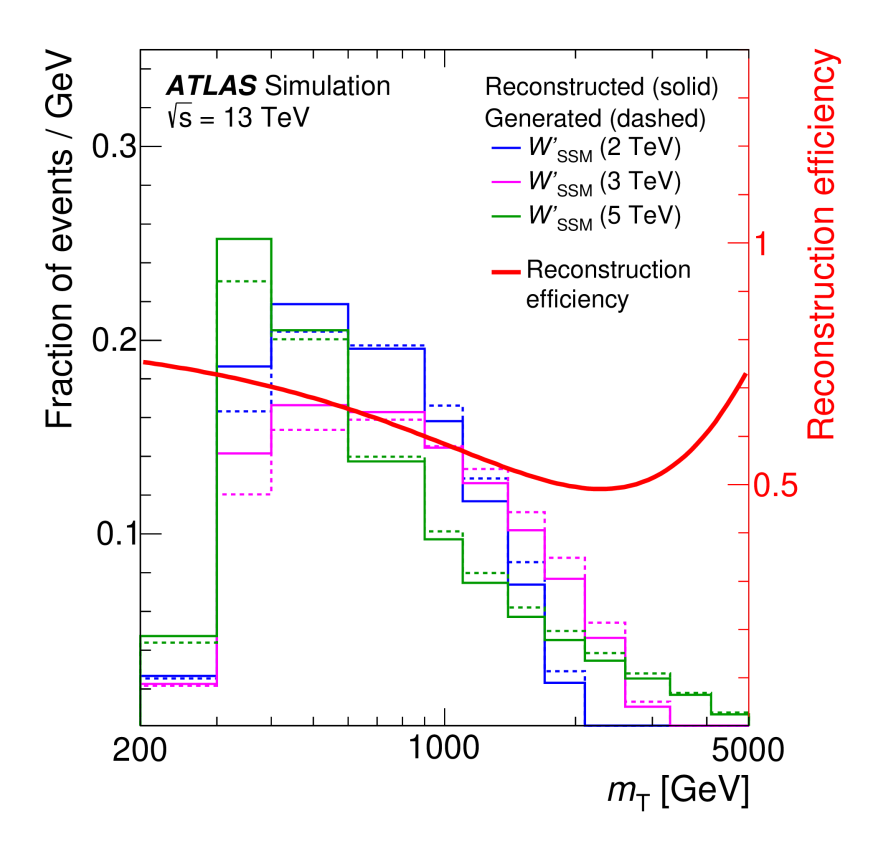


Figure 49: Comparison between the generated  $m_{\rm T}$  passing the selections at reconstruction-level (solid) and generator-level (dashed) for three SSM signal hypotheses of 2, 3 and 5 TeV in blue, purple and green lines respectively. The red line shows the efficiency of Eq. 6.17.

The yields of SM background and data events above each  $m_{\rm T}^{\rm thresh}$  are shown in Fig. 50. To obtain the upper limits, we perform a search for signal excess in each bin of the histogram independently. The limit calculation relies on determining the upper limit of the  $N_{\rm sig}$  and translating this to the visible cross section by scaling with the luminosity. To avoid issues encountered due to the use of asymptotic formulae at high- $m_{\rm T}^{\rm thresh}$ , where the observed/expected yields are low, the upper limits for  $m_{\rm T}^{\rm thresh}$  above 1.5 TeV are derived from pseudo-experiments.

Figure 51 shows the overlaid 95% upper limit on  $N_{\rm sig}$  and its error bands as obtained by the asymptotic formula method and the pseudo-experiments method. No significant deviation is seen between the results of the two methods in the intermediate range of  $m_{\rm T}^{\rm thresh}$ . However, the the asymptotic formula method led to fit problems for  $m_{\rm T}^{\rm thresh}$  above 2.1 TeV, due to the small number of events. The final 95% upper limits on  $N_{\rm sig}$  are determined by combining the results from both methods at  $m_{\rm T}^{\rm thresh}$ =1.5 TeV, where the data and SM background yields drop below 8 and 9.7 events, respectively. The 95% upper limits on the signal yields can be translated to upper limits on  $\sigma_{\rm vis}$ .

The 95% upper limits on  $\sigma_{\text{vis}}$  are shown in Fig. 52. The sudden drop near  $m_{\text{T}}^{\text{thresh}}$  of 1.5 TeV-1.6 TeV in the observed limit is a result of faster drop of data events above those thresholds.

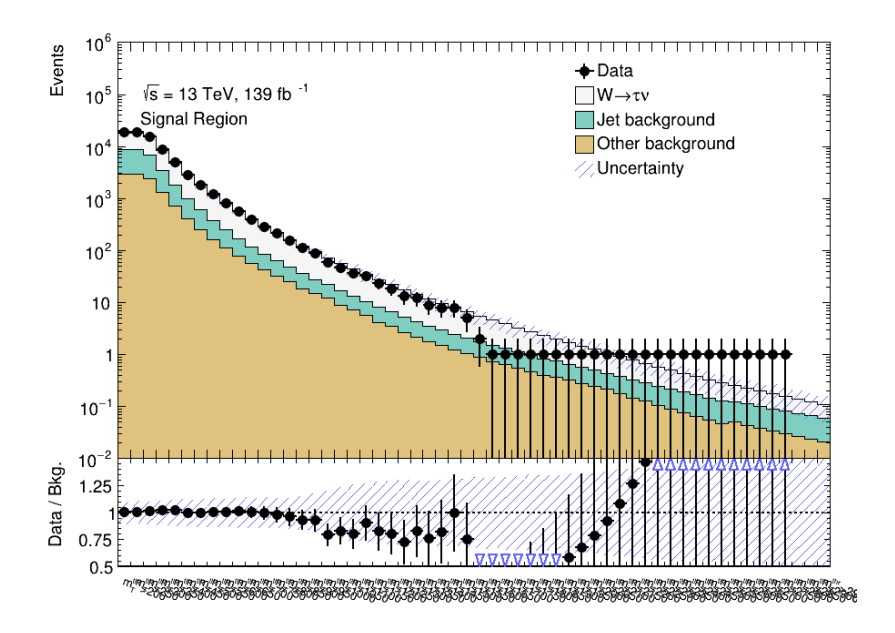


Figure 50: The observed events and SM background expected yields above each  $m_{\rm T}^{\rm thresh}$  from 200 GeV up to 2 950 GeV (in steps of 50 GeV).

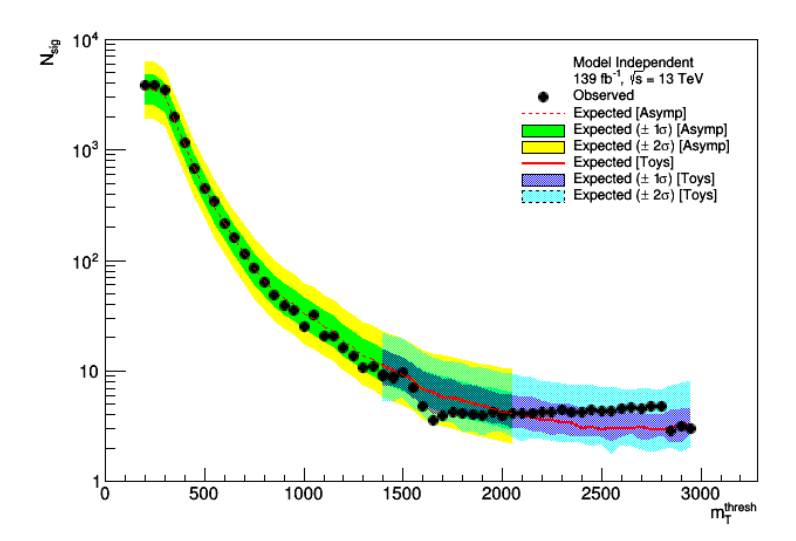


Figure 51: The 95% CL upper limits on the possible signal yields  $N_{\rm sig}$  as a function of the  $m_{\rm T}^{\rm thresh}$ . The observed upper limits are shown as data points. The results obtained from asymptotic formulae are shown in dashed red line (expected) with the green/yellow scheme for the  $\pm 1/2\sigma$  error bands. The results obtained from toys are shown in solid red line (expected) with the blue/cyan scheme for the  $\pm 1/2\sigma$  error bands. In the intermediate range of 1.4 TeV to 2.05 TeV there is a good agreement between the two methods.

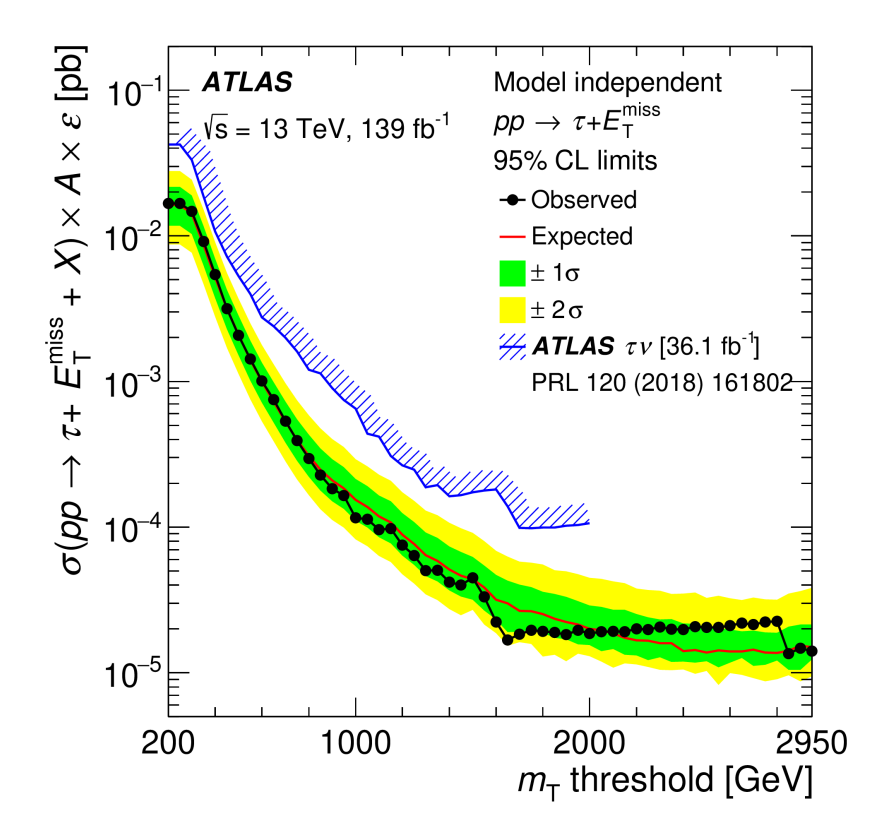


Figure 52: Model-independent 95% CL upper limits on the visible cross-section as a function of the transverse mass thresholds,  $m_{\rm T}^{\rm thresh}$ . The blue hatched line shows the observed 95% CL upper limits on the  $\sigma_{\rm vis}$  of the previous ATLAS  $W' \to \tau \nu$  [49] search. The steps in the observed upper limit at  $m_{\rm T}^{\rm thresh}$  of 1.6 and 2.85 TeV result of the discrete nature of the data and that the highest  $m_{\rm T}$  event in data appeared with  $m_{\rm T}$  =2.83 TeV.

## **Conclusions**

This thesis presented a search for  $W' \to \tau \nu$  decays using 139 fb<sup>-1</sup> of pp-collision data at center-of-mass energy of  $\sqrt{s}$  =13 TeV, recorded with the ATLAS detector at LHC. This analysis only considered decays of tau-leptons into hadrons. Such searches are motivated by new physics scenarios that violate the lepton universality by introducing gauge sectors with preferential couplings to the third generation of fermions. These models can either provide a dynamical explanation to the high-mass of the top-quark, or they can explain the deviations observed in rare B-meson semi-leptonic decays to tau leptons [97, 98, 99, 100, 101, 102, 103, 104, 105, 106].

The search relied on the transverse mass as a sensitive variable. A maximum likelihood fit was performed to compare the Standard Model expectation against the data, with no significant deviation observed. Consequently, 95% CL upper limits were set on the cross-section times branching ratio for various signal hypotheses, leading to the rejection of and various signal models. For the Sequential Standard Model, this search excluded at 95% CL the signal models up to masses of 5 TeV (4.9 TeV) in data (expectation), improving the reach of the previous ATLAS search using 36.1 fb<sup>-1</sup> by 1.3 TeV. Similarily, upper limits on the cross section times branching ratio for models with non-universal couplings were considered. Depending on the model parameters, the NUGIM models were excluded for masses less than 3.5 – 5.0 TeV at 95% CL. Finally upper limits at 95% CL on the visible production cross-section for  $\tau_{\text{had-vis}} + E_{\text{T}}^{\text{miss}}$  were derived. These limits were derived as a function of lower-thresholds on the  $m_{\text{T}}$ , using a cut-and-count approach. Signals with similar final state to this analysis and with visible cross-section above 17 fb to 0.014 fb (depending on the  $m_{\text{T}}$  threshold) are excluded at 95% CL.

The improvements in exclusion limits originate from several factors, including the increased dataset size, improved tau reconstruction and identification through multivariate techniques such as the RNN, and the multi-bin fitting approach to the  $m_{\rm T}$  distribution.

Future searches for high-mass signals can benefit from increased statistics, achievable with the ATLAS Run-3 dataset, expected to reach an integrated luminosity of  $300\,\mathrm{fb}^{-1}$ . Additional improvements in the identification of the core tracks of the  $\tau_{\mathrm{had-vis}}$  during reconstruction could further enhance sensitivity to high-mass signals. Finally, exploring alternative production modes and final states, such as  $qg \to bW'(\to \tau \nu)$ , remains a theoretically motivated avenue for further study.

# **Bibliography**

- [1] S. Navas et al., *Review of Particle Physics*, Phys. Rev. D **110** (3 2024) 030001, URL: https://link.aps.org/doi/10.1103/PhysRevD.110.030001.
- [2] http://cern-accelerators-optics.web.cern.ch/.
- [3] O. S. Brüning et al., *LHC Design Report*, CERN Yellow Reports: Monographs, CERN, 2004, URL: https://cds.cern.ch/record/782076.
- [4] G. Avoni et al.,

  The new LUCID-2 detector for luminosity measurement and monitoring in ATLAS,

  JINST 13 (2018) P07017.
- [5] R. Steerenberg et al., "Operation and performance of the CERN Large Hadron Collider during proton Run 2", 10th International Particle Accelerator Conference, 2019 MOPMP031.
- [6] T. A. Collaboration, *The ATLAS Experiment at the CERN Large Hadron Collider*, Journal of Instrumentation **3** (2008) S08003, URL: https://doi.org/10.1088%2F1748-0221%2F3%2F08%2Fs08003.
- [7] N. Ilic, Observation of the Higgs Boson Decaying to WW to leptons and neutrinos, Presented 15 Feb 2015, 2015, URL: https://cds.cern.ch/record/2257245.
- [8] M. Aaboud et al., Study of the material of the ATLAS inner detector for Run 2 of the LHC, Journal of Instrumentation 12 (2017) P12009, ISSN: 1748-0221, URL: http://dx.doi.org/10.1088/1748-0221/12/P12009.
- [9] Track Reconstruction Performance of the ATLAS Inner Detector at  $\sqrt{s} = 13$  TeV, tech. rep. ATL-PHYS-PUB-2015-018, CERN, 2015, URL: http://cds.cern.ch/record/2037683.
- [10] T. Saleem, Development of pixel detector for ATLAS Inner Tracker(ITK) upgrade at HL-LHC and Searching for the Standard Model Higgs boson decay into b-quark pair with ATLAS experiment, Theses: Université Paris Saclay (COmUE), 2019, URL: https://tel.archives-ouvertes.fr/tel-02275808.
- [11] J. Pequenao, "Computer Generated image of the ATLAS calorimeter", 2008, URL: https://cds.cern.ch/record/1095927.
- [12] G. e. a. Aad, Performance of the missing transverse momentum triggers for the ATLAS detector during Run-2 data taking, z 2020 (2020) 80, ISSN: 1029-8479, URL: https://doi.org/10.1007/JHEP08(2020)080.

- [13] M. Aaboud et al., *Performance of the ATLAS track reconstruction algorithms in dense environments in LHC Run* 2, The European Physical Journal C **77** (2017) 673, ISSN: 1434-6052, URL: https://doi.org/10.1140/epjc/s10052-017-5225-7.
- [14] G. Aad et al., Muon reconstruction performance of the ATLAS detector in proton–proton collision data at  $\sqrt{s} = 13$  TeV, Eur. Phys. J. C **76** (2016) 292, arXiv: 1603.05598 [hep-ex].
- [15] M. Aaboud et al., Electron reconstruction and identification in the ATLAS experiment using the 2015 and 2016 LHC proton-proton collision data at  $\sqrt{s} = 13$  TeV, Eur. Phys. J. C **79** (2019) 639, arXiv: 1902.04655 [physics.ins-det].
- [16] M. Cacciari, G. P. Salam and G. Soyez, *The anti-k<sub>t</sub> jet clustering algorithm*, JHEP **04** (2008) 063, arXiv: 0802.1189 [hep-ph].
- [17] G. Aad et al.,

  Topological cell clustering in the ATLAS calorimeters and its performance in LHC Run 1.

  Topological cell clustering in the ATLAS calorimeters and its performance in LHC Run 1,

  Eur. Phys. J. C 77 (2016) 490. 87 p, url: https://cds.cern.ch/record/2138166.
- [18] ATLAS Collaboration, *Performance of pile-up mitigation techniques for jets in pp collisions* at  $\sqrt{s} = 8$  TeV using the ATLAS detector, Eur. Phys. J. C **76** (2016) 581, arXiv: 1510.03823 [hep-ex].
- [19] ATLAS Collaboration,

  Identification and rejection of pile-up jets at high pseudorapidity with the ATLAS detector,

  Eur. Phys. J. C 77 (2017) 580, arXiv: 1705.02211 [hep-ex],

  Erratum: Eur. Phys. J. C 77 (2017) 712.
- [20] M. Aaboud et al., Jet energy scale measurements and their systematic uncertainties in proton-proton collisions at  $\sqrt{s} = 13$  TeV with the ATLAS detector, Phys. Rev. D **96** (2017) 072002, arXiv: 1703.09665 [hep-ex].
- [21] Selection of jets produced in 13TeV proton-proton collisions with the ATLAS detector, tech. rep. ATLAS-CONF-2015-029, CERN, 2015, URL: https://cds.cern.ch/record/2037702.
- [22] Measurement of the tau lepton reconstruction and identification performance in the ATLAS experiment using pp collisions at  $\sqrt{s} = 13$  TeV, tech. rep. ATLAS-CONF-2017-029, CERN, 2017, URL: https://cds.cern.ch/record/2261772.
- [23] Identification of hadronic tau lepton decays using neural networks in the ATLAS experiment, tech. rep. ATL-PHYS-PUB-2019-033, CERN, 2019, URL: https://cds.cern.ch/record/2688062.
- [24] A. Hrynevich,

  ATLAS jet and missing energy reconstruction, calibration and performance in LHC Run-2, tech. rep. ATL-PHYS-PROC-2017-045. 06, CERN, 2017,

  URL: https://cds.cern.ch/record/2263777.
- [25] M. Aaboud et al.,

  Identification and rejection of pile-up jets at high pseudorapidity with the ATLAS detector,

  Eur. Phys. J. C 77 (2017) 580, [Erratum: Eur.Phys.J.C 77, 712 (2017)],

  arXiv: 1705.02211 [hep-ex].

- [26] M. Cacciari and G. P. Salam, *Pileup subtraction using jet areas*, Phys. Lett. B **659** (2008) 119, arXiv: 0707.1378 [hep-ph].
- [27] Y. L. Dokshitzer, Calculation of the Structure Functions for Deep Inelastic Scattering and e+ e- Annihilation by Perturbation Theory in Quantum Chromodynamics, Sov. Phys. JETP **46** (1977) 641, [Zh. Eksp. Teor. Fiz. 73, 1216 (1977)].
- [28] V. N. Gribov and L. N. Lipatov, *Deep inelastic e p scattering in perturbation theory*, Sov. J. Nucl. Phys. **15** (1972) 438, [Yad. Fiz. 15, 781 (1972)].
- [29] G. Altarelli and G. Parisi, *Asymptotic Freedom in Parton Language*, Nucl. Phys. B **126** (1977) 298.
- [30] L. Del Debbio, *Parton distributions in the LHC era*, EPJ Web of Conferences **175** (2018) 01006.
- [31] K. Nakamura and S. Petcov, *Neutrino Masses, Mixing, and Oscillations*, Progress of Theoretical and Experimental Physics **2020** (2020) 083C01, Review of Particle Physics.
- [32] S. Chang and J. G. Wacker, Little Higgs models and custodial SU(2), Phys. Rev. D 69 (3 2004) 035002, URL: https://link.aps.org/doi/10.1103/PhysRevD.69.035002.
- [33] T. Li et al.,

  Charged lepton flavor violation in light of the muon magnetic moment anomaly and colliders,

  The European Physical Journal C 81 (2021), ISSN: 1434-6052,

  URL: http://dx.doi.org/10.1140/epjc/s10052-021-09569-9.
- [34] W. Altmannshofer et al.,

  Lepton flavor violating Z explanation of the muon anomalous magnetic moment,

  Physics Letters B 762 (2016) 389, ISSN: 0370-2693,

  URL: http://dx.doi.org/10.1016/j.physletb.2016.09.046.
- [35] R. Cheaib, *Overview of R(D) and R(D\*)*, 2022, arXiv: 2207.14146 [hep-ex], URL: https://arxiv.org/abs/2207.14146.
- [36] J. A. A. et al. (Particle Data Group), *Review of Particle Physics*, Phys. Rev. D **98** (2018) 030001.
- [37] R. Aaij et al., *Measurement of matter-antimatter differences in beauty baryon decays*, Nature Phys. **13** (2017) 391, arXiv: 1609.05216 [hep-ex].
- [38] P. Roy and M. D. L. de Moura,

  Left-Right Symmetric Models and the Matter-Antimatter Asymmetry,

  Advances in High Energy Physics 2014 (2014) Article ID 264201.
- [39] E. Malkawi, T. Tait and C.-P. Yuan, *A model of strong flavor dynamics for the top quark*, Phys. Lett. B **385** (1996) 304, arXiv: hep-ph/9603349.
- [40] D. J. Muller and S. Nandi, *Top flavor: a separate SU(2) for the third family*, Phys. Lett. B **383** (1996) 345, arXiv: hep-ph/9602390.
- [41] K. Hsieh et al., Global analysis of general  $SU(2) \times SU(2) \times U(1)$  models with precision data, Phys. Rev. D **82** (2010) 035011, arXiv: 1003.3482 [hep-ph].

- [42] C.-W. Chiang et al., Family  $SU(2)_l \times SU(2)_h \times U(1)$  Model, Phys. Rev. D **81** (2010) 015006, arXiv: 0911.1480 [hep-ph].
- [43] R. Calabrese et al., *Top-flavor scheme in the context of W' searches at LHC*, Phys. Rev. D **104** (2021) 055006, arXiv: 2104.06720 [hep-ph].
- [44] G. Senjanovic and R. N. Mohapatra, *Exact Left-Right Symmetry and the Weak Interaction*, Phys. Rev. D **12** (1975) 1502.
- [45] H. Georgi, J. W. Ng and J. P. Silva, *Little Higgs*, Phys. Rev. D **63** (2001) 035007.
- [46] G. Altarelli, B. Mele and M. Ruiz-Altaba,
  Searching for New Heavy Vector Bosons in pp̄ Colliders,
  Z. Phys. C 45 (1989) 109, [Erratum: Z.Phys.C 47, 676 (1990)].
- [47] P. D. Group, W'-Boson Searches,
  Progress of Theoretical and Experimental Physics 2023 (2023) 083C01,
  https://pdg.lbl.gov/2023/reviews/rpp2023-rev-wprime-searches.pdf.
- [48] ATLAS Collaboration, Search for a heavy charged boson in events with a charged lepton and missing transverse momentum from pp collisions at  $\sqrt{s} = 13$  TeV with the ATLAS detector, Phys. Rev. D **100** (2019) 052013, arXiv: 1906.05609 [hep-ex].
- [49] ATLAS Collaboration, Search for High-Mass Resonances Decaying to  $\tau v$  in pp Collisions at  $\sqrt{s} = 13$  TeV with the ATLAS detector, Phys. Rev. Lett. **120** (2018) 161802, arXiv: 1801.06992 [hep-ex].
- [50] CMS Collaboration, Search for new physics in the  $\tau$  lepton plus missing transverse momentum final state in proton-proton collisions at  $\sqrt{s} = 13$  TeV, JHEP **09** (2023) 051, arXiv: 2212.12604 [hep-ex].
- [51] Erdweg, Sören, *Study for Sensitivity for W' to τνwithCMS*, Available at: https://cds.cern.ch/record/2285844, PhD thesis: RWTH Aachen University, 2011.
- [52] G. Aad et al., Search for vector-boson resonances decaying into a top quark and a bottom quark using pp collisions at  $\sqrt{s} = 13$  TeV with the ATLAS detector, JHEP 12 (2023) 073, arXiv: 2308.08521 [hep-ex].
- [53] A. Hayrapetyan et al., Search for W' bosons decaying to a top and a bottom quark in leptonic final states in proton-proton collisions at  $\sqrt{s} = 13$  TeV, JHEP **05** (2024) 046, arXiv: 2310.19893 [hep-ex].
- [54] G. Aad et al., Search for new resonances in mass distributions of jet pairs using  $139 \text{ fb}^{-1}$  of pp collisions at  $\sqrt{s} = 13 \text{ TeV}$  with the ATLAS detector, JHEP **03** (2020) 145, arXiv: 1910.08447 [hep-ex].
- [55] A. M. Sirunyan et al., Search for high mass dijet resonances with a new background prediction method in proton-proton collisions at  $\sqrt{s} = 13$  TeV, JHEP **05** (2020) 033, arXiv: 1911.03947 [hep-ex].
- [56] Q.-H. Cao et al., Discovery and identification of W' and Z' in  $SU(2)_1 \otimes SU(2)_2 \otimes U(1)_X$  models at the LHC, Phys. Rev. D **86** (2012) 095010, arXiv: 1205.3769 [hep-ph].

- [57] K. Y. Lee, Lepton flavor violation in a nonuniversal gauge interaction model, Phys. Rev. D **82** (2010) 097701, arXiv: 1009.0104 [hep-ph].
- [58] K. Y. Lee, *Unitarity violation of the CKM matrix in a nonuniversal gauge interaction model*, Phys. Rev. D **71** (2005) 115008, arXiv: hep-ph/0410381.
- [59] B. R. Webber, A QCD Model for Jet Fragmentation Including Soft Gluon Interference, Nucl. Phys. B 238 (1984) 492.
- [60] B. Andersson et al., Parton Fragmentation and String Dynamics, Phys. Rept. 97 (1983) 31.
- [61] S. Agostinelli et al., GEANT4 a simulation toolkit, Nucl. Instrum. Meth. A 506 (2003) 250.
- [62] ATLAS Collaboration, *The ATLAS Simulation Infrastructure*, Eur. Phys. J. C **70** (2010) 823, arXiv: 1005.4568 [physics.ins-det].
- [63] P. Nason, A new method for combining NLO QCD with shower Monte Carlo algorithms, JHEP 11 (2004) 040, arXiv: hep-ph/0409146.
- [64] S. Frixione, P. Nason and C. Oleari, Matching NLO QCD computations with parton shower simulations: the POWHEG method, JHEP 11 (2007) 070, arXiv: 0709.2092 [hep-ph].
- [65] S. Alioli et al., A general framework for implementing NLO calculations in shower Monte Carlo programs: the POWHEG BOX, JHEP 06 (2010) 043, arXiv: 1002.2581 [hep-ph].
- [66] S. Alioli et al., *NLO vector-boson production matched with shower in POWHEG*, JHEP **07** (2008) 060, arXiv: 0805.4802 [hep-ph].
- [67] H.-L. Lai et al., *New parton distributions for collider physics*, Phys. Rev. D **82** (2010) 074024, arXiv: 1007.2241 [hep-ph].
- [68] ATLAS Collaboration, Measurement of the  $Z/\gamma^*$  boson transverse momentum distribution in pp collisions at  $\sqrt{s} = 7$  TeV with the ATLAS detector, JHEP **09** (2014) 145, arXiv: 1406.3660 [hep-ex].
- [69] J. Pumplin et al.,

  New Generation of Parton Distributions with Uncertainties from Global QCD Analysis,

  JHEP 07 (2002) 012, arXiv: hep-ph/0201195.
- [70] S. Frixione, G. Ridolfi and P. Nason,

  A positive-weight next-to-leading-order Monte Carlo for heavy flavour hadroproduction,

  JHEP 09 (2007) 126, arXiv: 0707.3088 [hep-ph].
- [71] NNPDF Collaboration, *Parton distributions for the LHC run II*, JHEP **04** (2015) 040, arXiv: 1410.8849 [hep-ph].
- [72] E. Re, Single-top Wt-channel production matched with parton showers using the POWHEG method, Eur. Phys. J. C 71 (2011) 1547, arXiv: 1009.2450 [hep-ph].
- [73] E. Bothmann et al., Event generation with Sherpa 2.2, SciPost Phys. 7 (2019) 034, arXiv: 1905.09127 [hep-ph].
- [74] S. Höche et al., *QCD matrix elements* + parton showers. The NLO case, JHEP **04** (2013) 027, arXiv: 1207.5030 [hep-ph].

- [75] T. Gleisberg and S. Höche, *Comix*, a new matrix element generator, JHEP **12** (2008) 039, arXiv: 0808.3674 [hep-ph].
- [76] S. Schumann and F. Krauss,

  A parton shower algorithm based on Catani–Seymour dipole factorisation,

  JHEP 03 (2008) 038, arXiv: 0709.1027 [hep-ph].
- [77] S. Höche et al., A critical appraisal of NLO+PS matching methods, JHEP **09** (2012) 049, arXiv: 1111.1220 [hep-ph].
- [78] S. Catani et al., *QCD Matrix Elements + Parton Showers*, JHEP **11** (2001) 063, arXiv: hep-ph/0109231.
- [79] S. Höche et al., *QCD matrix elements and truncated showers*, JHEP **05** (2009) 053, arXiv: 0903.1219 [hep-ph].
- [80] ATLAS Collaboration, *The new Fast Calorimeter Simulation in ATLAS*, ATL-SOFT-PUB-2018-002, 2018, url: https://cds.cern.ch/record/2630434.
- [81] K. Hsieh et al., *Global Analysis of General SU*(2) *x SU*(2) *x U*(1) *Models with Precision Data*, Phys. Rev. D **82** (2010) 035011, arXiv: 1003.3482 [hep-ph].
- [82] P. A. Z. et al., *Review of Particle Physics*, Prog. Theor. Exp. Phys. **2020** (2020) 083C01, Section on CKM Matrix.
- [83] G. Aad et al., A search for high-mass resonances decaying to  $\tau^+\tau^-$  in pp collisions at  $\sqrt{s} = 7$  TeV with the ATLAS detector, Phys. Lett. B **719** (2013) 242, arXiv: 1210.6604 [hep-ex].
- [84] G. Aad et al., Search for a heavy charged boson in events with a charged lepton and missing transverse momentum from pp collisions at  $\sqrt{s} = 13$  TeV with the ATLAS detector, Phys. Rev. D **100** (2019) 052013, arXiv: 1906.05609 [hep-ex].
- [85] ATLAS Collaboration, Search for additional heavy neutral Higgs and gauge bosons in the ditau final state produced in  $36 \, fb^{-1}$  of pp collisions at  $\sqrt{s} = 13 \, TeV$  with the ATLAS detector, JHEP **01** (2018) 055, arXiv: 1709.07242 [hep-ex].
- [86] ATLAS Collaboration, *Jet energy scale and resolution measured in proton–proton collisions* at  $\sqrt{s} = 13$  TeV with the ATLAS detector, Eur. Phys. J. C **81** (2021) 689, arXiv: 2007.02645 [hep-ex].
- [87] ATLAS Collaboration,  $E_T^{miss}$  performance in the ATLAS detector using 2015–2016 LHC pp collisions, ATLAS-CONF-2018-023, 2018, url: https://cds.cern.ch/record/2625233.
- [88] ATLAS Collaboration, Luminosity determination in pp collisions at  $\sqrt{s} = 13$  TeV using the ATLAS detector at the LHC, ATLAS-CONF-2019-021, 2019, URL: https://cds.cern.ch/record/2677054.
- [89] G. Aad et al., *Performance and calibration of quark/gluon-jet taggers using 140 fb*<sup>1</sup> *of pp collisions at TeV with the ATLAS detector\**, Chin. Phys. C **48** (2024) 023001, arXiv: 2308.00716 [hep-ex].
- [90] S. Dulat et al.,

  New parton distribution functions from a global analysis of quantum chromodynamics,
  Phys. Rev. D **93** (2016) 033006, arXiv: 1506.07443 [hep-ph].

- [91] ATLAS Collaboration, Precision measurement and interpretation of inclusive  $W^+$ ,  $W^-$  and  $Z/\gamma^*$  production cross sections with the ATLAS detector, Eur. Phys. J. C 77 (2017) 367, arXiv: 1612.03016 [hep-ex].
- [92] J. Butterworth, et al., *PDF4LHC recommendations for LHC Run II*, J. Phys. G **43** (2016) 023001, arXiv: hep-ph/1101.0536.
- [93] J. Butterworth et al., *PDF4LHC recommendations for LHC Run II*, J. Phys. G **43** (2016) 023001, arXiv: 1510.03865 [hep-ph].
- [94] A. Wald, Tests of Statistical Hypotheses Concerning Several Parameters When the Number of Observations is Large, Transactions of the American Mathematical Society **54** (1943) 426.
- [95] G. Cowan et al., *Asymptotic formulae for likelihood-based tests of new physics*, Eur. Phys. J. C **71** (2011) 1554, arXiv: 1007.1727 [physics.data-an], Erratum: Eur. Phys. J. C **73** (2013) 2501.
- [96] G. Choudalakis and D. Casadei, *Plotting the Differences Between Data and Expectation*, European Physical Journal Plus **127** (2011).
- [97] BaBar Collaboration, Measurement of an excess of  $\bar{B} \to D^{(*)} \tau^- \bar{\nu}_{\tau}$  decays and implications for charged Higgs bosons, Phys. Rev. D **88** (2013) 072012, arXiv: 1303.0571 [hep-ex].
- [98] LHCb Collaboration, Measurement of the Ratio of Branching Fractions  $\mathcal{B}(\bar{B}^0 \to D^{*+}\tau^-\bar{\nu}_{\tau})/\mathcal{B}(\bar{B}^0 \to D^{*+}\mu^-\bar{\nu}_{\mu}),$  Phys. Rev. Lett. **115** (2015) 111803, arXiv: 1506.08614 [hep-ex], Erratum: Phys. Rev. Lett. **115** (2015), 159901.
- [99] Belle Collaboration, Measurement of the branching ratio of  $\bar{B} \to D^{(*)} \tau^- \bar{\nu}_\tau$  relative to  $\bar{B} \to D^{(*)} \ell^- \bar{\nu}_\ell$  decays with hadronic tagging at Belle, Phys. Rev. D **92** (2015) 072014, arXiv: 1507.03233 [hep-ex].
- [100] Belle Collaboration, Measurement of the  $\tau$  lepton polarization and  $R(D^*)$  in the decay  $\bar{B} \to D^* \tau^- \bar{\nu}_{\tau}$  with one-prong hadronic  $\tau$  decays at Belle, Phys. Rev. D **97** (2018) 012004, arXiv: 1709.00129 [hep-ex].
- [101] LHCb Collaboration, Measurement of the Ratio of the  $B^0 \to D^{*-} \tau^+ \nu_{\tau}$  and  $B^0 \to D^{*-} \mu^+ \nu_{\mu}$  Branching Fractions Using Three-Prong  $\tau$ -Lepton Decays, Phys. Rev. Lett. **120** (2018) 171802, arXiv: 1708.08856 [hep-ex].
- [102] LHCb Collaboration, Test of lepton flavor universality by the measurement of the  $B^0 \to D^{*-} \tau^+ \nu_{\tau}$  branching fraction using three-prong  $\tau$  decays, Phys. Rev. D **97** (2018) 072013, arXiv: 1711.02505 [hep-ex].
- [103] Belle Collaboration, *Measurement of*  $\mathcal{R}(D)$  *and*  $\mathcal{R}(D^*)$  *with a Semileptonic Tagging Method*, Phys. Rev. Lett. **124** (2020) 161803, arXiv: 1910.05864 [hep-ex].
- [104] LHCb Collaboration, Measurement of the Ratio of Branching Fractions  $\mathcal{B}(B_c^+ \to J/\psi \tau^+ \nu_\tau)/\mathcal{B}(B_c^+ \to J/\psi \mu^+ \nu_\mu)$ , Phys. Rev. Lett. **120** (2018) 121801, arXiv: 1711.05623 [hep-ex].
- [105] LHCb Collaboration, Observation of the Decay  $\Lambda_b^0 \to \Lambda_c^+ \tau^- \overline{\nu}_{\tau}$ , Phys. Rev. Lett. **128** (2022) 191803, arXiv: 2201.03497 [hep-ex].

[106] LHCb Collaboration, *Measurement of the Ratios of Branching Fractions*  $\mathcal{R}(D^*)$  *and*  $\mathcal{R}(D^0)$ , Phys. Rev. Lett. **131** (2023) 111802, arXiv: 2302.02886 [hep-ex].